POLITECNICO
MILANO 1863

SCUOLA DI INGEGNERIA INDUSTRIALE
E DELL'INFORMAZIONE

Study of Fourier optical cavities for the confinement of exciton

Tesi di Laurea Magistrale in
Physics Engineering - Ingegneria Fisica

Author: **Luigi Brusaferri**

Student ID: 248290
Advisor: Prof. Giulio Nicola Felice Cerullo
Co-advisors: Prof. Simone Latini, Prof. Søren Raza, Prof. Bjarken Sørensen Jessen
Academic Year: 2024-25

Abstract

This thesis explores, within the framework of light matter interaction, the ability of different Fourier optical cavities [26] to confine excitons by making them experience a periodic potential [5], which is generated by the vacuum oscillations of the electromagnetic field. Fourier cavities are a novel optical structure where one of the surfaces of a conventional cavity is patterned with a sinusoidal shape: exploiting this discrete translational symmetry, the light dispersion bends, forming a periodic band structure akin to the electronic structure of a solid state system. In order to explore its eigenmodes, numerical simulations with COMSOL® and its MAN package [39][41], are carried out. In this regard, the materials that make up the cavity are studied and simulated via fully ab initio calculations, thanks to the GPAW [30] [40] [24] and the Quantum Espresso [11] [12] [10] codes. Finally, the exploration of the cavity eigenmodes is also carried out by nanofabricating a prototype of dielectric hBN cavity [27]: the nano lithographic technique used is the temperature scanning probe lithography, tSPL [31], on a PPA layer placed on top of the hBN flake. The outcome of this work is the calculation of the cavities eigenmodes, which could be later used to calculate the coupling coefficient with the excitons: the theoretical steps are introduced, but the calculation itself is open for future developments. Regarding the experimental work, after performing optical measures on the samples, the system of substrate, hBN, and PPA is found not to work. The reason lies in the nanofabrication: a future development should either use a different technique, different substrate, or etch the flake to directly carve the pattern on hBN.

Keywords: metaphotonics, quantum materials, ab initio calculations, nanolithography, numerical simulations

Abstract in lingua italiana

Questa tesi esplora, all'interno dello studio dell'interazione luce-materia, la possibilità di usare cavità ottiche di Fourier [26] per confinare eccitoni attraverso la creazione, mediante le oscillazioni di vuoto del campo elettromagnetico, di un potenziale periodico [5]. Per cavità di Fourier [26] si intende una normale cavità ottica, la cui superficie superiore ha però una forma sinusoidale: sfruttando la discreta simmetria translazionale che ne consegue, la dispersione della luce risulta piegata, e così si viene a formare una struttura a bande simile al caso dei solidi cristallini. Per studiare le soluzioni dell'equazione di Maxwell all'interno di tali cavità, sono state fatte simulazioni con COMSOL® e il relativo pacchetto MAN [39][41]. A tal proposito, i materiali costitutivi della cavità sono stati studiati con conti ab initio, grazie ai codici GPAW [30][40][24] e Quantum Espresso [11][12][10]. Infine, lo studio dei modi di cavità è portato avanti anche dal punto di vista sperimentale, con la nanofabbricazione di una cavità dielettrica di hBN [27]. Per ricavare la forma sinusoidale, è stata usata la tecnica nanolitografica conosciuta come tSPL [31] su uno strato di PPA posto sopra il fiocco di hBN. Il risultato di questa tesi è il calcolo dei modi propri della cavità, che potranno essere usati per il conto delle costanti di accoppiamento con gli eccitoni: la procedura teorica è introdotta, ma il calcolo in sé è lasciato a futuri sviluppi. Per quanto riguarda il lavoro sperimentale, a seguito di misure ottiche sui campioni fabbricati, il sistema composto da substrato, hBN, e PPA è risultato non funzionante. La ragione sta nella nanofabbricazione: per future implementazioni sarà necessario usare o una tecnica differente, o un diverso substrato, oppure ancora transferire la forma sinusoidale da PPA a hBN con etching.

Parole chiave: metafotonica, materiali quantistici, ab inito, nanolitografia, simulazioni numeriche

Contents

Introduction

The study of light and matter interaction, as the name suggests, lies at the very crossroad between the fields of optics and solid state physics. In this regard, it is quite common to either analyse the electromagnetic field, and approximate the matter contribution with a known dielectric function, or to analyse matter, and approximate the electromagnetic contribution with a free-light dispersion. In order to broaden the understanding of physical phenomena happening at the edge of these approximations, a more comprehensive treatment of both the electromagnetic field and matter particles is required.

The systems, chosen for this study, where the interaction takes place, are optical cavities that have characteristic bi-dimensional sinusoidal patterns called Fourier surfaces [26]. Because these kind of structures are a novelty in the field of light-matter interaction, one of the scientific question to be answered is on the possibility of the modes living inside these special cavities to confine quasi-particles such as excitons. In order to address this issue, three types of cavities are taken into consideration and simulated: the first one exploits the phenomenon of total internal reflection to confine light; to further enhance the confinement, the second one employs particular states called surface plasmons polaritons [4]. These states can be viewed as solutions to the Maxwell's equations at the interface between a metal and a dielectric. Similarly, the third kind of cavity increases the confinement even more via states called phonon polaritons [4]: they are also quasi-particles, but their source lies in the relative movement of ions inside a lattice. An extensive analysis of their performance is presented and commented.

Periodicity in the optical cavity is central to this study, and the reason is that the fundamental goal of this work is to show how periodic patterns cause excitons to experience a periodic potential. The general concept of using optical cavities to change materials proprieties has been widely discussed in literature (for reference [18] [28] [2]), but the novel idea on exploiting periodicity comes from the paper *"Tunable Phases of Moiré Excitons in van der Waals Heterostructures"* [5]: in that study, it is the creation of a Moiré superlattice to cause excitons the experiencing of a periodic potential. This work aims to reproduce similar results, using an optical cavity instead of the Moiré lattice.

Excitons are quasi particles born from the Coulomb interaction between an excited electron and a hole. This work deals in particular with excitons that live in 2D materials called transition metal dichalcogenides (TMDs): due to the low dimensionality, electrons and holes inside these materials can interact more strongly, as there is less matter around to potentially screen the interaction. This condition results in an enhancement of the optical response.

In order to address these topics, this thesis is arranged in the following manner: the first chapter introduces concepts such as the behaviour of light when trapped inside cavities, how it strays from the free space case, and what the consequences are. These ideas will be the groundwork for the later discussions. Then, it is examined the behaviour of matter in presence of light, with a special focus for the materials chosen. In order to quantitatively assess their optical response, fully ab initio calculations are carried out. The results of these computations will be used for the simulations of the field inside the cavity. In the third chapter, simulations of the electromagnetic field are presented and analysed: there, three subsections are devoted to examining the most relevant aspect of the simulations, that is, the numerical methods applied. After that, in order to explore the possibility of building a Fourier cavity, and measure its optical response, the fourth chapter presents the experimental work, with a detailed description of the nanofabrication methods, the setup for the optical measurements, and their results. In doing so, another research question is also addressed: on the possibility of having a grating effect on the guided modes by simply adding a patterned layer of another material (a thermoplastic) on top of hBN. Lastly, the fifth chapter gives a brief overview at the future developments.

The outcome of this work is the calculation of the cavities eigenmodes, which could be later used to calculate the coupling coefficient with the excitons: the theoretical steps are introduced, but the calculation itself is open for future developments. It is finally worth mentioning that the results presented regarding the hyperbolic polaritons are part of a project which is still running, and therefore they are to be considered as only a sample of a work which is in progress.

1 | Chapter one: Confining light

1.1. Light in optical cavities

In order to enhance the coupling with excitons, the intensity of the electromagnetic field needs to be increased. The most direct way would be to simply increase the number of photons, but that requires a lot of input power. Therefore the choice made in this work, more cost effective, is to enhance the electromagnetic field by confining it. During the course of history, many methods have been devised to accomplish such result, as, for example, optical lenses, systems of mirrors, or cavities. This section will mainly focus on the electromagnetic field inside optical cavities, and its dispersion relation: that is, how different optical structures modify the propagation of light. In the following, four relevant and insightful cases, among the many, will be discussed.

1.1.1. Fabry-Perot cavities

The most simple, yet very effective, structure is known as the *Fabry-Perot cavity*: it consists of two perfect planar mirrors, placed at a distance $2d$ from each other.

(a) Sketch of the cavity

(b) Scheme of the rays inside the cavity

Figure 1.1: Fabry Perot cavity sketches

Because the mirrors are assumed to be perfectly reflecting, a ray launched inside this structure with an angle θ (with respect to the propagation direction) will be reflected top and bottom, as shown in the picture 1.1b.

In order to understand how this multiple bouncing modifies the electric field and the

dispersion relation, consider the following argument. The propagation can be sustained only if the following self-consistency condition is met: $\Delta\varphi_{AC} - \Delta\varphi_{AC} = 2q\pi$ where q is a positive integer, zero included. What the equation enforces, explicitly, is that the phase of the light, taken in to points symmetric with respect to the bouncing off of a mirror, must be the same (except for a 2π shift): this is the reason why it's referred to as self-consistency condition. Considering the figure above, it naturally follows:

$$\overline{AC} = d/sin(\theta) \quad \text{and} \quad \overline{AB} = \overline{AC} \cdot cos(2\theta) = d \cdot cos(2\theta)/sin(\theta) \tag{1.1}$$

Therefore:

$$\overline{AC} - \overline{AB} = \frac{d}{sin(\theta)} - \frac{d}{sin(\theta)} \cdot cos(2\theta) = \frac{d}{sin(\theta)}(1 - cos(2\theta) = \tag{1.2}$$

$$= \frac{2d}{sin(\theta)} sin^2(\theta) = 2d \cdot sin(\theta) \tag{1.3}$$

By definition, the phase acquired by a monochromatic light ray that has traveled an optical path $n \cdot \Delta x$ is equal to $n \cdot \Delta x \cdot 2\pi/\lambda$ (λ being the wavelength of the light). Thus:

$$\Delta\varphi_{AC} - \Delta\varphi_{AB} = \frac{2\pi}{\lambda} \cdot n \cdot \overline{AC} - 2\pi - \frac{2\pi}{\lambda} \cdot n \cdot \overline{AB} = \frac{2\pi}{\lambda} \cdot n \cdot \left(\overline{AC} - \overline{AB}\right) - 2\pi \tag{1.4}$$

$$= \frac{2\pi}{\lambda} \cdot n \cdot 2d \cdot sin(\theta) - 2\pi \tag{1.5}$$

As a consequence of the self-consistency relation becomes:

$$2q\pi = \frac{2\pi}{\lambda} \cdot n \cdot 2d \cdot sin(\theta) - 2\pi \tag{1.6}$$

$$2(q+1)\pi = \frac{2\pi}{\lambda} \cdot n \cdot 2d \cdot sin(\theta) \tag{1.7}$$

By defining $m = q+1$, the self-consistency relation for guided modes inside a Fabry-Perot cavity can be written as:

$$sin(\theta_m) = \frac{m\lambda}{2d \cdot n} \quad \text{where} \quad m = 1, 2, 3, ... \tag{1.8}$$

Hence, within a given cavity, there will be a variety of modes propagating with different angles. Considering a generic mode, whose propagation vector $\vec{k}$ lays in the (x, z) plane and makes an angle θ with the x axis, it is possible to write:

$$\vec{k} = k_z\vec{u}_z + k_x\vec{u}_x = k \cdot sin(\theta)\vec{u}_z + k \cdot cos(\theta)\vec{u}_x \tag{1.9}$$

with $\vec{u}_x$ and $\vec{u}_z$ unit vectors along the axis x and z, respectively. Assuming $\theta = \theta_m$ (i.e. it satisfies the self-consistency equation), it follows:

$$k_{zm} = k \cdot sin(\theta_m) = \frac{2\pi}{\lambda} \cdot \frac{m\lambda}{2d \cdot n} = \frac{m\pi}{d} \tag{1.10}$$

$$k_{xm} = k \cdot cos(\theta_m) = \frac{2\pi}{\lambda} \cdot cos(\theta_m) \tag{1.11}$$

Therefore:

$$k_{xm}^2 = n^2 \left(\frac{2\pi}{\lambda}\right)^2 cos^2(\theta_m) = n^2 \left(\frac{2\pi}{\lambda}\right)^2 \left(1 - sin^2(\theta_m)\right) = \tag{1.12}$$

$$= n^2 \left(\frac{2\pi}{\lambda}\right)^2 - n^2 \left(\frac{2\pi}{\lambda}\right)^2 sin^2(\theta_m) = \tag{1.13}$$

$$= n^2 \left(\frac{2\pi}{\lambda}\right)^2 - n^2 \left(\frac{2\pi}{\lambda}\right)^2 \frac{m^2\lambda^2}{4d^2n^2} = n^2 \left(\frac{2\pi}{\lambda}\right)^2 - m^2\frac{\pi^2}{d^2} = \tag{1.14}$$

$$= n^2\frac{\omega^2}{c^2} - m^2\frac{\pi^2}{d^2} \tag{1.15}$$

Hence, the dispersion relation for a Fabry-Perot cavity is:

$$\omega = \frac{c}{n}\sqrt{k_{xm}^2 + m^2\frac{\pi^2}{d^2}} \tag{1.16}$$

It is interesting to note that the dispersion is parabolic, as opposed to the linear dispersion found for e.m. waves propagating in free space: it is now clear that light confined in a cavity behaves in a fundamentally different way than light in free space.

Another relevant characteristic of the modes, besides the dispersion relation, is the shape of their electromagnetic field; for simplicity, only the electric field will be considered. Assume one of these modes corresponds to a specific value of m: it is possible to write its electric field as a sum of two waves, as shown in the picture below.

Indeed:

$$E_m^+(x,z,t) = A_m e^{i(\omega t - k_x x - k_z z)} \tag{1.17}$$

$$E_m^-(x,z,t) = A_m e^{i(\omega t - k_x x + k_z z)} e^{i(m-1)\pi} \tag{1.18}$$

$$E_m(x,z,t) = E_m^+ + E_m^- = A_m e^{i(\omega t - k_x x)} \left[e^{-ik_z z} + e^{i(m-1)\pi} e^{-ik_z z}\right] \tag{1.19}$$

where the phase shift $\Delta\varphi = q\pi = (m-1)\pi$ is accounted for. In order to visualize them better, it is possible to rewrite the field expression as a product of a periodic term times

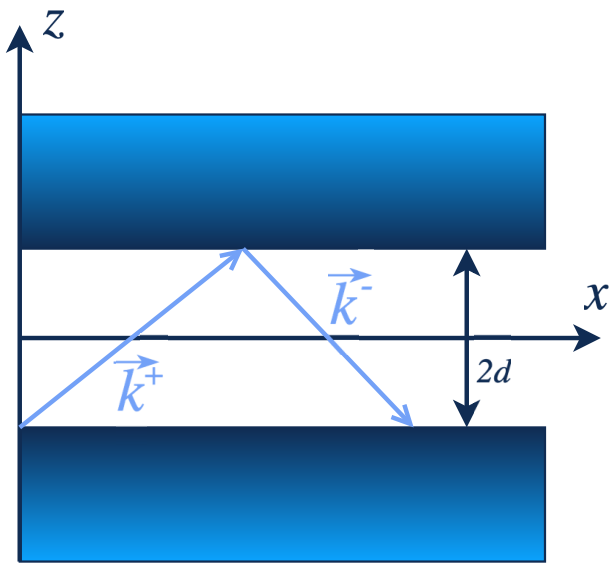

Figure 1.2: Sketch of the waves $\vec{k}^+$ and $\vec{k}^-$ making up to overall electromagnetic field

a propagating one:

$$E_m(x,z,t) = c_m \cdot u_m(z) \cdot e^{i(\omega t - k_x x)} \tag{1.20}$$

where

$$\text{m odd} \quad c_m = \sqrt{2d}A_m \quad \text{and} \quad u_m(z) = \sqrt{\frac{2}{d}} \cdot cos\left(\frac{m\pi z}{d}\right) \tag{1.21}$$

$$\text{m even} \quad c_m = -i\sqrt{2d}A_m \quad \text{and} \quad u_m(z) = \sqrt{\frac{2}{d}} \cdot sin\left(\frac{m\pi z}{d}\right) \tag{1.22}$$

It is important to realise that the normalization constant A_m is that is proportional to $\sqrt{1/A}$ where $A = l_x \cdot d$. Assuming l_x constant and very large, since the field is unbound along x, the normalization constant becomes dependent on d following $A_m \propto 1/\sqrt{d}$. Thus, the smaller the distance between the mirrors, the higher the amplitude, which means that the electromagnetic field inside a Fabry-Perot cavity is enhanced.

Before moving on to the next example, it is relevant to notice that there will be a value m_{max} such that

$$sin(\theta_{m_{max}+1}) = \frac{(m_{max}+1)\lambda}{2d \cdot n} > 1 \tag{1.23}$$

Hence:

$$m_{max} = \frac{2d \cdot n}{\lambda} \tag{1.24}$$

that is, m_{max} is the closest integer to $2d{\cdot}n/\lambda$. Thus, by varying the geometry, the material, or the wavelength, it is possible to have Fabry-Perot cavities that host different numbers of modes.

1.1.2. Dielectric waveguides

Another widely known structure is the *planar dielectric waveguide*: it consists of a slab of a dielectric material having refractive index n_1, called *core*, placed in between another dielectric material having refractive index n_2, called *cladding*. It is also assumed that $n_1 > n_2$.

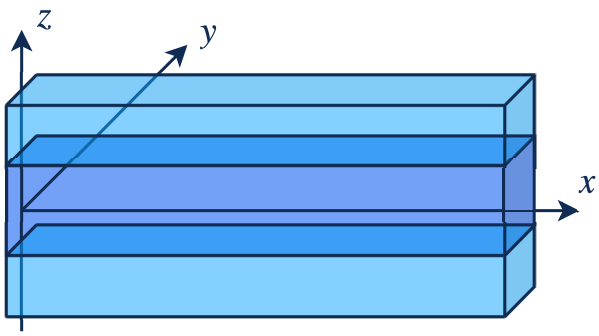

Figure 1.3: Sketch of a dielectric waveguide: in blue the cladding, in purple the core

The confinement of light within the core is based on the idea of total internal reflection: because $n_1 > n_2$, if a ray inside the core meets the cladding at a certain angle, it will be completely reflected. It is possible to define a *critical angle*:

$$sin\theta_{1CR} = \frac{n_2}{n_1} \tag{1.25}$$

Thus there will be internal reflection as long as $\theta_1 > \theta_{1CR}$.

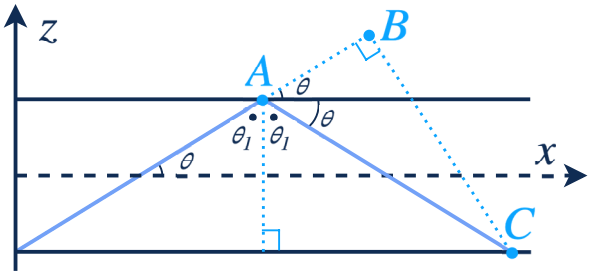

Figure 1.4: Sketch of the rays inside the dielectric slab

From the picture above it is clear that $\theta_1 = \pi/2 - \theta$. Hence, by defining $\theta_{1CR} = \pi/2 - \theta_{CR}$, when $\theta_1 > \theta_{1CR}$ it will follow that $\theta < \theta_{CR}$. Therefore:

$$sin\theta_1 > n_2/n_1 \rightarrow sin(\pi/2 - \theta) = cos\theta > n_2/n_1 \rightarrow \quad \theta < arccos(n_2/n_1) \tag{1.26}$$

At this point, it is interesting to find out the modes that live inside this structure. As shown in the previous example, a mode must satisfy the self-consistency condition $\Delta\varphi_{AC} - \Delta\varphi_{AC} = 2q\pi$ where q is a positive integer, zero included. The distances are still:

$$\overline{AC} = \frac{d}{sin\theta} \tag{1.27}$$

$$\overline{AB} = \overline{AC} \cdot cos2\theta = \frac{d}{sin\theta} cos2\theta \tag{1.28}$$

$$\tag{1.29}$$

While the phase shifts become:

$$\Delta\varphi_{AC} = \frac{2\pi}{\lambda} n_1 \frac{d}{sin\theta} - 2\varphi_r \tag{1.30}$$

$$\Delta\varphi_{AB} = \frac{2\pi}{\lambda} n_1 \frac{d}{sin\theta} cos2\theta \tag{1.31}$$

Imposing self-consistency $\Delta\varphi_{AC} - \Delta\varphi_{AC} = 2q\pi$ leads to:

$$\frac{2\pi}{\lambda} n_1 \frac{d}{sin\theta} - 2\varphi_r - \frac{2\pi}{\lambda} n_1 \frac{d}{sin\theta} cos2\theta = 2q\pi \rightarrow \frac{2\pi}{\lambda} n_1 \frac{d}{sin\theta}(1 - cos2\theta) - 2\varphi_r = 2q\pi \tag{1.32}$$

$$\frac{2\pi}{\lambda} n_1 \frac{d}{sin\theta} 2sin^2\theta - 2\varphi_r = 2q\pi \rightarrow \frac{\varphi_r}{2} = \frac{\pi}{\lambda} n_1 d \cdot sin\theta - q\frac{\pi}{2} \tag{1.33}$$

Therefore

$$tan\left(\frac{\varphi_r}{2}\right) = tan\left(\frac{\pi}{\lambda} n_1 d \cdot sin\theta - q\frac{\pi}{2}\right) \tag{1.34}$$

In order to proceed, it is necessary to deal with φ_r (see section **??** in Appendix A for the complete derivation). It is possible to prove that the modes correspond to the angles θ that satisfy the equation:

$$tan\left(\frac{\pi}{\lambda} n_1 d \cdot sin\theta - q\frac{\pi}{2}\right) = \sqrt{\frac{cos^2\theta_{1CR}}{sin^2\theta} - 1} \tag{1.35}$$

From which it derives that the number M of guided modes for a given cavity is:

$$M = \left\lceil \frac{2d}{\lambda} \sqrt{n_1^2 - n_2^2} \right\rceil \tag{1.36}$$

where the term $\sqrt{n_1^2 - n_2^2}$ is known as *numerical aperture*.

Having understood the conditions required for modes to propagate, it is now time to analyse their behaviour more closely. In the following, assume a mode travels with an

angle θ_m and has a TE polarization. Thus, in a similar fashion to the Fabry-Perot case, it is possible to prove (full derivatin can be found in A.2 Appendix A):

$$E(x,z,t) = u_m e^{i(\omega t - k_{xm}x)} \tag{1.37}$$

where:

$$u_m = \begin{cases} A_m cos\left(\frac{2\pi n_1 sin\theta_m}{\lambda} y\right) & n \text{ even}, |y| < d/2 \\ A_m sin\left(\frac{2\pi n_1 sin\theta_m}{\lambda} y\right) & n \text{ odd}, |y| < d/2 \\ c_m e^{-\gamma_m z} & \text{for } y > d/2 \\ c_m e^{+\gamma_m z} & \text{for } y < d/2 \end{cases} \tag{1.38}$$

From this expression of the field, it is possible to see that the enhancement of the electromagnetic field inside a dielectric waveguide follows from a similar argument as the Fabry-Perot case. However, this time, the confinement is weaker, due to the evanescent tails $e^{\pm\gamma_m z}$ in the cladding region.

Lastly, from the self consistency relation it is also possible to obtain the dispersion relation. Firstly, it is relevant to notice:

$$\frac{2\pi}{\lambda} n_1 sin\theta_m = \sqrt{\frac{n_1^2\omega^2}{c^2} - k_{xm}^2} \tag{1.39}$$

Therefore:

$$\begin{aligned} tan^2(\varphi_r/2) = \frac{cos^2\theta_{1CR}}{sin^2\theta_m} - 1 = \frac{1 - sin^2\theta_{1CR}}{sin^2\theta_m} - 1 = \frac{1 - n_2^2/n_1^2}{1 - k_{xm}^2 c^2/n_1^2\omega^2} - 1 = \\ = \frac{k_{xm}^2 c^2/n_1^2\omega^2 - n_2^2/n_1^2}{1 - k_{xm}^2 c^2/n_1^2\omega^2} = \frac{k_{xm}^2 - n_2^2\omega^2/c^2}{n_2^2\omega^2/c^2 - k_{xm}^2} \end{aligned}$$

$$tan^2(\varphi_r/2) = tan\left(\frac{\pi}{\lambda} n_1 d \cdot sin\theta - q\frac{\pi}{2}\right) = tan^2\left(\frac{d}{2}\sqrt{\frac{n_1^2\omega^2}{c^2} - k_{xm}^2} - m\frac{\pi}{2}\right) \tag{1.40}$$

Which naturally implies:

$$tan^2\left(\frac{d}{2}\sqrt{\frac{n_1^2\omega^2}{c^2} - k_{xm}^2} - m\frac{\pi}{2}\right) = \frac{k_{xm}^2 - n_2^2\omega^2/c^2}{n_2^2\omega^2/c^2 - k_{xm}^2} \tag{1.41}$$

There is no exact analytical expression for $\omega = \omega(k_{xm})$; however it is possible to calculate it numerically, as shown in figure 1.5.

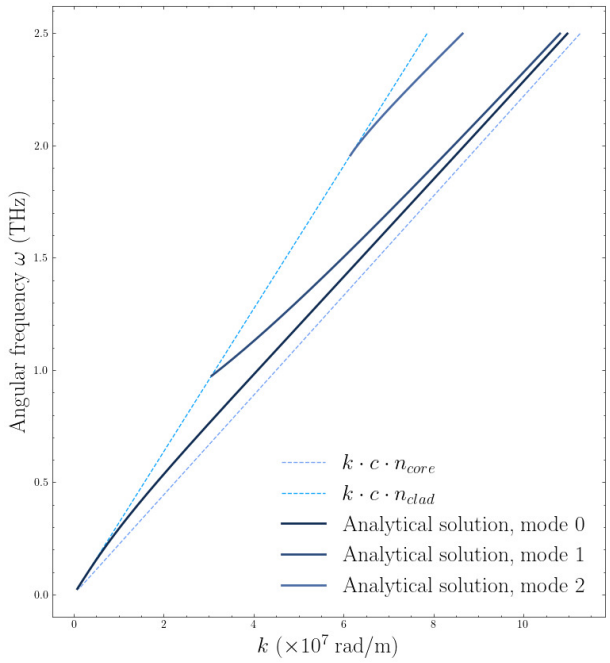

Figure 1.5: Numerical solution of equation 1.41, valid for TE modes only

1.1.3. Plasmonic cavities

It is well known that in vacuum or in a dielectric material the general solutions of Maxwell equations are plane waves. However they are not the only possible general solution. In fact, when considering the interface between a dielectric and a metal, a new kind of solution arises [15] [43]: *plasmon polariton*. The name "polariton" refers to a quasiparticle born from the interaction between light and a matter excitation; in this case, the excitation is the plasmon. The idea behind a plasmonic cavity is to exploit this type of solutions to confine the field strongly, even on a sub-wavelength scale.

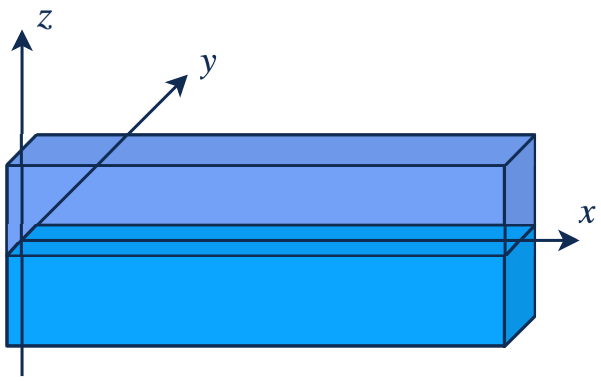

Figure 1.6: Sketch of a plasmonic cavity: in purple the dielectric ε_2, in blue the metal ε_1

Consider a planar interface between a dielectric and a metal slab, whose dielectric functions are, respectively, $\varepsilon_2 = \varepsilon_d$ and $\varepsilon_1(\omega) = 1 - \omega_p^2/\omega^2$. Assume the interface lies on the (x, y) plane at a height $z = 0$. Due to the optical isotropy of the two media, it is possible to consider, without loss of generality, a solution propagating along the x axis; at first assume it is a TM wave. Because the fields are expected to be damped away both in the metal (1) and in the dielectric (2), the solution to the Maxwell equations can be written as:

$$\vec{E}_1 = (E_{1x}, 0, E_{1z})e^{i(q_1 x - \omega t)}e^{+k_1 z} \tag{1.42}$$
$$\vec{B}_1 = (0, B_{1y}, 0)e^{i(q_1 x - \omega t)}e^{+k_1 z} \tag{1.43}$$
$$\vec{E}_2 = (E_{2x}, 0, E_{2z})e^{i(q_2 x - \omega t)}e^{-k_2 z} \tag{1.44}$$
$$\vec{B}_2 = (0, B_{2y}, 0)e^{i(q_2 x - \omega t)}e^{-k_2 z} \tag{1.45}$$

Because the parallel components of the fields at $z = 0$ must be continuous:

$$E_{1x} = E_{2x}; \quad B_{1y} = B_{2y}; \quad q_1 = q_2 \tag{1.46}$$

Thus:

$$\vec{E}_1 = (E_x, 0, E_{1z})e^{i(qx - \omega t)}e^{+k_1 z} \tag{1.47}$$
$$\vec{B}_1 = (0, B_y, 0)e^{i(qx - \omega t)}e^{+k_1 z} \tag{1.48}$$
$$\vec{E}_2 = (E_x, 0, E_{2z})e^{i(qx - \omega t)}e^{-k_2 z} \tag{1.49}$$
$$\vec{B}_2 = (0, B_y, 0)e^{i(qx - \omega t)}e^{-k_2 z} \tag{1.50}$$

Furthermore, by applying the Maxwell equation $\nabla \cdot (\varepsilon \vec{E}) = 0$, it follows:

$$iqE_x + k_1 E_{1z} = 0 \quad \text{and} \quad iqE_x - k_2 E_{2z} = 0 \tag{1.51}$$

Considering these two equations and imposing the continuity of the normal component $\varepsilon_1(\omega)E_{1z} = \varepsilon_2 E_{2z}$, it is possible to write:

$$\frac{\varepsilon_1(\omega)}{k_1} + \frac{\varepsilon_2}{k_2} = 0 \tag{1.52}$$

In order to find the solutions, it is now necessary to consider the two curl Maxwell's equations:

$$\nabla \times \vec{E}_i = -\frac{1}{c}\frac{\partial \vec{B}_i}{\partial t} \quad \text{and} \quad \nabla \times \vec{B}_i = \varepsilon_i \frac{1}{c}\frac{\partial \vec{E}_i}{\partial t} \tag{1.53}$$

where $i = 1$ for the metal and $i = 2$ for the dielectric. To get rid of the magnetic field, it is necessary to take the curl of the first equation, and inserting the resulting expression in the second one, so that the final result is:

$$\nabla^2 \vec{E}_i = \frac{\varepsilon_i}{c^2} \frac{\partial^2 \vec{E}_i}{\partial t^2} \tag{1.54}$$

Substituting the fields in 1.47 into the above equation yields:

$$q^2 = k_1^2 + \frac{\varepsilon_1(\omega)}{c^2}\omega^2 \quad \text{and} \quad q^2 = k_2^2 + \frac{\varepsilon_2}{c^2}\omega^2 \tag{1.55}$$

which can be merged into the single expression:

$$q^2 = \frac{\omega^2}{c^2} \frac{\varepsilon_1(\omega)\varepsilon_2}{\varepsilon_1(\omega) + \varepsilon_2} \tag{1.56}$$

By substituting $\varepsilon_1(\omega)$ and ε_2 with their definition, it is possible to write the surface plasmon polariton dispersion relation:

$$q^2 = \frac{\omega^2}{c^2}\varepsilon_d \frac{\omega^2 - \omega_p^2}{(\varepsilon_d + 1)\omega^2 - \omega_p^2} \tag{1.57}$$

Below, its plot:

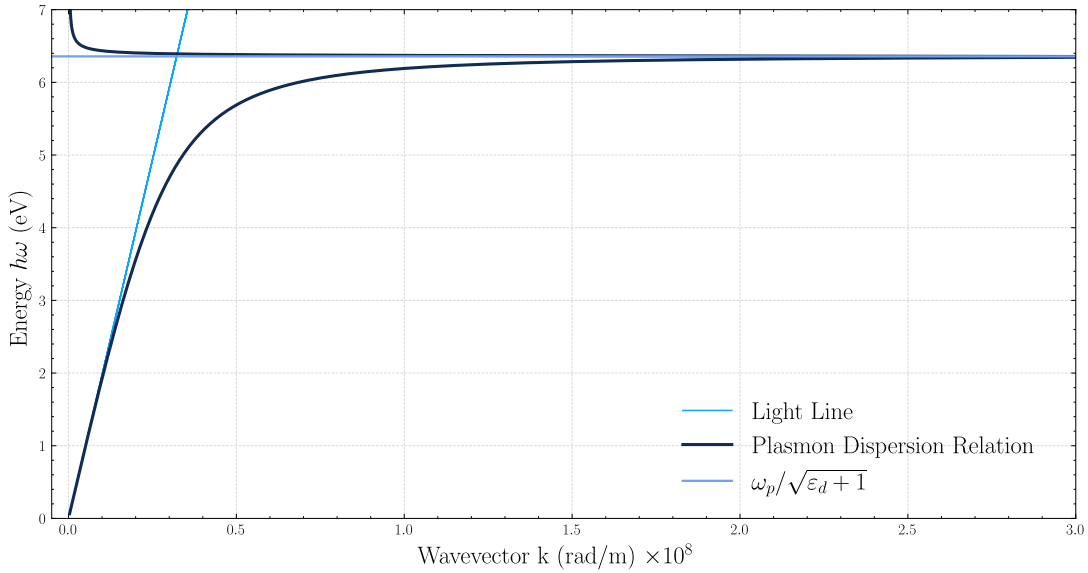

Figure 1.7: Surface plasmon polariton dispersion

Note that the dispersion for small values of q closely follows the dispersion of electromagnetic waves propagating inside the dielectric medium: the polariton is here more a photon than a plasmon. Then, the curve strays from the light line, and finally, for higher values of q, it tends to the constant $\omega_p/\sqrt{\varepsilon_d + 1}$. It is not a random value: indeed it is the frequency obtained by solving the Maxwell's equations whit the speed of light set to infinite. For this reason, it is also known as the surface plasmon polariton *non-retarded* solution.

Lastly, as a final remark, it is interesting to note that, at the beginning of the subsection, if the assumption was to have a TE profile instead of a TM one, there wouldn't have been any solution. It is possible to understand why in an intuitive way. Indeed, eq. 1.51 shows the ratio between the transverse (z) and longitudinal (x) components of the electric field inside the medium. By including eq.s 1.55 and 1.56, it follows:

$$\frac{E_{2z}}{E_x} = i\frac{q}{k_2} = i\sqrt{\frac{\omega_p^2 - \omega^2}{\varepsilon_d \omega^2}} \tag{1.58}$$

This expression shows clearly how the component along z dominates in the low frequency (and low momentum) range, making the polariton behave in a light-like manner; the longitudinal components takes over only for very high frequency ($E_{2z} = E_x$ for $\omega = \omega_p/(\varepsilon_d + 1)$), where the polariton acts more like a plasmon. Now consider a TE mode: its electric field has only the transverse (y) component, thus lacking the ability to generate a hybrid photon-plasmon (i.e. a polariton) quasi-particle.

1.1.4. Hyperbolic dispersion cavities

At the end of the last subsection, there is a plot of the surface plasmon polaritons dispersion. Looking at that plot, it is insightful to notice that the surface plasmon polaritons dispersion exists only in the interval $(0, \omega_p/\sqrt{\varepsilon_d + 1})$, and that in such energy range $\varepsilon_1(\omega) < 0$. Indeed, those kind of solutions of the Maxwell equations are only allowed at the interface between a medium with a positive dielectric constant and a medium with a negative one. Because materials with an anisotropic ε exist, the question rises naturally: what would happen to a medium whose dielectric constant is positive along one direction and negative along another one? The answer are the quasi-particles *hyperbolic polaritons* [17] [38] [8] [13] [16] [34]. The meaning of their name lays in the shape of the dispersion relation in k space. Indeed, assume a material has a dielectric constant that can be

represented by the diagonal tensor:

$$\overline{\overline{\varepsilon}} = \begin{bmatrix} \varepsilon_{xx} & 0 & 0 \\ 0 & \varepsilon_{yy} & 0 \\ 0 & 0 & \varepsilon_{zz} \end{bmatrix} \tag{1.59}$$

Consider now the wave equation:

$$\overline{\overline{\varepsilon}} \frac{1}{c^2} \frac{\partial^2 \vec{E}}{\partial t^2} - \nabla^2 \vec{E} = 0 \tag{1.60}$$

Assuming the electric field $\vec{E} \propto e^{i(\vec{k}\cdot\vec{r}-\omega t)}$, then the above equation becomes:

$$\begin{bmatrix} \omega^2\varepsilon_{xx}/c^2 - k_y^2 - k_z^2 & k_x k_y & k_x k_z \\ k_x k_y & \omega^2\varepsilon_{yy}/c^2 - k_x^2 - k_z^2 & k_y k_z \\ k_x k_z & k_y k_z & \omega^2\varepsilon_{zz}/c^2 - k_x^2 - k_y^2 \end{bmatrix} \vec{E} = 0 \tag{1.61}$$

In order to find the solutions it is necessary to impose:

$$det \begin{bmatrix} k_0^2\varepsilon_{xx} - k_y^2 - k_z^2 & k_x k_y & k_x k_z \\ k_x k_y & k_0^2\varepsilon_{yy} - k_x^2 - k_z^2 & k_y k_z \\ k_x k_z & k_y k_z & k_0^2\varepsilon_{zz} - k_x^2 - k_y^2 \end{bmatrix} = 0 \tag{1.62}$$

which results in:

$$T_x T_y T_z + T_y T_z k_x^2 + T_x T_z k_y^2 + T_x T_y k_z^2 = 0 \tag{1.63}$$

where

$$T_\alpha \triangleq k_0^2\varepsilon_{\alpha\alpha} - k_x^2 - k_y^2 - k_z^2 \quad \text{and} \quad k_0^2 = \omega^2/c^2 \tag{1.64}$$

In order to proceed, consider a medium where $\varepsilon_{xx} = \varepsilon_{zz} = \varepsilon_\parallel > 0$ and $\varepsilon_{yy} = \varepsilon_\perp$ where $\varepsilon_\perp < 0$. As a consequence:

$$T_x = T_z = T_\parallel = \varepsilon_\parallel\omega^2/c^2 - k_x^2 - k_y^2 - k_z^2 \quad \text{and} \quad T_y = T_\perp = \varepsilon_\perp\omega^2/c^2 - k_x^2 - k_y^2 - k_z^2 \tag{1.65}$$

Thus eq. 1.63 becomes:

$$T_\parallel T_\perp + T_\perp(k_x^2 + k_z^2) + T_\parallel k_y^2 = 0 \tag{1.66}$$

which can be simplified into:

$$\left(\frac{\omega^2}{c^2} - \frac{k_x^2 + k_y^2 + k_z^2}{\varepsilon_\parallel}\right)\left(\frac{\omega^2}{c^2} - \frac{k_x^2 + k_z^2}{\varepsilon_\perp} - \frac{k_y^2}{\varepsilon_\parallel}\right) = 0 \tag{1.67}$$

The second term reveals where the adjective "hyperbolic" comes from: the expression's plot in the (k_x, k_y, k_z) has a hyperbolic shape (the idea is even clearer when seen from above, figure 1.8b)

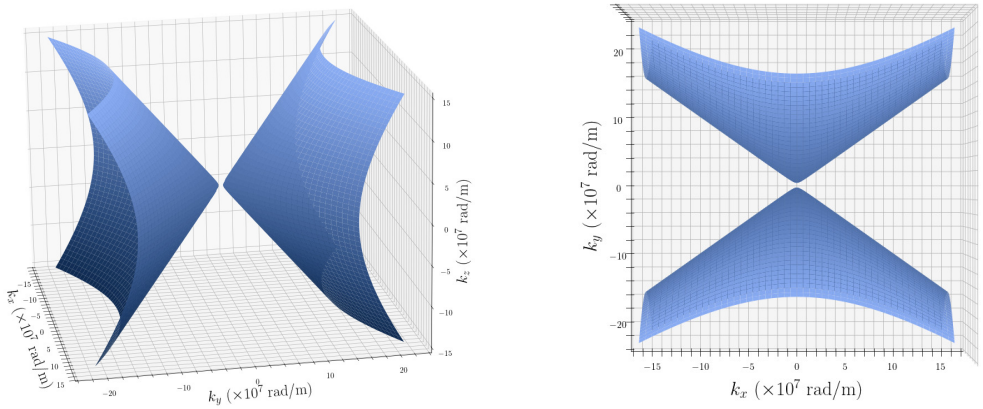

(a) 3D view (b) Cut along plane of constant k_z

Figure 1.8: Full dispersion assuming $\varepsilon_\parallel = 1$ and $\varepsilon_\perp = -1$

In order to see the relevance of this hyperbolic form for field confinement, consider that light propagating in the free space, on the other hand, has a spherical dispersion. At a certain energy ω_0, a general solution is a superposition of multiple states lying on the isosurface $\omega = \omega_0$: because such surface is spherical, this number of states is limited, and therefore the solution has only a limited number of k-vectors, which results in poor confinement. Vice versa, with a hyperbolic dispersion, there can be infinitely many states, and hence k-vectors contributions, which results in much greater confinement. In theory the hyperbolic iso-surfaces are infinite, hence hosting an infinite number of states; in practice that is not the case, but still the number of states is a lot bigger than the spherical dispersion case.

1.2. Manipulating light dispersion

The language of symmetry is a powerful tool in physics. This section will explore the consequence of symmetries in an optical structure, with a special focus on discrete translational symmetry: the reason for the scientific interest towards periodic structure is because of their particular symmetry, which causes the appearance of photonic band structures. This section is adapted from the book "Photonic Crystals: Molding the flow of light" [19]

1.2.1. Optical Bloch theorem and band structure

Assuming a linear, isotropic, non dispersive, non magnetic ($\mu_r \approx 1$, and lossless material, the Maxwell equations become:

$$\nabla \cdot \vec{H}(\vec{r},t) = 0 \qquad \nabla \times \vec{E}(\vec{r},t) + \mu_0 \frac{\partial \vec{H}(\vec{r},t)}{\partial t} = 0$$
$$\nabla \cdot \Big[\varepsilon(\vec{r})\vec{E}(\vec{r},t)\Big] = 0 \qquad \nabla \times \vec{H}(\vec{r},t) - \varepsilon_0 \varepsilon(\vec{r}) \frac{\partial \vec{E}(\vec{r},t)}{\partial t} = 0$$

where it holds true:

$$\vec{D}(\vec{r},t) = \varepsilon_0 \varepsilon(\vec{r})\vec{E}(\vec{r},t) \quad \text{and} \quad \vec{B}(\vec{r},t) = \mu_0 \mu(\vec{r})\vec{H}(\vec{r},t)$$

Further, assuming an harmonic behaviour in time, the fields can be written as:

$$\vec{H}(\vec{r},t) = \vec{H}(\vec{r})e^{-i\omega t} \quad \text{and} \quad \vec{E}(\vec{r},t) = \vec{E}(\vec{r})e^{-i\omega t}$$

Hence, substituting this analytical expressions of the fields in the above equations and taking a few algebraic steps, it is possible to condense everything in a single equation:

$$\nabla \times \left(\frac{1}{\varepsilon(\vec{r})} \nabla \times \vec{H}(\vec{r})\right) = \left(\frac{\omega}{c}\right)^2 \vec{H}(\vec{r})$$

By defining the operator $\hat{\Theta}$ as:

$$\hat{\Theta}\vec{H} \coloneqq \nabla \times \left(\frac{1}{\varepsilon(\vec{r})} \nabla \times \vec{H}(\vec{r})\right)$$

the equation above can be re-written as an eigenvalue problem:

$$\hat{\Theta}\vec{H} = \left(\frac{\omega}{c}\right)^2 \vec{H}(\vec{r})$$

This result is known as *master equation*. In general, eigenfunctions and eigenvalues of $\hat{\Theta}$ are not easily found. However, suppose the existance of an operator $\hat{S}$, whose eigenfucntions and eigenvalues easy to determine. If the system possesses the symmetry related to this operator, that is if $\hat{\Theta}$ commutes with $\hat{S}$, then it is possible to build and classify the eigenfunctions of $\hat{\Theta}$ using the properties of $\hat{S}$. To better understand this concept, consider the examples of continous and discrete translational symmetry.

Consider the operator related to the continous translational symmetry: $\hat{T}_{\vec{d}}$, where $\vec{d}$ represent an arbitrary displacement vector. A system that has this symmetry along all three directions is called *homogenous medium*. In such a case, the eigenfunctions of $\hat{T}_{\vec{d}}$ have form $c \cdot e^{i\vec{k}\cdot\vec{r}}$, and it is possible to write the modes (i.e. the eigenfunctions of $\hat{\Theta}$) as:

$$\vec{H}_{\vec{k}}(\vec{r}) = \vec{H}_0 e^{i\vec{k}\cdot\vec{r}}$$

Hence, the modes can be classified by their $\vec{k}$ vector. Even though nothing can be said regarding their frequencies, it is still possible, for each $\vec{k}$, to order the modes for increasing ω. Thus, any mode can be identified by the unique couple $(\vec{k}, n)$ where the *band number* n stands for the place in line of increasing frequency of the mode.

The operator related to the discrete translational symmetry is $\hat{T}_{\vec{R}}$ where $\vec{R} = \ell\vec{a}$ represents the displacement vector. This discrete symmetry can be thought of in terms of dielectric function, conisdering $\varepsilon(\vec{r}) = \varepsilon(\vec{r} + \vec{R})$. Notice that $\vec{R}$ cannot take any arbitrary value, rather it must be an integral multiple of the *lattice vector* $\vec{a}$, where $|\vec{a}|$ is the *lattice constant*. The eigenfunctions of this operator are plane waves of the form $exp(i\vec{k} \cdot \vec{R})$, exactly as it happened for the previous case. However there is a major difference compared to the continous symmetry. Indeed, consider a discrete translational symmetry along all three directions, so that $\vec{R} = Ua\vec{u}_x + Vb\vec{u}_y + Zc\vec{u}_z$ where a, b, and c are the lattice constants, and U, V, and Z are integers. Then it is possible to define a *reciprocal vector* $\vec{G} = L(2\pi/a)\vec{u}_x + M(2\pi/b)\vec{u}_y + N(2\pi/c)\vec{u}_z$ (with L, M, and N arbitrary integers). As a consequence, all the modes having wave vector equal to $\vec{k} + \vec{G}$ are degenerate, and therefore it is reasonable to consider the eigenfunctions of $\hat{\Theta}$ as linear combinations of those modes:

$$\vec{H}_{\vec{k}}(\vec{r}) = \sum_{\vec{G}} \vec{c}_{\vec{k},\vec{G}}(\vec{r}) \cdot e^{i(\vec{k}+\vec{G})\cdot\vec{r}} = e^{i\vec{k}\cdot\vec{r}} \sum_{\vec{G}} \vec{c}_{\vec{k},\vec{G}}(\vec{r}) \cdot e^{i\vec{G}\cdot\vec{r}} = e^{i\vec{k}\cdot\vec{r}} \cdot \vec{u}_{\vec{k}}(\vec{r})$$

where $\vec{u}_{\vec{k}}(\vec{r})$ is a periodic function, that is $\vec{u}_{\vec{k}}(\vec{r}) = \vec{u}_{\vec{k}}(\vec{r}+\vec{R})$ for any lattice vector $\vec{R}$. This

result is known as (optical) Bloch's theorem. Its validity implies that the mode frequencies must also be periodic: i.e. $\omega(\vec{k}) = \omega(\vec{k} + \vec{G})$. Thus, it is straightforward to define (first) *Brillouin zone* the region with non-redundant values of $\vec{k}$. Another relevant consequence of the theorem is that $\vec{k}$ is a conserved quantity modulo the addition of reciprocal lattice vectors. In this regard, considering a system with discrete translational symmetry, it is possible to substitute the result of the Bloch's theorem in the master equation, obtaining the following expression:

$$\begin{aligned} \nabla \times \frac{1}{\varepsilon(\vec{r})} \nabla \times e^{i\vec{k}\cdot\vec{r}} \vec{u}_{\vec{k}}(\vec{r}) &= (\omega(\vec{k})/c)^2 e^{i\vec{k}\cdot\vec{r}} \vec{u}_{\vec{k}}(\vec{r}) \\ (i\vec{k} + \nabla) \times \frac{1}{\varepsilon(\vec{r})} (i\vec{k} + \nabla) \times \vec{u}_{\vec{k}}(\vec{r}) &= (\omega(\vec{k})/c)^2 \vec{u}_{\vec{k}}(\vec{r}) \\ \hat{\Theta}_{\vec{k}} \vec{u}_{\vec{k}}(\vec{r}) &= (\omega(\vec{k})/c)^2 \vec{u}_{\vec{k}}(\vec{r}) \end{aligned}$$

where $\hat{\Theta}_{\vec{k}}$ has been defined as a new Hermitian operator. Because $\vec{k}$ is a continous parameter in $\hat{\Theta}_{\vec{k}}$, it is reasonable to expect that, for a fixed band index n, the frequency of each band varies continously with $\vec{k}$. Thus the modes of the system are a family of continous functions $\omega_n(\vec{k})$, and such functions define the *band structure* of the system.

1.2.2. 1D photonic crystals and gap opening

The simplest system with discrete translational symmetry is the *multilayer film*: it is a 1D photonic crystal made up of alternating layers with different dielectric constant ε_1 and ε_2. It is also possible to visualise this system as an infinite repetition of the dielectric waveguide along the z axis. Therefore, considering symmetry arguments, it is clear that modes can be classified using $\vec{k}_\parallel$, k_z, and n. Furthermore, assuming a spatial period a, the modes take the following Bloch form:

$$\vec{H}_{n,k_z,\vec{k}_\parallel}(\vec{r}) = e^{i\vec{k}_\parallel \cdot (x\vec{u}_x + y\vec{u}_y)} e^{ik_z z} \cdot u_{n,k_z,\vec{k}_\parallel}(z)$$

where $\vec{k}_\parallel$ can take any value, while k_z can be restricted to the first Brillouin zone, which in this case is defined as the interval $-\pi/a \leq k_z \leq \pi/a$. Thus, the band structure will be revealed by plotting $\omega_n(k_z)$ inside this interval. The computed band structure is presented in the following figure 1.9.

It is also possible to qualitatively deduce this result by employing heuristic arguments. Firstly, consider the case where $\varepsilon_1 = \varepsilon_2 = \varepsilon$: the system would become a homogeneous dielectric medium, with an arbitrary periodicity of a. Hence, the modes will have the known dispersion $\omega(k_z) = ck/\sqrt{\varepsilon}$, and because of the periodicity there will be a folding of

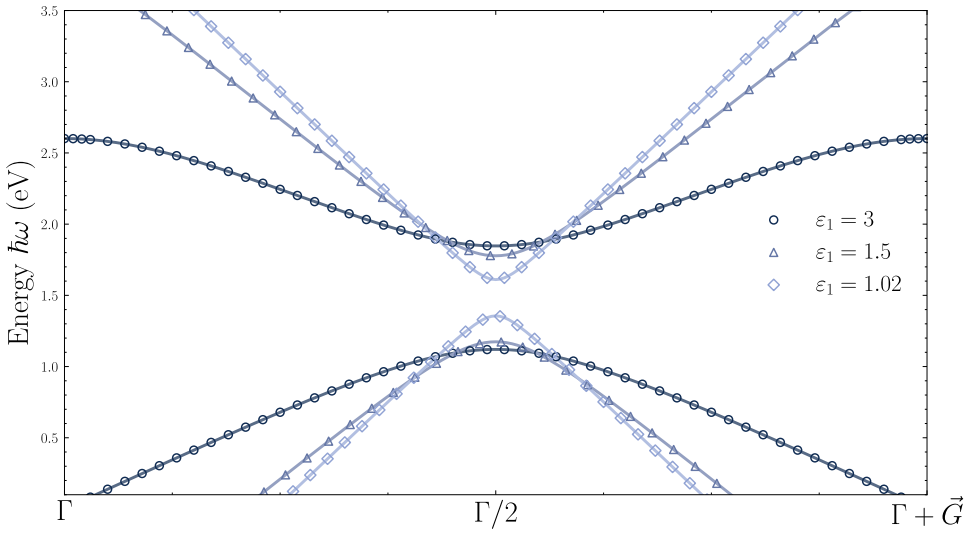

Figure 1.9: Simulation of the (scaled and shifted) dispersions for a period $L = 200$ nm, varying ε_1, and $\varepsilon_2 = 1$

the lines at the edge of the Brillouin zone. Then, consider the case where $\varepsilon_1 \neq \varepsilon_2$, but their difference is small. The picture above shows that such system has a dispersion relation almost the same as the previous one, with the important difference of manifesting a band gap, called *optical band gap*. The reason why this feature emerges can be understood by a simple argument: consider the profile of the electric field for the mode immediately above and below the gap. Since the gap lies at $k_z = \pi/a$ (i.e. at the edge of the Brillouin zone) the modes will necessarily have a periodicity of $2a$. There are only 2 ways of fitting modes with this period: either by placing the nodes in the ε_1 layers, or by placing them in the ε_2 layers. As a consequence, in the former case the energy of the mode will mostly be present in the ε_2 layers, while in the ladder case the energy will mostly be in the ε_1 layers.

The bending of the bands due to the discrete translational symmetry is a crucial point in this investigation. As shown in literature Troisi et al. [37], it is possible to use the e.m. field band structure to create a periodic potential for excitons, which results in their confinement, in a similar fashion to what can be achieved with more conventional potential generated by a crystalline structure [5].

1.2.3. Proposed structure: Fourier cavity

Having quickly explored various ways to confine light, it is now time to present the structures studied in this work: *Fourier cavities* [26]. Generally speaking, a Fourier

cavity is an optical cavity with at least a *Fourier surface*, i.e. a surface with a sinusoidal pattern.

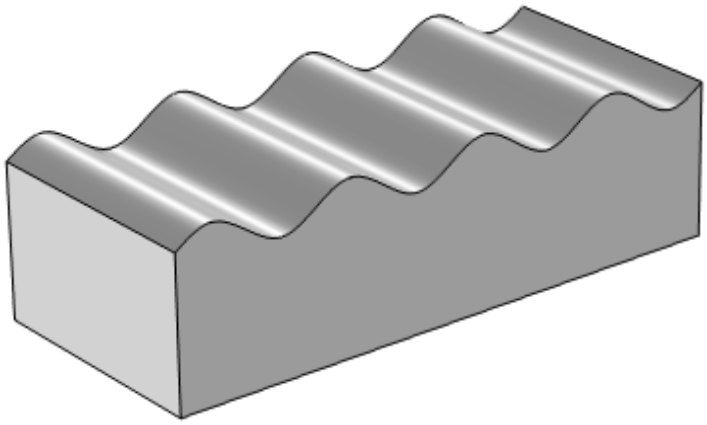

Figure 1.10: A sketch of the cavity

The core idea of this work is to place an active monolayer material, TMD, inside this structure, and let the vacuum quantum fluctuations, enhanced by the presence of the pattern, couple with the excitonic states of the 2D material. In principle, there could be a lot of different patterns that can achieve field confinement, with different efficiency each. Hence, the focus of this study falls on simple sinusoidal pattern because once its influence on the light has been assessed, then it would be possible to understand the effect of a more complicated pattern by combining the known effects of multiple Fourier components. Additionally, a basic design such as the one considered can be more easily fabricated in the laboratory.

The periodic pattern sets a discrete translational symmetry, which causes the formation of a band structure in the dispersion of light, as seen in the previous subsections. In this regard, there are a few parameters of interest: firstly, the period of the pattern L plays a fundamental role. Indeed, the light bands will repeat periodically in k space every $|\vec{G}| = 2\pi/L$, with the first Brillouin zone defined within the k interval $(-\pi/L, \pi/L)$. The larger the period in real space, the smaller the Brillouin zone, and vice versa.

Another relevant parameter is the thickness d of the cavity. Even if the exact relation between d and the properties of light confined depends on the particular kind of cavity considered, it is still fair to say that a larger thickness will be related to a longer wavelength in the electromagnetic excitation, while a smaller thickness to a shorter wavelength.

Lastly, the amplitude A of the pattern will be related to the symmetry properties of the system. Qualitatively speaking, a smaller amplitude will drive the structure toward the flat surface case, while an higher amplitude will enhance the features related to the periodicity.

2 | Chapter two: Light and matter interaction

2.1. Optical response of a material

As the aim of this work is to study the confinement of excitons via the interaction with the e.m. field, it is vital to understand how materials interact with it. In the following the role of excitons in the optical response will be discussed. It is important to mention that even if, in general, photon carry a momentum different than zero,in this section, for simplicity, it will be considered only the special case where excitons couple to zero momentum photons. In recent years, theories that consider the coupling with finite momentum photons are being developed, but the mathematical background to deal with them is more involved, and out of the scope of this work.

2.1.1. Dielectric function from the linear response theory

The analysis of the interaction with light is carried out with the help of the linear response theory. The underlying idea is that the linear response function tells how a given physical quantity changes when the system is subjected to a weak perturbation [36].

Within this framework, the *interaction picture* is employed. As a quick recap, it is relevant to mention that the overall hamiltonian $\hat{H}$ is split into $\hat{H}_0 + \hat{V}$, where the time-evolution of generic operator $\hat{A}$ is calculated using Heisenberg picture with respect to $\hat{H}_0$

$$\hat{A}_{\hat{H}_0}(t) = e^{i\hat{H}_0 t}\hat{A}(t)e^{-i\hat{H}_0 t}, \tag{2.1}$$

while the remaining time dependence due to $\hat{V}$ is carried out by Schroedinger picture:

$$|\psi(t)\rangle = U_I(\hat{t}, t_0)\,|\psi(t_0)\rangle \quad \text{with} \quad \hat{U}_I(t, t_0) = e^{i\hat{H}_0 t}\hat{U}(t, t_0)e^{-i\hat{H}_0 t_0} \tag{2.2}$$

Inserting the above expressions in the Schroedinger equation leads to:

$$\hat{U}_I(t,t_0) = \hat{T}exp\left[-i\int_{t_0}^{t}\hat{V}_{\hat{H}_0}(t')dt'\right] \tag{2.3}$$

where $\hat{T}$ is time-ordering operator (later goes left).

Assuming $\hat{V}(t) = e^{-i(\omega+i\eta)t}\hat{V}$ (i.e. scalar and harmonic time-dependence), it is possible to prove [14]:

$$\delta A(\omega+i\eta) = \sum_s \frac{\langle 0|\,\hat{A}\,|s\rangle\,\langle s|\,\hat{V}\,|0\rangle}{\omega-\omega_{s0}+i\eta} - \frac{\langle 0|\,\hat{V}\,|s\rangle\,\langle s|\,\hat{A}\,|0\rangle}{\omega+\omega_{s0}+i\eta} \tag{2.4}$$

Notice that A depends on the states $|s\rangle$, which are exact many-body eigenstates of $\hat{H}_0$. In the simpler case of non-interacting particles they are Slater determinants of single particle eigenstates from one particle hamiltonians; on the other hand, if the electrons are assuming to be interacting, then the eigenstates are not known.

In order to calculate the optical response, the main focus will be placed, among the many possible response functions, to the density response function. This function relates the change of density to the presence of an external perturbative potential. Assuming that $\hat{A} = \hat{n}(r)$ and that the external potential is $\hat{V} = \int V(r)\hat{n}(r)dr$, the *Kubo formula* can be written as:

$$\delta n(r,\omega) = \int \chi(r,r',\omega)V(r')dr' \tag{2.5}$$

where:

$$\chi(r,r',\omega) = \sum_s \frac{\langle 0|\,\hat{n}(r)\,|s\rangle\,\langle s|\,\hat{n}(r')\,|0\rangle}{\omega-\omega_{s0}+i\eta} - \frac{\langle 0|\,\hat{n}(r')\,|s\rangle\,\langle s|\,\hat{n}(r)\,|0\rangle}{\omega+\omega_{s0}+i\eta} \tag{2.6}$$

As mentioned before, in the case of non-interacting electrons $|s\rangle$ are not many-body eigenstate, rather they are Slater determinants of single-particle eigenfunctons $|\phi_i\rangle$. It is thus possible to define a non-interacting density response:

$$\chi^0(r,r',\omega) = \sum_{ij}(f_i-f_j)\frac{\phi_i(r)^*\phi_j(r)\phi_i(r)\phi_j(r')^*}{\omega-(\epsilon_j-\epsilon_i)+i\eta} \tag{2.7}$$

with $f_i = \theta(\epsilon_F - \epsilon_i)$ occupation number of orbital i.

In the case of a periodic system (a cristal, for example) it is convenient to work in reciprocal space, by taking the Fourier transform of χ with respect to both spatial component. In particular, if $Q = G + q$ with G reciprocal lattice vector, and q vector in the first BZ, it is

possible to show that any periodic function $f(r,r') = f(r+R, r'+R')$ is block diagonal in reciprocal space $f(G+q, G'+q') = f(G+q, G'+q')\delta_{qq'}$. Hence it can be written in compact form $f(G+q, G'+q') = f_{GG'}(q)$, which leads to:

$$\chi^0_{GG'}(q,\omega) = \sum_{nm}\sum_{k}(f_{nk} - f_{mk+q})\frac{\langle\phi_{nk}|\, e^{i(G+q)r}\,|\phi_{mk+q}\rangle\,\langle\phi_{mk+q}|\, e^{-i(G'+q)r}\,|\phi_{nk}\rangle}{\omega - (\epsilon_{mk+q} - \epsilon_{nk}) + i\eta} \tag{2.8}$$

In principle the main objective would be to calculate χ, but so far the only approximation is the non-interacting electron one, which is used to compute χ_0. It is now necessary to find a way to go from χ_0 to χ. a promising starting point would be to remember that it is possible to emulate interactions via effective potentials. There are many effective fields theory, with different approximations: some examples are Hartree-Fock (stronger approximations), and TD-DFT (theoretically exact).

Indeed, consider, within an Hartree-Fock approximation, the effective potential $v_s(r,t) = v_{ion}(r) + v_H(r,t) + v_{ext}(r,t)$ with:

$$v_H(r,t) = \int \frac{n(r',t)}{|r-r'|}dr' \tag{2.9}$$

$$v_{ext}(r,t) = v_{ext}(r)e^{-i(\omega+i\eta)t} \tag{2.10}$$

From

$$\delta v_s(r,\omega) = v_{ext}(r,\omega) + \int \frac{\delta n(r',\omega)}{|r-r'|}dr' \tag{2.11}$$

it follows:

$$\delta n(r,\omega) = \int \chi^0(r,r',\omega)\delta v_s(r',\omega)dr' \tag{2.12}$$

$$\delta n(r,\omega) = \int \chi(r,r',\omega)v_{ext}(r',\omega)dr' \tag{2.13}$$

and:

$$\chi(r,r',\omega) = \chi^0(r,r',\omega) + \int\int \chi^0(r,r',\omega)\frac{1}{|r_1-r_2|}\chi(r_2,r',\omega)dr_1dr_2 \tag{2.14}$$

A few remarks about this final result are in order: firstly, notice that the expression above is a *Dyson equation*, whose general form is $\chi = \chi^0 + \chi^0 v\chi$. Secondly, the approximation applied in this case is better known as *Random Phase Approximation* (or RPA in short) because we consider electrons "the Hartree way", i.e. neglecting exchange and correlation.

Finally, it is now necessary to calculate the dielectric function from the response function.

By definition, the *microscopic inverse* dielectric function is a response function that relates changes of the total potential to changes of the external (applied) potential:

$$\delta v_{tot}(r,t) = \int\int \varepsilon^{-1}(r,r',t-t')v_{ext}(r',t')dr'dt' \tag{2.15}$$

Notice that, in the same way of the responses above, also ε^{-1} is a retarded function. It is possible to take its Fourier transform:

$$\delta v_{tot}(r,\omega) = \int \varepsilon^{-1}(r,r',\omega)v_{ext}(r',\omega)dr' \tag{2.16}$$

where:

$$\delta v_{tot}(r,\omega) = v_{ext}(r,\omega) + \int \frac{\delta n(r',\omega)}{|r-r'|}dr' \tag{2.17}$$

Notice that $v_{tot} \neq v_s$ because v_s takes into account the exchange potential as well.

Considering the above expression, it is possible to write the inverse dielectric function explicitly:

$$\varepsilon^{-1}(r,r',\omega) = \delta(r-r') + \int \frac{\chi(r1,r',\omega)}{|r-r_1|}dr_1 \tag{2.18}$$

If the RPA is applied, the expression becomes:

$$\varepsilon^{-1}(r,r',\omega) = \delta(r-r') - \int \frac{\chi^0(r1,r',\omega)}{|r-r_1|}dr_1 \tag{2.19}$$

and its Fourier transform is:

$$\varepsilon^{-1}_{GG'}(q,\omega) = \delta_{GG'} - \frac{\chi^0_{GG'}(q,\omega)}{|G+q|^2} \tag{2.20}$$

2.1.2. Exciton contribution

The non-interacting particle picture works quite well in most situations, but it fails crucially, as the name suggests, when the influence of electrons on each other generates states with a significant contribution to the overall optical response. An important example of such states is the exciton: it is a quasi-particle born from the Coulomb interaction between an excited electron and a hole. In order to characterise it more precisely, it is convenient to start from the many body Hamiltonian for interacting electrons:

$$\hat{H} = \sum_i \frac{p_i^2}{2} - \sum_{i,I} \frac{Z_I}{|r_i - R_I|} + \frac{1}{2}\sum_{i\neq j} \frac{1}{|r_i - r_j|} \tag{2.21}$$

To make the calculations simpler, assume there are only two bands. In a one-electron picture (i.e. the non-interacting case), it would be enough to take a Slater determinant basis and the hamiltonian $\hat{H}$ would be diagonal. However, the equation above is for the many-bodies case, and thus one would need to find the many-body eigenstates $|s\rangle$. Because it is not possible to get them exactly, some approximation is in order. For instance, consider the ground state within a non-interacting system:

$$|\Psi_{GS}\rangle = |\phi_{vk_1}...\phi_{vk_N}\rangle \tag{2.22}$$

where

$$|\phi_{vk_1}...\phi_{vk_N}\rangle = \frac{1}{\sqrt{N!}} \det \begin{bmatrix} \phi_1(r_1) & \phi_2(r_1) & ... & \phi_N(r_1) \\ \phi_1(r_2) & \phi_2(r_2) & ... & \phi_N(r_N) \\ \vdots & \vdots & \ddots & \vdots \\ \phi_1(r_N) & \phi_2(r_N) & \dots & \phi_N(r_N) \end{bmatrix} \tag{2.23}$$

In order to avoid dealing with complicated many-body states $|s\rangle$, it is useful to consider the approximation of single excitations of the ground state. In simple terms, the ground state (GS) corresponds to a situation with no excitons; the 1^{st} excited state corresponds to a situation with one (single) exciton, and so on. By putting this idea into equations one gets:

$$|\Psi_k^{ex}\rangle = |\Psi_{GS,c\bar{v}k}\rangle = \hat{c}_{ck}^{\dagger}\hat{c}_{vk}\,|\Psi_{GS}\rangle \tag{2.24}$$

Note that this expression is valid only for a point k. In general:

$$|\Psi^{exc}\rangle = \sum_k A_k \hat{c}_{ck}^{\dagger}\hat{c}_{vk}\,|\Psi_{GS}\rangle \tag{2.25}$$

It is important to point out that, even if the assumption is that electrons and holes have either $k = 0$ or $k \neq 0$, in this approximation exciton are considered to have $q = 0$.

With the above basis set, it is now possible to solve the equation:

$$\langle\Psi_{GS}|\,\hat{c}_{vk}^{\dagger}\hat{c}_{ck}\hat{H}\,|\Psi^{exc}\rangle = EA_k \tag{2.26}$$

$$\tag{2.27}$$

which, after following known results from one- and two-body operators becomes:

$$\overbrace{(\epsilon_{ck} - \epsilon_{vk} - E)\,A_k}^{\text{kinetic + nuclei}} + \overbrace{\sum_{k'} U_{kk'}A_{k'}}^{\text{el-el repulsion}} = 0 \tag{2.28}$$

This expression is the two particle static approximation of the *Bethe-Salpeter Equation*, and it is a fundamental starting point for the treatment of exciton. It is also relevant to know that $U_{kk'}$, known as the *Coulomb kernel*, accounts for both the direct interaction

$$U_{d,kk'} = -\langle \phi_{ck}(r_1)\phi_{vk'}(r_2)|\, 1/r_{12}\, |\phi_{ck'}(r_1)\phi_{vk}(r_2)\rangle \tag{2.29}$$

and the exchange interaction

$$U_{ex,kk'} = \langle \phi_{ck}(r_1)\phi_{vk'}(r_2)|\, 1/r_{12}\, |\phi_{vk}(r_1)\phi_{ck'}(r_2)\rangle \tag{2.30}$$

Although there are numerical method to solve the Bethe-Salpeter equation, in order to proceed analytically it is necessary to consider a few approximations: first $U_{ex,kk'}$ is neglected; then the system is assumed to be a bulk-like crystal, hence single-particle functions are $\phi_{vk}(r) = e^{ikr}u_{vk}(r)$; also the approximation $u^*_{ck}(r)u_{ck}(r) \simeq \frac{1}{V}\langle u_{ck}|u_{ck'}\rangle \simeq \frac{1}{V}$ will be employed. Lastly, the bands are assumed to be parabolic:

$$\epsilon_{ck} = E_G + \frac{k^2}{2m_e} \tag{2.31}$$

$$\epsilon_{vk} = -\frac{k^2}{2m_h} \tag{2.32}$$

Thus

$$\epsilon_{ck} - \epsilon_{vk} = E_G + \frac{k^2}{2\mu_{ex}} \tag{2.33}$$

where the excitonic effective mass is defined as $\mu^{-1}_{ext} = m_e^{-1} + m_h^{-1}$. As a consequence the Coulomb kernel becomes:

$$U_{d,kk'} = -\frac{1}{V}\int \frac{e^{-ir(k-k')}}{r}dr = -\frac{1}{V}\frac{4\pi}{|k-k'|^2} \tag{2.34}$$

Even if this expression is sound, there is a practical problem: when simulating a system of many particles, such as a solid, this expression becomes problematic, as all the particles, even if relatively far apart, always interact with one another. Because the reality is different, as charges screen one another, it is common to make the assumption of having a screened potential in the form:

$$U^{screen}_{d,kk'} = -\frac{1}{V}\frac{4\pi}{\varepsilon|k-k'|^2} \tag{2.35}$$

Notice that the screeing term added at the denominator is none other the dielectric

function calculated in the previous subsection. In this way, there is effectively a first link between the excitons and the optical response to a field.

Substituting eq. 2.34 and taking into account all the approximation discussed, eq. 2.28 becomes

$$\left(E_G + \frac{k^2}{2\mu_{ex}} - E\right) A_k - \frac{1}{V}\sum_{k'} \frac{4\pi}{\epsilon|k-k'|^2} A_{k'} = 0 \tag{2.36}$$

By taking the Fourier transform of A_k one gets:

$$F(r) = \frac{1}{\sqrt{V}}\sum_k A_k e^{ikr} \tag{2.37}$$

From here, it is possible to derive the *hydrogenic equation*:

$$\left[-\frac{\nabla^2}{2\mu_{ex}} - \frac{1}{\epsilon \cdot r}\right] F(r) = (E - E_G)F(r) \tag{2.38}$$

where the term $W(\boldsymbol{r}) = \frac{1}{\epsilon \cdot r}$ takes into account the screened electron-hole interaction. Because, as the name suggest, this equation resembles closely the one used for the hydrogen atom, also their solution will be similar. It relevant to mention that eq. 2.38 in the case of 2D materials takes the form:

$$\left[-\frac{\nabla^2}{2\mu} - W(\boldsymbol{r})\right] F^n(\boldsymbol{r}) = E_b^n F^n(\boldsymbol{r}) \tag{2.39}$$

$$W(\boldsymbol{r}) = \frac{1}{4\alpha}\left[H_0(x) - N_0(x)\right]_{x=r/2\pi\alpha} \tag{2.40}$$

with W screened Coulomb interaction written in terms of the *Keldysh interaction*, which employs the Struve and Neumann functions H_0 and N_0 respectively; α is the crystal polarizability. The reason behind the difference from the 3D case, is that in 2D the screened interaction is:

$$U_{d,kk'}^{screen2D} = -\frac{1}{A}\frac{4\pi}{\varepsilon|k-k'|}, \tag{2.41}$$

which is different than 2.35, where the scaling over $|k-k'|$ was squared. As a consequence 2D materials have a non-local response, which is often found in the form:

$$\varepsilon_{2D}(k) = 1 + \alpha k \tag{2.42}$$

2.1.3. Coupled exciton-light problem

Equipped with the description of the exciton, it is now time to move on the exploration of the exciton-light coupling. In order to properly describe their interaction, it is necessary to consider a quantisation of the electromagnetic (e.m.) field: here, the field is quantised via the interaction potential $\hat{\vec{A}}$. The e.m. field hamiltonian added to the many body one generates:

$$\hat{H}_{QED} = \overbrace{-\frac{\left(\hat{\vec{p}} - e\hat{\vec{A}}\right)^2}{2m} - \hat{W}}^{\text{matter + field inside}} + \overbrace{\omega\left(\hat{a}^\dagger\hat{a} + \frac{1}{2}\right)}^{\text{free field, light}} \tag{2.43}$$

with $\hat{\vec{p}}$ momentum, $\hat{\vec{A}}$ vector potential, $\hat{W}$ scalar potential in the matter, and $\hat{a}$, $\hat{a}^\dagger$ annihilation and creation operators, respectively. The expression above can be written more explicitly as:

$$\hat{H}_{QED} = \hat{H}_{el} + \omega\left(\hat{a}^\dagger\hat{a} + \frac{1}{2}\right) + \hat{\vec{p}}(\hat{a}^\dagger + \hat{a}) + \frac{A_0^2}{2}(\hat{a}^\dagger + \hat{a})^2 \tag{2.44}$$

The last term of $\hat{H}_{QED}$ can be re-written as:

$$\frac{A_0^2}{2}(\hat{a}^\dagger + \hat{a})^2 \propto \overbrace{2\hat{a}^\dagger\hat{a} + 1}^{\text{diagonal}} + \overbrace{\hat{a}^{\dagger 2} + \hat{a}^2}^{\text{BT}} \tag{2.45}$$

where BT stands for *Bougoliov Transform*, which is used to reshape the terms to fit into the free field component. As a consequence, that contribution ends up re-normalizing the frequency $\omega \to \Omega$, and equation 2.44 then becomes:

$$\hat{H}_{QED} = H_{el} + \Omega\left(\hat{a}^\dagger\hat{a} + \frac{1}{2}\right) + A_0\sum_{i,j,\vec{k}}\left(\left\langle\phi_{i\vec{k}}\right|\hat{\vec{e}}\cdot\hat{\vec{p}}\left|\phi_{j\vec{k}}\right\rangle\hat{d}^\dagger_{i\vec{k}}\hat{d}_{j\vec{k}}\hat{a}^\dagger + h.c.\right) \tag{2.46}$$

where $\hat{d}^\dagger_{i\vec{k}}$ and $\hat{d}_{j\vec{k}}$ are electronic creation and annihilation operators (respetctively) with band index i,j. Firstly, although the full expression of the vector potential is

$$\hat{\vec{A}} = A_0 e^{i\vec{q}\cdot\vec{r}}(\hat{a}^\dagger + \hat{a}) \tag{2.47}$$

the $e^{\cdots}$ term has been neglected in virtue of the *long wavelength approximation*, or long-wavelength electron-photon coupling. It is relevant to mention that this assumption, despite its wide use, is not without some issues: to be precise, if carried too far, it results in action having a speed $v \to \infty$, which is clearly non-physical. Secondly, the cavity is assumed to host only a single mode having a frequency ω, and to be lossless.

In order to go forward and to make the problem easier to handle analytically, it is possible to make the additional approximation of non-interacting excitons (which is fairly reasonable for non-pumped cavities). In other words, it shall be assumed:

$$\hat{H}_{el}\left|\Psi_n^{exc}\right\rangle \approx \epsilon_n^{exc}\left|\Psi_n^{exc}\right\rangle \quad \text{where} \quad \left|\Psi_n^{exc}\right\rangle = \sum_{cv\vec{k}} A^n_{cv\vec{k}}\hat{d}^\dagger_{c\vec{k}}\hat{d}_{v\vec{k}}\left|\Psi_0\right\rangle \tag{2.48}$$

which, in simple terms, means that $\left|\Psi_n^{exc}\right\rangle$ is a linear combination of singly excited electronic determinants, and ground state $\left|\Psi_0\right\rangle$ is a single determinant.

Furthermore, by assuming that the electron-hole Coulomb interaction is not affected by the photons (even tough it is not fully true), one can write:

$$\left\langle\Psi_n^{exc}\right|\hat{H}_{QED}\left|\Psi_m^{exc}\right\rangle = \left[\epsilon_n^{exc} + \Omega\hat{a}^\dagger\hat{a} + N_{el}\frac{A_0^2}{2}(\hat{a}^\dagger+\hat{a})^2\right]\delta_{nm} + A_0\left(\mathcal{M}^{exc}_{nm}\hat{a}^\dagger + \mathcal{M}^{exc*}_{mn}\hat{a}\right) \tag{2.49}$$

where the excitonic matrix elements are:

$$\mathcal{M}^{exc}_{nm} = \sum_{ij\vec{k}}\left\langle\phi_{i\vec{k}}\right|\hat{e}\cdot\hat{p}\left|\phi_{j\vec{k}}\right\rangle\left\langle\Psi_n^{exc}\right|\hat{d}^\dagger_{i\vec{k}}\hat{d}_{j\vec{k}}\left|\Psi_m^{exc}\right\rangle \tag{2.50}$$

At last, excitonic states are considered non-dispersive (momentum independent): that is, the excitonic states are described by spin-independent 2-bands BSE, where only a single valence and a single conduction bands are taken into account. As a consequence $\mathcal{M}$ elements can only have two general expressions:

$$\mathcal{M}^{exc}_{0n} = \sum_{\vec{k}} A^n_{\vec{k}}\left\langle\phi_{v\vec{k}}\right|\hat{e}\cdot\hat{p}\left|\phi_{c\vec{k}}\right\rangle \tag{2.51}$$

or

$$\mathcal{M}^{exc}_{mn} = N_{el}\sum_{\vec{k}} A^{m*}_{\vec{k}}A^n_{\vec{k}}\left[\left\langle\phi_{c\vec{k}}\right|\hat{e}\cdot\hat{p}\left|\phi_{c\vec{k}}\right\rangle - \left\langle\phi_{v\vec{k}}\right|\hat{e}\cdot\hat{p}\left|\phi_{v\vec{k}}\right\rangle\right] \tag{2.52}$$

The first terms determines if the exciton is bright or dark, while the second determines the mixing nature (i.e. the transition bright to dark or vice versa).

The next step would be to diagonalise the matrix obtained by projecting onto the mixed exciton-photon basis $\left|\Psi_n^{exc}\right\rangle\otimes\left|\gamma\right\rangle$. The exciton-polariton eigenfunction will then be:

$$\left|\Psi_I^{pol}(\Omega)\right\rangle = \sum_{n\gamma} C^I_{n\gamma}\left|\Psi_n^{exc}\right\rangle\otimes\left|\gamma\right\rangle \tag{2.53}$$

Consistently with the previous exploration of the exciton behaviour, in order to proceed analytically a Mott-Wannier (MW) model shall be considered. The first consequence is that excitons are very localised and therefore the valence-conduction momentum matrix elements are constant:

$$\mathcal{M}_{0n}^{exc} = \langle \phi_{vK} | \, \hat{e} \cdot \hat{p} \, | \phi_{cK} \rangle \, F(\vec{r} = \vec{0}) \tag{2.54}$$

Further, assuming parabolic conduction and valence bands leads to:

$$\langle \phi_{vK} | \, \hat{e} \cdot \hat{p} \, | \phi_{vK} \rangle = \hat{e} \cdot \frac{d}{d\vec{k}} \epsilon_{v\vec{k}} = -\frac{k}{m_b} \tag{2.55}$$

$$\langle \phi_{vK} | \, \hat{e} \cdot \hat{p} \, | \phi_{vK} \rangle = \hat{e} \cdot \frac{d}{d\vec{k}} \epsilon_{v\vec{k}} = -\frac{k}{m_b} \tag{2.56}$$

$$\mathcal{M}_{mn}^{exc} = \left[\frac{1}{m_h} + \frac{1}{m_e} \right] \sum_{\vec{k}} A_{\vec{k}}^{m*} A_{\vec{k}}^{n} \, \hat{e} \cdot \vec{k} \tag{2.57}$$

By taking into account these expressions, the optical response is:

$$\sigma(\omega, \Omega) = \sum_{i} \frac{\mathcal{M}_{0n}^{pol} \mathcal{M}_{I0}^{pol}}{\omega - E_I^{pol}(\Omega) + E_0^{pol}(\Omega) + i\eta} \tag{2.58}$$

2.2. Materials of the Fourier cavity

The idea behind the making of a cavity is to confine the e.m. field inside so that its amplitude can be greatly enlarged and therefore the coupling with the excitons increases. The cavity can be thought as made from two parts: an active medium, where excitons live, and the cladding around. The properties of both these materials need to be considered carefully: indeed, excitons behave differently depending on the active medium they live in, while having different cladding leads to different kinds of confinement of the e.m. field (namely, total internal reflection, surface plasmon polaritons, and hyperbolic polaritons). Therefore, in the following, a study of two candidate materials is carried out: for the active material its band structure and its optical response (in terms of the polarizability), both with and without excitonic contributions, will be presented. Regarding the cavity material, besides the computation of its band structure, the analysis will be centered on the extraction of parameters useful for the COMSOL® implementation of the hyperbolic cavity. Indeed, in that case, the hBN response will be approximated as a single pole Lorentz function (see subsection 3.3.1), where the values of its parameters ω_{px}, ω_{px}, ω_{px}, and ω_{px} will be computed in this section.

2.2.1. 2D materials as active medium

One of the most interesting class of bidimensional materials are the *transitional metal dichalcogenides*, also known as TMDs: the name comes from the fact that they all share a formula of the type MX_2 where M stands for a metal element, while X is an element of the chalcogen family. Hence, a first reason why these compounds are so widely studied: the possibility of combining different elements in countless combination opens the door for a huge variety of novel materials which may carry intriguing properties. Note also that the properties of a TMD bulk material are often different than that of same monolayer material. Another characteristic is the possibility of stacking up different TMDs one on top of the other, and, via Van der Waals interaction, they will form a heterostructure with again new properties. Lastly, because of their lower dimensionality, there is less dieletric screening, compared to the standard isotropic bulk scenario, and therefore the contribution of excitons, surface plasmons, and polaritons is more relevant.

One of the candidates for the active material is tungsten disulfide WS_2, shown in the picture above. Its single-layer structure can be found in either rhombohedral or hexagonal symmetry: in this study the latter will be analysed.

Because the aim of this work is to present a fully theoretical simulation, instead of relying

(a) Top view (b) Side view

Figure 2.1: Sketch of monolayer WS_2 crystal structure: tungsten atoms in dark blue, while sulfur atoms in light blue

on experimental data, the properties of the materials considered are calculated ab initio. In this study such calculations are performed with the GPAW software [30] [40] [24] [25] [3]

The first step towards the understanding of this material is the study of its electronic band structure. The computation is carried out on a 8 by 8 by 8 k-points grid, with a PBE functional, and an energy cut-off of 200 eV; furthermore, a spin-orbit correction is included, and the plotting of the bands is spin resolved.

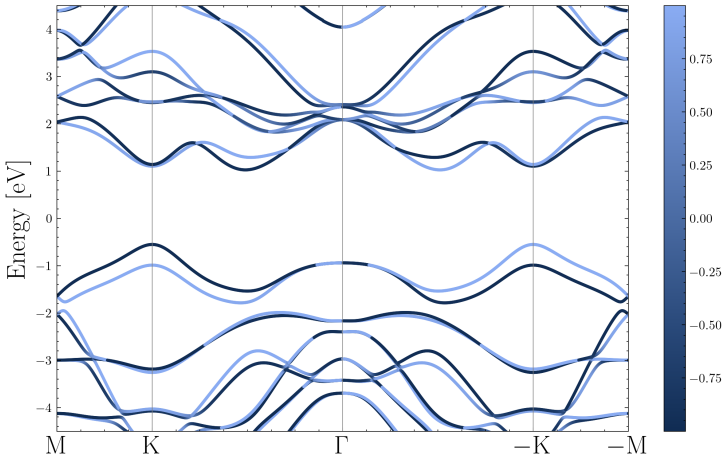

Figure 2.2: Spin resolved band structure

Being a standard DFT calculation without GW_0 correction, the band gap is quite smaller than the experimental one. Nonetheless, there are quite a few features to notice. First of all, the band gap: from the picture it is clear that monolayer WS_2 has a direct band gap. This propriety marks a significant difference from its bulk form, where the band gap is indirect. Another noticeable feature is the spin-orbit splitting of the valence bands at the K point: the splitting of the bands causes a removal of the degeneracy, so that spin up

and spin down electrons have different energies. Further, it is relevant to consider that the spin-splitting at the valence peaks of two adjacent K points, as depicted in the image above, is inverted. This feature leads to interesting phenomena: for example light having right-hand, or left-hand, polarization excites selectively electrons belonging to only one peak [42].

Further characteristic of this material can be seen by considering its optical response [40]. As a first step consider the random phase approximation RPA, where electrons interact with each other via an effective potential. As stated in previous chapters, because the dielectric function is not really well defined for 2D system, it is convenient to consider the polarizability α instead (which is well defined). Under such conditions, the optical response, proportional to the absorption, becomes:

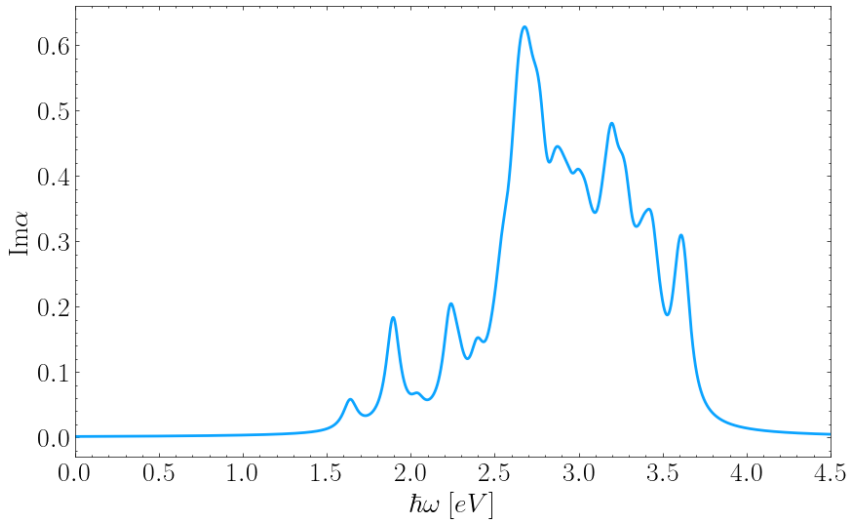

Figure 2.3: Optical response computed under RPA

Notice the onset is a little above 1.5 eV, which corresponds to the computed gap, as shown in figure 2.2.

In order to get a more precise result, it is also possible to take into account excitonic effect through the Bethe-Salpeter equation. In this new case, the optical response changes significantly:

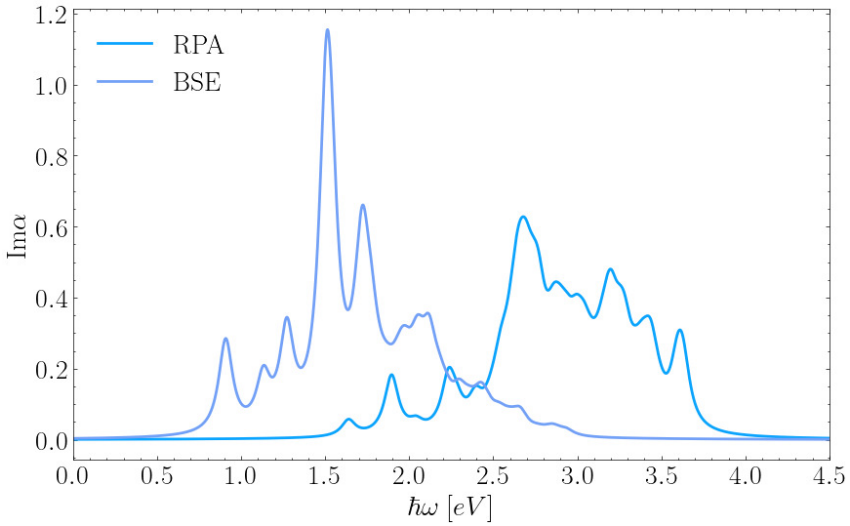

Figure 2.4: Optical responses computed under RPA and BSE

The excitonic contribution can be clearly seen through the new peaks appearing inside the gap: that is because the new approximation takes into account the presence of such bound states.

2.2.2. Hexagonal Boron Nitride as cavity material

In this work, the choice of the material for the cavity falls under hexagonal boron nitride, or hBN in short. It is a layered crystal, made up of monoatomic sheets where the atoms are arranged in an hexagonal structure, much like graphite is made up of graphene sheets, except for the fact that hBN doesn't have carbon atoms, but boron and nitrogen ones, alternating in the hexagonal pattern.

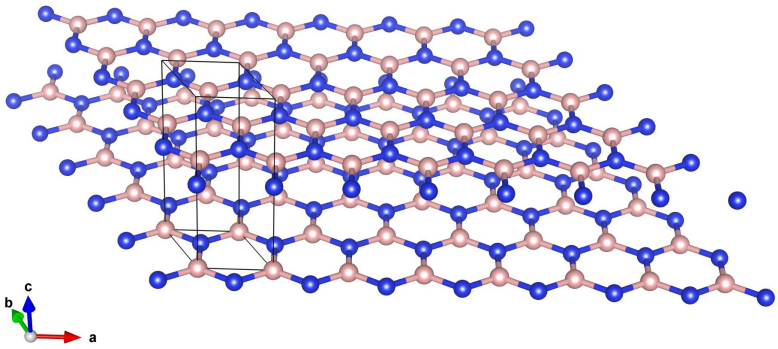

Figure 2.5: Sketch of the crystalline structure of hBN

This material is a semi-transparent anisotropic dielectric, with a diagonal dielectric tensor that can be expressed as:

$$\overline{\overline{\varepsilon}} = \begin{bmatrix} \varepsilon_{\parallel}(\omega) & 0 & 0 \\ 0 & \varepsilon_{\perp}(\omega) & 0 \\ 0 & 0 & \varepsilon_{\parallel}(\omega) \end{bmatrix} \tag{2.59}$$

As shown in the notation, it is possible to find an isotropic plane, where every direction is equivalent, and a perpendicular axis, where the behaviour changes.

In order to better understand the properties of this material, it is necessary to study it in a more quantitative way. Therefore, in the following, there will be presented ab initio calculations, computed via the Quantum Espresso software [10] [11] [11]. First of all, consider the band structure, shown in figure 2.6:

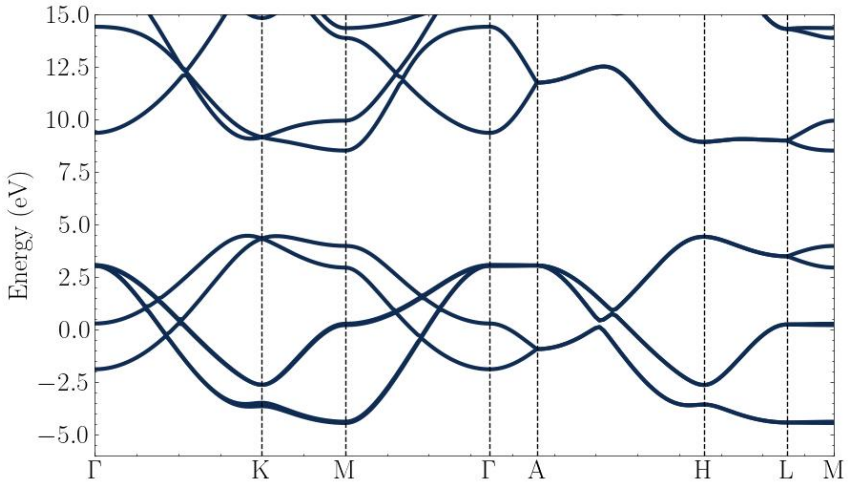

Figure 2.6: Band dispersion diagram for bulk layered hBN

Notice that the size of the band gap does not correspond to the experimental measurement, because the calculation are carried out without the GW correction to DFT. Besides the value of the gap, these band structure is in full agreement with the literature reference [35]. Then, as a next step, the optical response should be calculated. However, as stated in the introduction to this section, the focus is on the hyperbolic response. Indeed, the parallel and perpendicular components of the dielectric tensor of hBN in the far IR frequency are dominated by the phononic response, and they can be well approximated by the expressions:

$$\varepsilon_{\parallel}(\omega) = \varepsilon_{\infty\parallel}\left(1 - \frac{\omega_{LO\parallel}^2 - \omega_{TO\parallel}^2}{\omega^2 - \omega_{TO\parallel}^2 + i\gamma_{\parallel}\omega}\right) \tag{2.60}$$

$$\varepsilon_{\perp}(\omega) = \varepsilon_{\infty\perp}\left(1 - \frac{\omega_{LO\perp}^2 - \omega_{TO\perp}^2}{\omega^2 - \omega_{TO\perp}^2 + i\gamma_{\perp}\omega}\right), \tag{2.61}$$

where the frequencies marked as "LO" or "TO" refer respectively to the *longitudinal optical* and *transverse optical* phonon frequencies. In the hBN bulk crystal happens that the phonon branches couple with the photons, giving rise to a polaritonic state. One of the consequence is the energy splitting between the resonance frequencies of the longitudinal phonon modes and the transverse ones [15]. Moreover, the peculiarity of hBN is that this splitting happens at different energies along the two principal axes: these phenomenon lies at the core of the formation of hyperbolic polaritons. It is therefore fundamental for the simulation of the hyperbolic cavity the ab initio calculations on the values of the parameters appearing in the equations above. In order to do so, the Quantum Espresso code is preferred over the GPAW code, because the former implement the LO-TO correction, not present in the latter. The results of such calculations is the phonon dispersion, shown in figure 2.7.

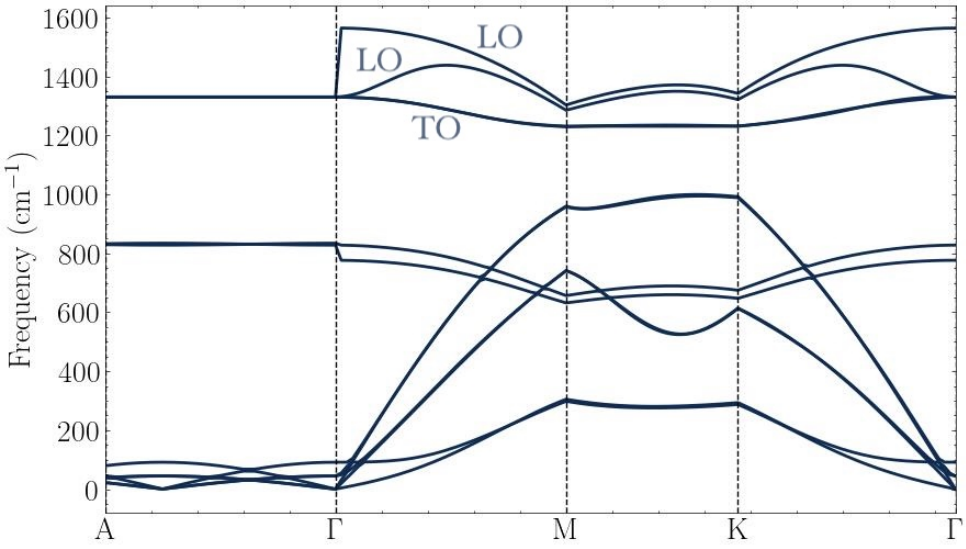

Figure 2.7: Phononic dispersion relation; LO and TO modes are indicated by the labels

Notice the splitting of the LO and TO branches at the Γ point. These dispersion is in full agreement with similar calculations in literature [29]. The phonon calculations, are also in agreement with the reference values [2]:

$$\omega_{LO\parallel} = 200meV \quad \omega_{TO\parallel} = 168meV \quad \omega_{LO\perp} = 103meV \quad \omega_{TO\perp} = 94meV$$

Hence, the plot of the dielectric functions in equations 2.60 and 2.61 is shown in figure 2.8:

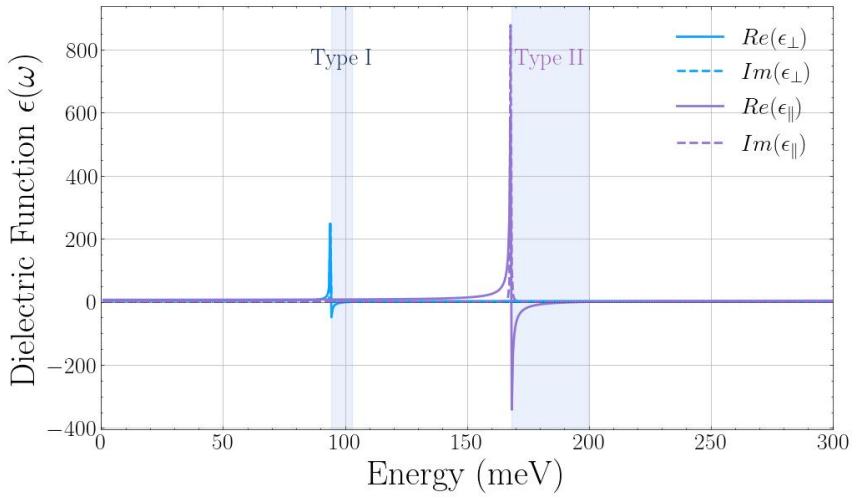

Figure 2.8: Plot of the parallel and perpendicular term of hBN's dielectric tensor; the values of the γ parameters are arbitrary

It is important to mention that the values of the γ parameters, which determine both the broadening and the height of the peaks, have been artificially set.

Having a full description of the material that constitute the core of the optical cavity, it is now possible to address the electromagnetic field simulations, discussed in the next chapter.

3 | Chapter three: Numerical Simulations

After having discussed how the electromagnetic field behaves inside cavities with a simple geometry, it is now time to study its behaviour inside a Fourier cavity. Because an analytical approach is out of question for the arbitrary geometry, in this section numerical simulations will be employed to find the eigenmodes of the electromagnetic field inside different kind of Fourier cavities. The main challenge of the study, the numerical methods, will have their own dedicated subsections.

All the simulations are achieved using the software COMSOL® [1], and the extracted data are plotted with Python scripts.

3.1. Dielectric waveguide

The first kind of Fourier cavity taken into consideration is a dielectric waveguide made of an hBN core and a glass cladding, where the surface between the core and the top cladding has been shaped into a sinusoidal pattern. As seen in section 1.2, it is expected to see a bending of the dispersion relation, and the opening of an energy gap. In the following subsection firstly there will be a discussion on the numerical methods necessary for the simulations, and then the simulations results will be presented.

3.1.1. Numerical treatment

The simulations are carried out using the RF module paired with an eigenfrequency study in a 2D environment. The system is modeled as a single column of 3 main layers: the one representing hBN is sandwiched between the other two, which represent the cladding around. Between the core and the top cladding there is an additional layer that represents the patterned PPA resist: the sinusoidal pattern has an amplitude A, with its lowest point sitting at a distance H from the hBN. Moreover, scattering boundary conditions are additionally placed at the top and bottom edges, while the left and right boundaries

have Floquet periodic boundary condition with k vector k_x. The RF module solves for all three (complex, in general) components of the e.m. field. In order to obtain the dispersion relation, a parametric sweep over values of $k_x \in (0, G)$, with $G = 2\pi/L$ and L period length, is applied to the eigenfrequency study.

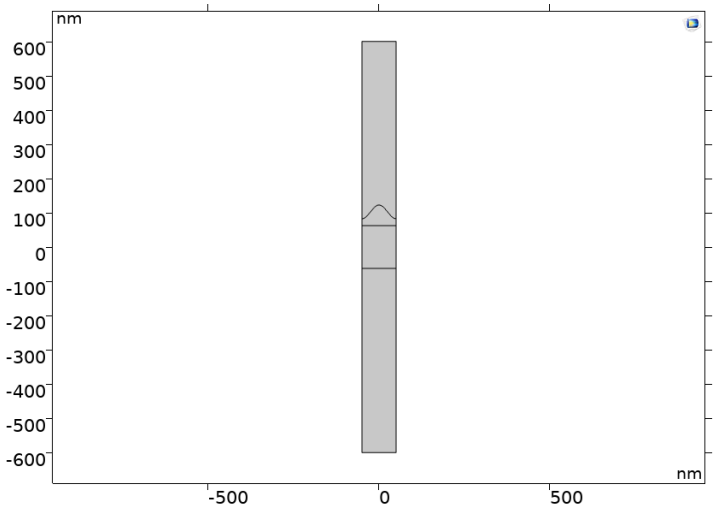

Figure 3.1: Picture of the model

In figure 3.1 a sketch of the structure and in figure 3.2 of the parameters discussed.

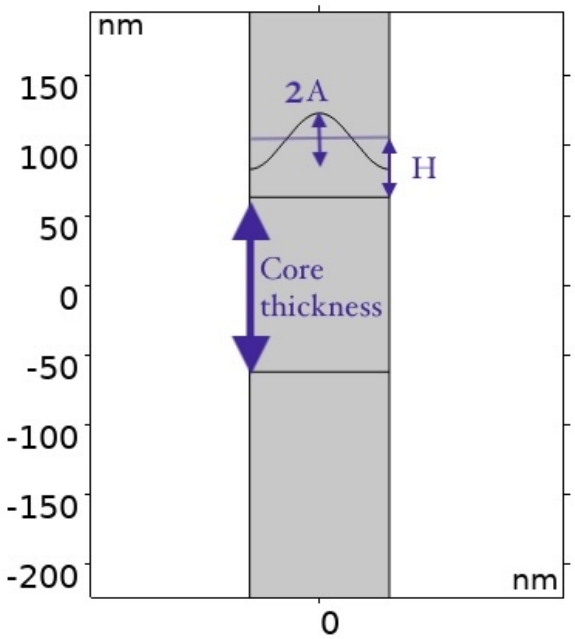

Figure 3.2: Sketch of the strcture, with parameters indicated

3.1.2. Simulations

An example of the results of the simulation is presented in the following, all the other plots are in the appendix B

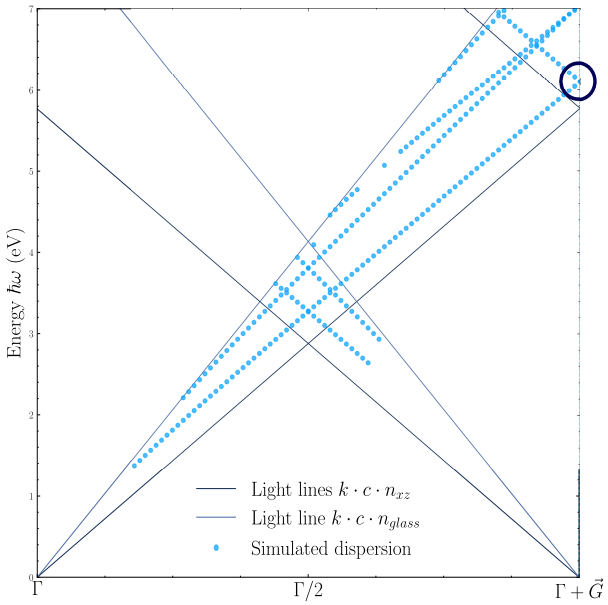

Figure 3.3: Simulation with a period of 100 nm, T = 100 nm, H = 20 nm, A = 20nm; the circle marks the region where the gap is

As a guide for the eye the figure shows the light lines with slope n_{xz} and n_{glass} at the two Γ points: indeed, as shown in section 1.1.2, it is known that the guided modes are confined within the light cone with slopes equal to the refractive indices of the core and of the cladding, and that the dispersion relation is periodic, with a period equal to $\vec{G}$. However, before beginning any further analysis, it is relevant to consider that these plots are post-processed. The reason is that, because the simulation box is finite and very big, there are a lot of box-states solutions: they stem from the fact that the simulation box acts as a Fabry-Perot cavity. Because the eigensolver cannot discriminate between the box-states and the actual dielectric waveguide modes, and since the density of the former states is higher, it finds mostly box-states. This behaviour brings a few consequences. Firstly, the eigenvalue solver needs to be instructed to look for frequency around the first cone, and not in all the $\hbar\omega$ vs k space. Therefore, even if theoretically all the modes present in the cone generated at the Γ point should be exactly mirrored in the cone generated at the $\Gamma + \vec{G}$ point, the simulation favour the modes living in the cone at the left Γ point. Secondly, it is necessary to clean the resulting data, in order to show (mostly) only the guided modes, while filtering out the box-states. Hence, it is used a filter that exploits

the quality factor $Q = Re\{f\}/2Im\{f\}$, which can be thought of as a measure of the confinement of the e.m. field: the guided modes have a high Q factor, since they are mostly confined in the core region; on the other hand the box-states are widely spread trough all the box length, thus resulting in a low Q factor.

The first thing to notice is that the periodic structure has a very clear effect on the dispersion: the lines generated near the Γ point are mirrored in the $\Gamma+\vec{G}$ point, and there is some crossing (which is actually a bending) at the $\Gamma/2$ and $\Gamma+\vec{G}$ points. However, to better understand what is happening, it is necessary to know some characteristics of the simulations itself. Firstly, the lines representing the 0-th mode show a threshold (that is, they don't stretch to the zero energy point), even if they theoretically should. The reason is that the complete stretch to zero energy is true in an infinite space; on the other hand, the simulations are carried out in a box which, albeit much larger compared to the system size, is not infinite: as a consequence there is minimum energy threshold.

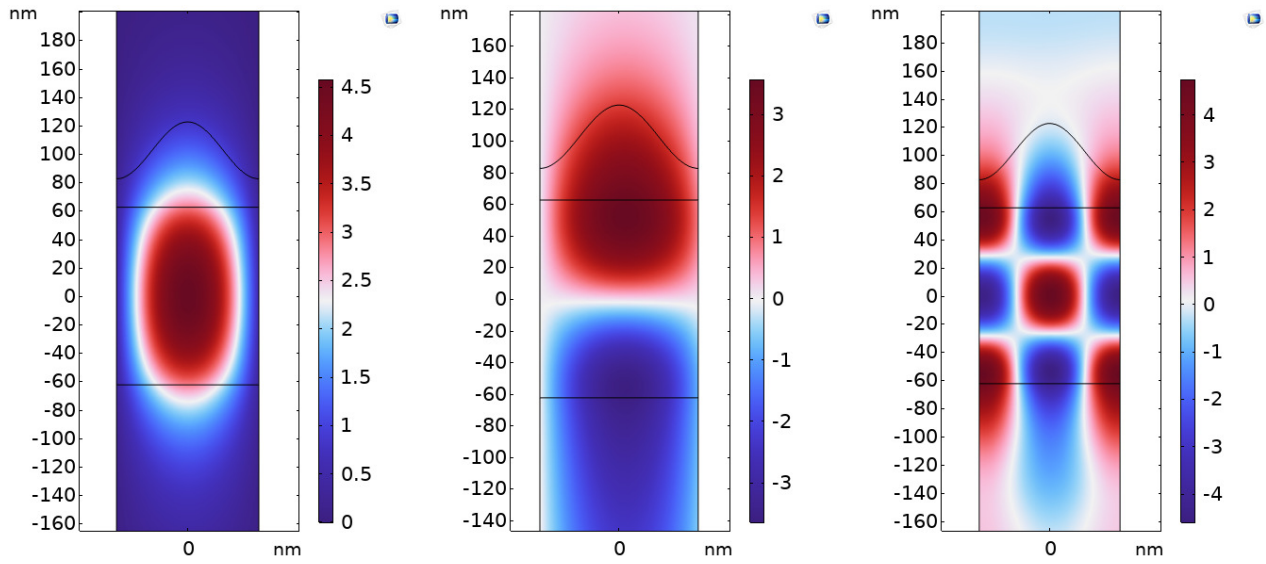

(a) 0-th mode (b) 1-st mode (c) 2-nd mode

Figure 3.4: Profile of the E_z component for the first three TE modes; colour scale in V/m

Above, it is possible to see the field profile of the first three TE modes. Notice that the the numbering of the modes is given by their vertical periodicity, while the horizontal one is a byproduct of the numerical simulations. From those pictures it looks like this kind of cavity does not confine the electromagnetic field efficiently: indeed the colour scale shows relatively small amplitudes of the field: they are comparable to the amplitudes of the box states, which are not confined at all.

Because, at the naked eye, all the dispersion plots (see Appendix B) look the same, in

order to further analyse these results, it is necessary to approach the data in a more quantitative way. First of all, the choice considered is that the quantity of interest is the lowest band gap produced at the $\Gamma + \vec{G}$ point due to the bending of the bands (the position of the gap is highlighted by the blue circle in the picture 3.3; note that its size makes the gap itself to little to be seen with a naked eye). The reason for the interest is that the size of the gap is a measure of the bending of the bands: the bigger it is, the more bent the bands will be, and thus the higher the likelihood for the exciton to couple to periodic modes.

Considering the simulations with varying core layer thickness in Appendix B from a) to e), it is possible to see how this parameter influences the gap.

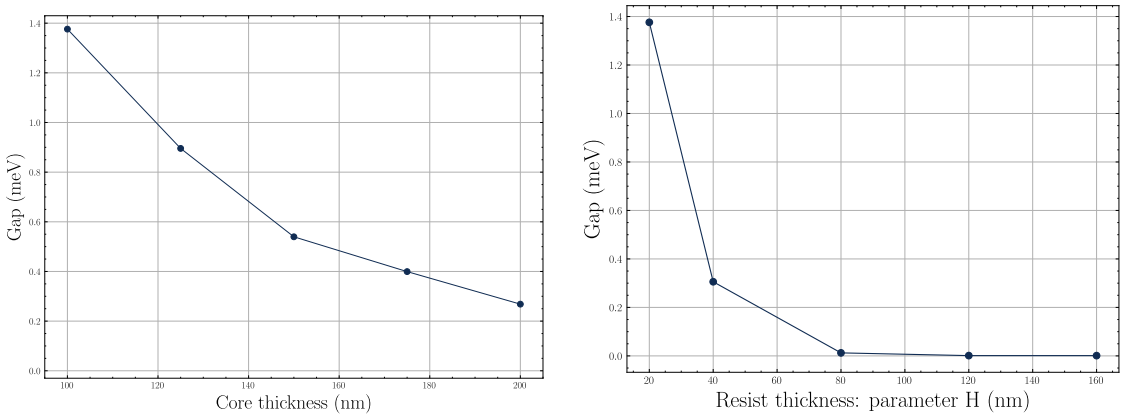

(a) Gap vs T (b) Gap vs H

Figure 3.5: Variation of the gap against T and H

As expected, the gap decreases as the thickness grows: this behaviour can be understood by considering that, as the thickness gets higher, the size of the pattern becomes relatively smaller, hence moving the simulation towards the flat case, where the bands do not bend and therefore the gap is null.

Notice also the order of magnitude of the gap's size: it is around 1 meV. This value explains why at the naked eye the bands seemed to cross instead of bend.

Similarly happens if the minimum core-pattern distance is increased, as shown in figure 3.5b. Also in this case the gap decreases the higher the parameter gets. Indeed, a similar argument can be made: as this distance H increases, the smaller (relatively) the pattern becomes, driving the simulation again towards the flat scenario.

Lastly, consider the variation of the amplitude of the pattern, shown in figure 3.6

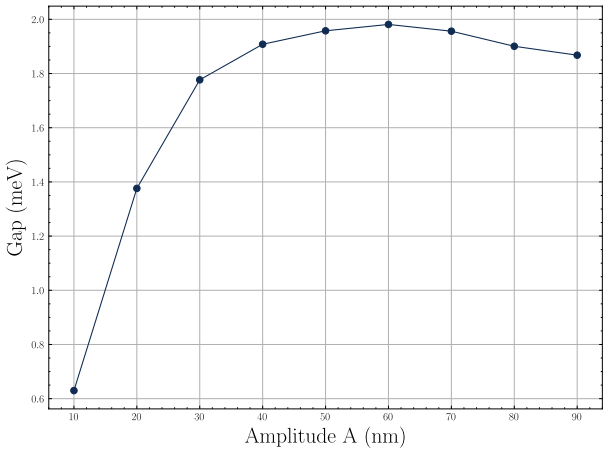

Figure 3.6: Gap vs A

At first enhancing the amplitude directly translates into an increase in the gap, as the sinusoidal pattern's contribution gains more importance. However, after about 60 to 70 nm, the gap begins to shrink: the reason can be attributed to the same argument applied for the two analysis above.

Having gathered the results above, it is now possible to address the question of the scientific investigation, on the ability of this kind of cavity to confine excitons. From the simulation computed, it is clear that the answer is no. Indeed, even if the parameters T and H are shrunk to get the gap above the 1 meV threshold, there is a fundamental problem with the structure. In order to confine excitons, a periodic cavity must have a Brillouin zone big enough to see a variation in the exciton dispersion of at least 1 meV, and some states resonant with the exciton ground state energy. This arbitrary threshold of 1 meV has been chosen considering the common experimental resolution of experimental measurements from literature. Assuming for simplicity an hydrogen model where the dispersion has a parabolic shape (see subsection 2.1.2) with known values for the parameters [7], it follows that WS_2 has the resonance at about 2 eV, and that a difference of 1 meV can be discriminated at a distance from the Γ point (in k space) corresponding to a period below 70 nm. However, as seen in the simulations, already with a period of 100 nm the band gap is at about 6 eV: making the period shorter will cause the gap to be even higher. An energy so high is a problem for two reasons: firstly, it will be harder for excitons to couple with a radiation too far in energy. Secondly, lamps used in experimental measurements have a finite spectrum, which defines a limited energy window where modes can be observed: if the modes' energy is too high, they cannot be experimentally seen.

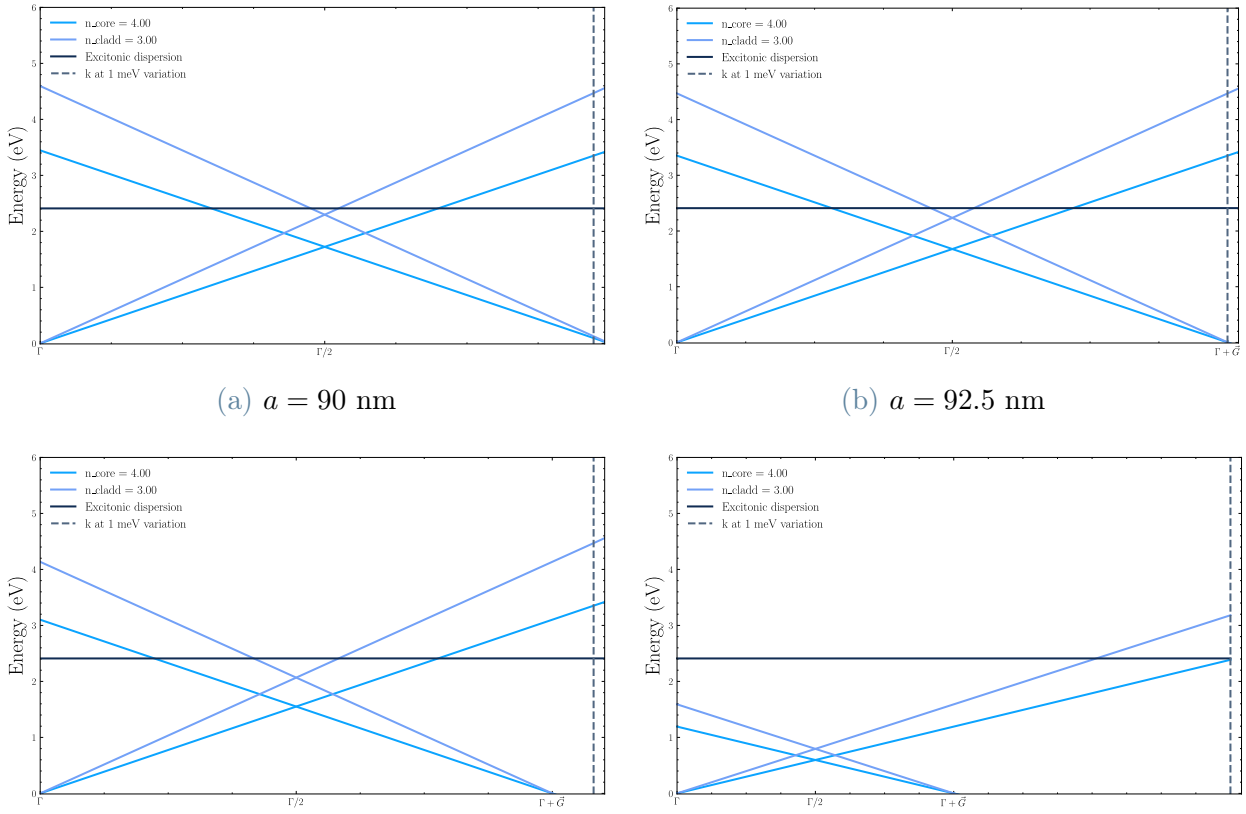

(a) $a = 90$ nm

(b) $a = 92.5$ nm

(c) $a = 100$ nm

(d) $a = 260$ nm

Figure 3.7: Light lines and exciton dispersions for different values of the period a; the dashed line shows where the excitonic dispersion is 1 meV different from its value at the Γ point

Moving away from the specific case simulated above, even considering a materials with a high refractive index, the same trade-off between having a big period to match the energies, and having a small period to match the k space requirement rules out the dielectric waveguide as a cavity to confine excitons. In the example shown in Fig. B.2, the matching energy condition is met at approximately 260 nm and upwards, while the k space requirement is fulfilled below 92.5 nm.

The only solution left is to consider a non-resonant regime. In that case, however, it is necessary to carefully consider the energies of the modes: indeed, hBN has a gap at around 6 eV [6], and any modes with a similar energy can either be absorbed, or inreract with hBN's excitons.

3.2. Plasmonic cavity

The second kind of Fourier cavity analyzed relies on the surface plasmon polaritons to confine the electromagnetic field within an even smaller volume than in the previous case. It is structured as a hBN slab with a sinusoidal pattern on the top surface, that lies on a silver substrate. In the following subsection firstly there will be a discussion on the numerical methods necessary for the simulations, and then the simulations results will be presented. Below a sketch of the model used.

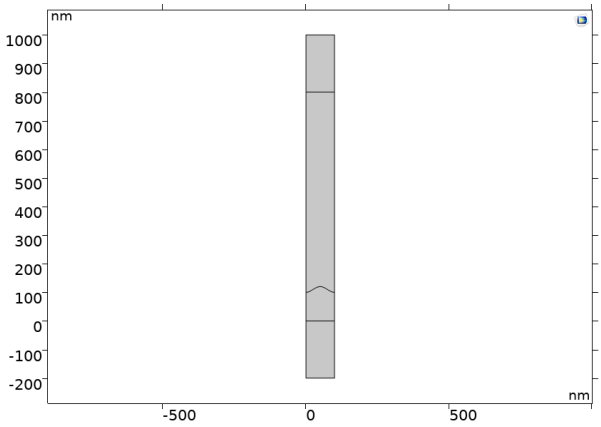

Figure 3.8: Sketch of the model

The parameters discussed in the following subsections are sketch in figure 3.9.

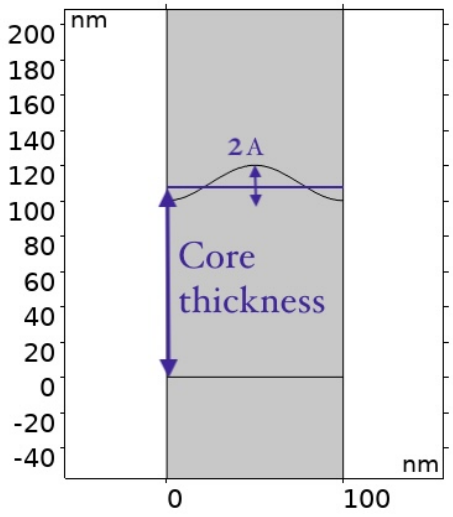

Figure 3.9: Detailed view on the parameters

3.2.1. Numerical treatment

The eigenfrequency study within the RF module in COMSOL® supports only non dispersive media. However for plasmons, the equation that needs to be solved is the following:

$$\varepsilon(\omega)\frac{\omega^2}{c^2}\vec{E} - \nabla^2\vec{E} = 0 \tag{3.1}$$

In short, the eigensolver takes a guess frequency ω_g, computes $\varepsilon(\omega_g)$, and then solves the problem for ω: if the medium is non dispersive or weakly dispersive, it does not matter if the guessed frequency coincides with the one found solving the equation, because $\varepsilon(\omega_g) \approx \varepsilon(\omega)\ \forall\ \omega$. On the other hand if the medium is dispersive, then $\varepsilon(\omega_g) \neq \varepsilon(\omega)$ in general, and therefore the solution found is not the correct eigenfrequency.

Even if there are no COMSOL®-native solution to this issue, it is still feasible to address dispersive system thanks to the theory behind the MAN (*Model Analysis of Nanoresonators*) package [39] [41] [23]. The fundamental assumption of this approach is that the medium permittivity is written analytically as a multi-poles Lorentz model:

$$\varepsilon(\omega) = \sum_n \varepsilon_0\varepsilon_\infty\left(1 - \frac{\omega_{pn}^2}{\omega^2 - \omega_{0n}^2 + i\gamma\omega}\right) \tag{3.2}$$

and constant permeability $\mu = \mu_0$. Because in the present work a single-pole permeability is accurate enough to describe the system, the assumption will be to have only one pole. The main idea now is to re-write eq. 3.1 with the help of two auxiliary field:

$$\vec{P}(\vec{r}) = -\varepsilon_0\varepsilon_\infty\frac{\omega_p^2}{\omega^2 - \omega_0^2 + i\gamma\omega}\vec{E}(\vec{r}) \qquad \vec{J}(\vec{r}) = -i\omega\vec{P}(\vec{r}) \tag{3.3}$$

Considering also the Maxwell equations:

$$i\varepsilon(\omega)^{-1}\nabla\times\vec{H}(\vec{r}) = \omega\vec{E}(\vec{r}) \qquad -i\mu^{-1}\nabla\times\vec{E}(\vec{r}) = \omega\vec{H}(\vec{r}) \tag{3.4}$$

it is possible to write a system of 4 equations. After the substitution of $\varepsilon(\omega)$ with its analytical expression, and a few algebraic steps, 3.1 becomes the linear equation:

$$\begin{bmatrix} 0 & -i\mu_0^{-1}\nabla\times & 0 & 0 \\ i(\varepsilon_0\varepsilon_\infty)^{-1}\nabla\times & 0 & 0 & -i(\varepsilon_0\varepsilon_\infty)^{-1} \\ 0 & 0 & 0 & i \\ 0 & i\omega_p^2\varepsilon_0\varepsilon_\infty & -i\omega_0^2 & -i\gamma \end{bmatrix} \begin{bmatrix} \vec{H}(\vec{r}) \\ \vec{E}(\vec{r}) \\ \vec{P}(\vec{r}) \\ \vec{J}(\vec{r}) \end{bmatrix} = \omega \begin{bmatrix} \vec{H}(\vec{r}) \\ \vec{E}(\vec{r}) \\ \vec{P}(\vec{r}) \\ \vec{J}(\vec{r}) \end{bmatrix} \tag{3.5}$$

Moreover, this expression can be put into quadratic form:

$$\begin{bmatrix} \nabla \times \mu^{-1} \nabla \times & 0 \\ \varepsilon_\infty \omega_p^2 & -\omega_0^2 \end{bmatrix} \begin{bmatrix} \vec{E}(\vec{r}) \\ \vec{P}(\vec{r}) \end{bmatrix} + \omega \begin{bmatrix} 0 & 0 \\ 0 & i\gamma \end{bmatrix} \begin{bmatrix} \vec{E}(\vec{r}) \\ \vec{P}(\vec{r}) \end{bmatrix} + \omega^2 \begin{bmatrix} -\varepsilon_\infty & -1 \\ 0 & 1 \end{bmatrix} \begin{bmatrix} \vec{E}(\vec{r}) \\ \vec{P}(\vec{r}) \end{bmatrix} = 0 \quad (3.6)$$

The above equations are enough to solve the issue and find the eigenmodes of the system. However, COMSOL®, solves the equation using the finite element method (FEM) [32]: in this framework, the differential equations above must be written in its *weak form*. The corresponding integro-differential equation are thus:

$$\int_V \nabla \times \vec{F}(\vec{r}) \cdot \mu^{-1} \nabla \times \vec{E}(\vec{r}) - \omega^2 \varepsilon_\infty \vec{F}(\vec{r}) \cdot \vec{E}(\vec{r}) - \omega^2 \vec{F}(\vec{r}) \cdot \vec{P}(\vec{r}) d^3\vec{r} = 0 \quad (3.7)$$

$$\int_V \varepsilon_\infty \omega_p^2 \vec{F}(\vec{r}) \cdot \vec{E}(\vec{r}) - \omega_0^2 \vec{F}(\vec{r}) \cdot \vec{P}(\vec{r}) + i\gamma\omega \vec{F}(\vec{r}) \cdot \vec{P}(\vec{r}) + \omega^2 \vec{F}(\vec{r}) \cdot \vec{P}(\vec{r}) d^3\vec{r} = 0 \quad (3.8)$$

In order to implement these equations in COMSOL® the same settings and boundary conditions considered in subsection 3.1.1 are applied, with only two exceptions. Firstly, it is relevant to mention that the weak form equation automatically implemented inside the RF module is the following:

$$\int_V \nabla \times \vec{F}(\vec{r}) \cdot \mu^{-1} \nabla \times \vec{E}(\vec{r}) - \omega^2 \varepsilon_\infty \vec{F}(\vec{r}) \cdot \vec{E}(\vec{r}) d^3\vec{r} = 0 \quad (3.9)$$

The only difference with eq. 3.7 is the term $-\omega^2 \vec{F}(\vec{r}) \cdot \vec{P}(\vec{r})$ which is added using the "weak form contribution" option inside the RF module.

Secondly, eq. 3.8 is implemented by adding to the simulation the Weak Form PDE module, which takes care of solving the equation. However a few details about it need to be explained: indeed, even though equation 3.8 is formally correct, it is not numerically stable. In order for the simulation to work properly, it is necessary to write it as:

$$\int_V \frac{1}{\lambda_N^2} \left(\varepsilon_\infty \vec{F}(\vec{r}) \cdot \vec{E}(\vec{r}) + \frac{-\omega_0^2 \vec{F}(\vec{r}) \cdot \vec{P}(\vec{r}) + i\gamma\omega \vec{F}(\vec{r}) \cdot \vec{P}(\vec{r}) + \omega^2 \vec{F}(\vec{r}) \cdot \vec{P}(\vec{r}) d^3\vec{r}}{\omega_p^2} \right) = 0, \quad (3.10)$$

where λ_N is a parameter which makes the equation numerically stable, and in the following simulations it is set equal to 100 nm. The choice of this value, suggested in the User Guide, is totally empirical: after trying different numbers in multiple simulation it is possible to conclude that the stability of the numerical methods is sound around $\lambda_N \approx 100$ nm.

3.2.2. Simulations

Because the aim of this work is to study the effect of a pattern which is directly on the surface of the cavity, and not on the substrate, for the case of surface plasmon polariton the pattern is considered to be on the dielectric part, and not on the metal one. Hence, the cavity taken into consideration is made from a patterned hBN core, with varying thickness, and a silver substrate. The choice of silver lies in the fact that its dispersion is well approximated (within a reasonable limit) by a single pole Lorentz-type function. An example of the results of the simulation is presented below here, while the rest are in the appendix B.

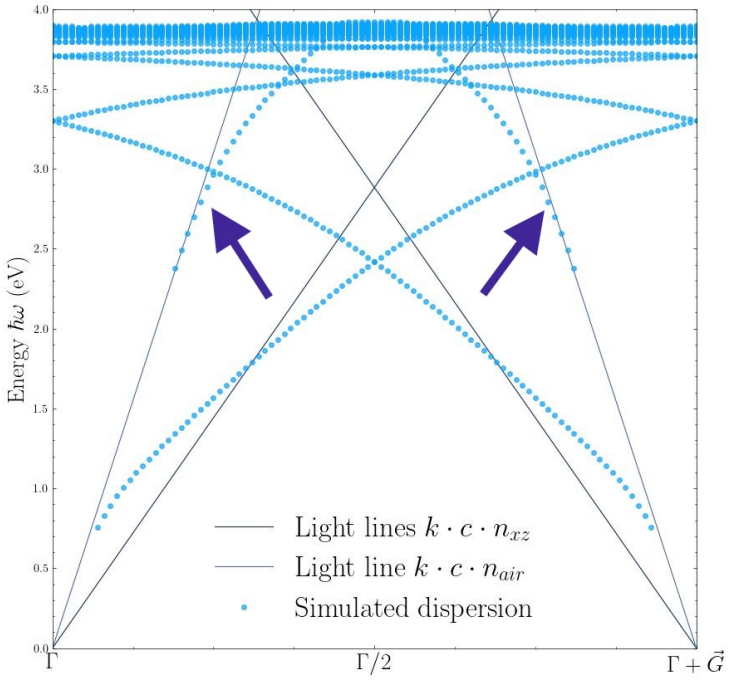

Figure 3.10: Simulation with a period of 100 nm, core thickness 100 nm and amplitude 10 nm

From this picture it is clear the effect of the periodic pattern on the dispersion of the modes. Considering that silver has $\omega_p = 8.99$ eV, the asymptote is correctly shown at $\omega_{SPP} = \omega_p/\sqrt{\varepsilon_{core} + 1} = 3.87$ eV. Notice also how, close to the asymptote, the dispersion is almost flat, and therefore the bending generates a high density of available states near the resonant energy.

By looking at the plot, which is post processed to remove box modes (see discussion in subsection 3.1.2), it is possible to see that, besides the surface plasmon polaritons, waveguides modes are present: they are indicated by the blue arrows.

Before analysing the dispersion further, consider the field profiles: as the theory in subsection 1.1.3 shows, only the TM modes can form plasmon polaritons. These modes can be chiefly described via the component of the electric field perpendicular to the surface, which in the case of these simulations is E_y, as shown in figure 3.11.

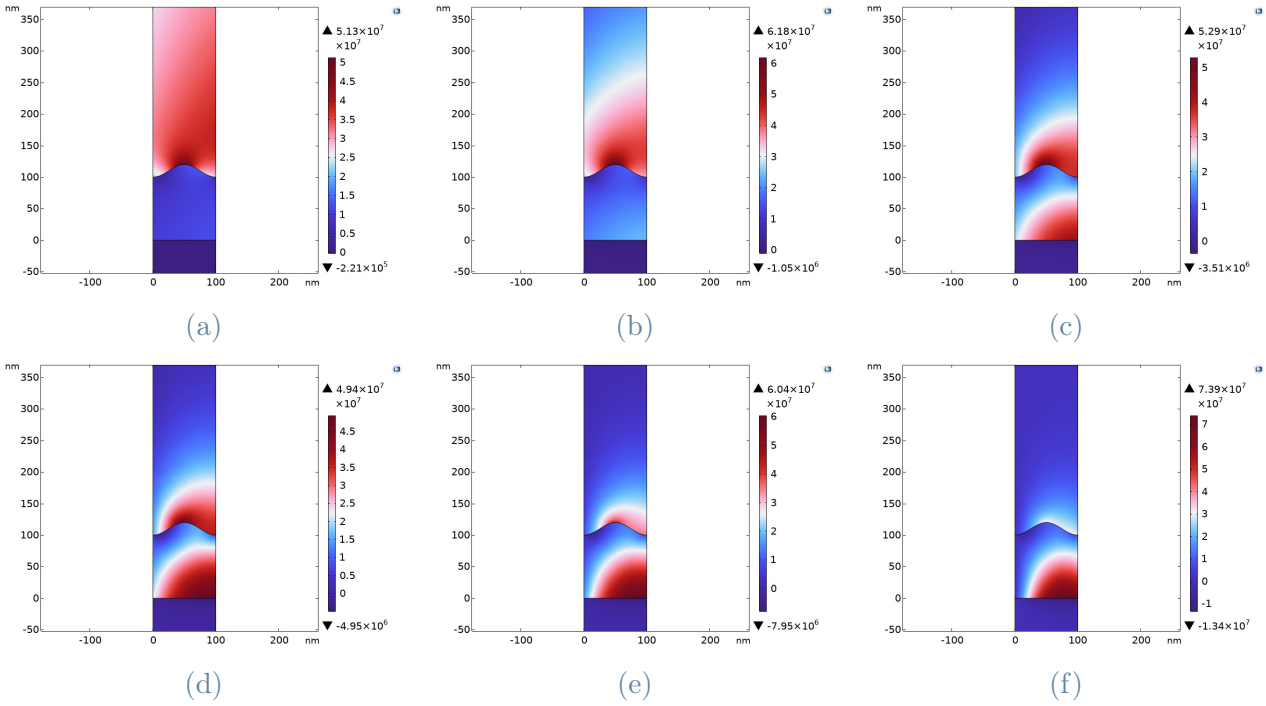

Figure 3.11: E_y field profiles for different k_x values; scale is V/m

Notice how, in the lowest branch, as the value of the k_x vector is increased, the surface plasmon polaritons moves from being on the tip of the pattern, to being close to the silver substrate. Notice also the field asymmetry present in the pictures: it is due to the fact that the modes possess a finite value of k_x.

On the other hand, higher energy modes do not show this behaviour: they stick to the silver surface:

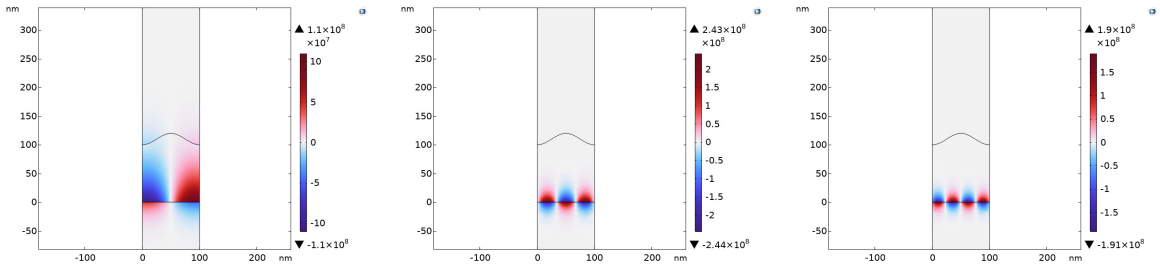

(a) (b) (c)

Figure 3.12: Examples of E_y profiles of higher order modes; scale is V/m

Moving on, it is relevant to notice that, for this kind of cavity, the period is not a parameter of interest. That is because, to avoid the k-space vs resonance trade-off, it is possible to look for material with an asymptote close to the target energy. Hence, the parameters of interest are only the thickness of the hBN core, and the amplitude of the pattern on top of it. Here's the results of the analysis of the gap (quantity of interest) at the Γ point:

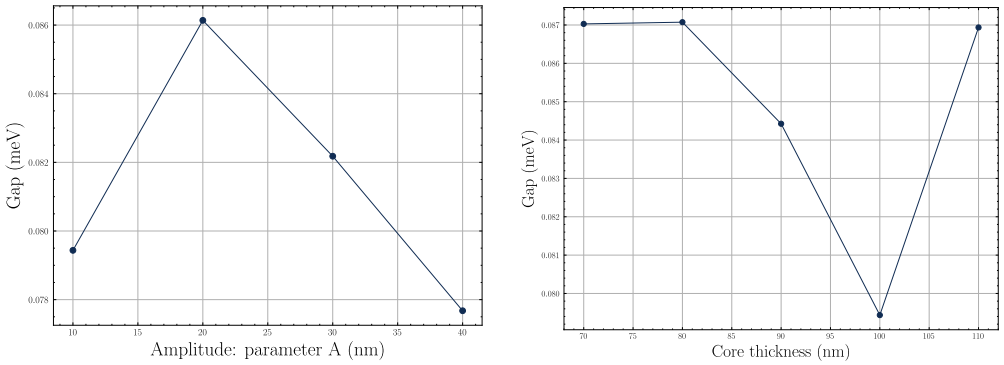

(a) Gap vs Amplitude (b) Gap vs Core Thickness

Figure 3.13: Study on the variation of the gap

The parameters have been chosen to be in a realistic range. Unfortunately the gap is well below the threshold of 1meV, and therefore any analysis of the curves is not useful, since such small fluctuations won't be experimentally distinguishable. Even though surface plasmon polaritons introduce great confinement in the field, they fail to generate a meaningful gap.

3.3. Hyperbolic dispersion cavity

The third kind of Fourier cavity aims to achieve even smaller confinement of the electromagnetic field thanks to the help of hyperbolic polaritons. To be precise, the cavity, made of hBN, can sustain hyperbolic phonon-polaritons in the IR frequency range (see subsection 2.2.2 for a detailed presentation). In the following subsection firstly there will be a discussion on the numerical methods necessary for the simulations, and then the simulations results will be presented.

3.3.1. Numerical treatment

The issue of dispersive media in COMSOL® is addressed with the same MAN approach employed in 3.2.1. The only difference is that now the permittivity, which remains frequency dependent, is not a scalar quantity, but a diagonal tensor:

$$\varepsilon(\omega) = \begin{bmatrix} \varepsilon_x(\omega) & 0 & 0 \\ 0 & \varepsilon_y(\omega) & 0 \\ 0 & 0 & \varepsilon_z(\omega) \end{bmatrix} \tag{3.11}$$

Further, because the system considered, namely hBN, has an in-plane isotropy, there will be used the further assumption $\varepsilon_x(\omega) = \varepsilon_z(\omega)$. Hence, the auxiliary fields are defined as:

$$\vec{P} = \begin{pmatrix} -\varepsilon_0 \varepsilon_{\infty x} \frac{\omega_{px}^2}{\omega^2 - \omega_{0x}^2 + i\gamma_x \omega} E_x \\ -\varepsilon_0 \varepsilon_{\infty y} \frac{\omega_{py}^2}{\omega^2 - \omega_{0y}^2 + i\gamma_y \omega} E_y \\ -\varepsilon_0 \varepsilon_{\infty x} \frac{\omega_{px}^2}{\omega^2 - \omega_{0x}^2 + i\gamma_x \omega} E_z \end{pmatrix} \qquad \vec{J} = -i\omega \vec{P} \tag{3.12}$$

By also defining the tensorial quantities

$$\overline{\overline{\varepsilon}}_\infty = \begin{bmatrix} \varepsilon_{\infty x} & 0 & 0 \\ 0 & \varepsilon_{\infty y} & 0 \\ 0 & 0 & \varepsilon_{\infty x} \end{bmatrix} \quad \overline{\overline{\Omega}}_p = \begin{bmatrix} \omega_{px}^2 & 0 & 0 \\ 0 & \omega_{py}^2 & 0 \\ 0 & 0 & \omega_{px}^2 \end{bmatrix} \quad \overline{\overline{\Omega}}_0 = \begin{bmatrix} \omega_{0x}^2 & 0 & 0 \\ 0 & \omega_{0y}^2 & 0 \\ 0 & 0 & \omega_{0x}^2 \end{bmatrix} \quad \overline{\overline{\Gamma}} = \begin{bmatrix} \gamma_x & 0 & 0 \\ 0 & \gamma_y & 0 \\ 0 & 0 & \gamma_x \end{bmatrix}$$

the linearized equation becomes:

$$\begin{bmatrix} 0 & -i\mu_0^{-1}\nabla\times & 0 & 0 \\ -i\varepsilon_0^{-1}\bar{\bar{\varepsilon}}_\infty^{-1}\nabla\times & 0 & 0 & -i\varepsilon_0^{-1}\bar{\bar{\varepsilon}}_\infty^{-1} \\ 0 & 0 & 0 & i \\ 0 & i\varepsilon_0\bar{\bar{\varepsilon}}_\infty\bar{\bar{\Omega}}_p & -i\bar{\bar{\Omega}}_0 & -i\bar{\bar{\Gamma}} \end{bmatrix} \begin{pmatrix} \vec{H} \\ \vec{E} \\ \vec{P} \\ \vec{J} \end{pmatrix} = \omega \begin{pmatrix} \vec{H} \\ \vec{E} \\ \vec{P} \\ \vec{J} \end{pmatrix} \tag{3.13}$$

Notice that it is formally equivalent to eq. 3.5. Similarly, the quadratic form is also formally equivalent to eq. 3.6:

$$\begin{bmatrix} \nabla\times\mu_0^{-1}\nabla\times & 0 \\ \bar{\bar{\varepsilon}}_\infty\bar{\bar{\Omega}}_p & -\bar{\bar{\Omega}}_0 \end{bmatrix} \begin{bmatrix} \vec{E} \\ \vec{P} \end{bmatrix} + \omega \begin{bmatrix} 0 & 0 \\ 0 & i\bar{\bar{\Gamma}} \end{bmatrix} \begin{bmatrix} \vec{E} \\ \vec{P} \end{bmatrix} + \omega^2 \begin{bmatrix} -\bar{\bar{\varepsilon}}_\infty & -1 \\ 0 & 1 \end{bmatrix} \begin{bmatrix} \vec{E} \\ \vec{P} \end{bmatrix} = 0 \tag{3.14}$$

And lastly, the weak form:

$$\int_V \nabla\times\vec{F}(\vec{r})\cdot\mu^{-1}\nabla\times\vec{E}(\vec{r}) - \omega^2\bar{\bar{\varepsilon}}_\infty\vec{F}(\vec{r})\cdot\vec{E}(\vec{r}) - \omega^2\vec{F}(\vec{r})\cdot\vec{P}(\vec{r})d^3\vec{r} = 0 \tag{3.15}$$

$$\int_V \bar{\bar{\varepsilon}}_\infty\bar{\bar{\Omega}}_p\vec{F}(\vec{r})\cdot\vec{E}(\vec{r}) - \bar{\bar{\Omega}}_0\vec{F}(\vec{r})\cdot\vec{P}(\vec{r}) + i\bar{\bar{\Gamma}}\omega\vec{F}(\vec{r})\cdot\vec{P}(\vec{r}) + \omega^2\vec{F}(\vec{r})\cdot\vec{P}(\vec{r})d^3\vec{r} = 0 \tag{3.16}$$

In order to implement these equations in COMSOL® the same settings and boundary conditions considered in subsection 3.2.1 are applied, taking into consideration that the scalar quantities ε_∞, ω_p, ω_0, and γ are now tensors.

It is relevant to stress that this generalization is not discussed in the main MAN papers, rather, together with its implementation, it can be considered as an original contribution.

3.3.2. Simulations

The implementation of the MAN framework for the hyperbolic cavity case has been significantly more challenging that the previous one. First of, consider the weak form equations 3.16. A straightforward implementation would be:

$$\int_V \varepsilon_{\infty x}\omega_{px}^2F_xE_x + \varepsilon_{\infty y}\omega_{py}^2F_yE_y + (-\omega_{0x}^2 + i\gamma_x\omega + \omega^2)F_xP_x + (-\omega_{0y}^2 + i\gamma_y\omega + \omega^2)F_yP_yd^3r = 0 \tag{3.17}$$

But that would not be numerically stable, as explained in the previous section, where the numerical stabilization was:

$$\int_V \frac{1}{\lambda_N^2}\left(\varepsilon_\infty \vec{F}(\vec{r})\cdot\vec{E}(\vec{r}) + \frac{-\omega_0^2\vec{F}(\vec{r})\cdot\vec{P}(\vec{r}) + i\gamma\omega\vec{F}(\vec{r})\cdot\vec{P}(\vec{r}) + \omega^2\vec{F}(\vec{r})\cdot\vec{P}(\vec{r})d^3\vec{r}}{\omega_p^2}\right) = 0, \tag{3.18}$$

However, compare equations 3.17 and 3.18: it is not possible to re-write the former exactly in terms of the ladder, because there are two ω_p^2 terms with different values. A first approach would be to simply take the largest plasma frequency and use it to normalise. Hence equation 3.17 would become:

$$\int_V \frac{1}{\lambda_N^2}\left(\varepsilon_{\infty x}F_xE_x + \varepsilon_{\infty y}\frac{\omega_{py}^2}{\omega_{px}^2}F_yE_y + \frac{(-\omega_{0x}^2 + i\gamma_x\omega + \omega^2)}{\omega_{px}^2}F_xP_x + \frac{(-\omega_{0y}^2 + i\gamma_y\omega + \omega^2)}{\omega_{px}^2}F_yP_y\right)d^3r = 0 \tag{3.19}$$

In figure 3.14 the results of such choice:

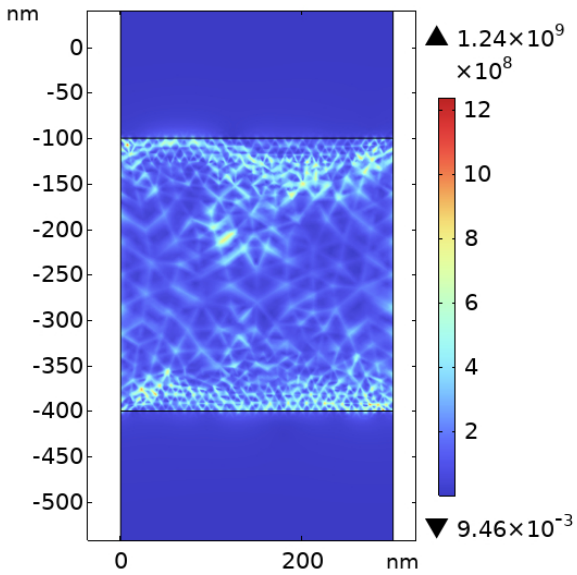

Figure 3.14: Norm of the electric field for a fixed frequency and fixed k_x vector

These kind of solutions are referred to as "mesh modes", because their profile closely follows the underlying mesh nodes. Additionally, these modes are all found within 1 THz from the guess frequency inserted in the eigensolver. They do not hold any physical meaning, and their presence indicates that something has gone wrong.

In order to avoid this problem, one could try to change the value of λ_N or divide by ω_{py}^2 instead, but the result is the same: only mesh modes. This behaviour of the solver implies that a new approach needs to be considered. For instance the two components, x and y, could be separated into two different PDEs: in that way, each term is divided by the corresponding plasma frequency, by a different λ_N, and the numerical stability could be achieved. There is, however, a fundamental problem that lies within the FEM implementation: the two equations, for the x and the y components, would be one-dimensional. As a consequence, it would be impossible to use the "curl" shape function, which requires a test function of two components, for F: because the solver for the main Helmholtz equation employs precisely a curl shape function, not using the same one for the two additional PDEs would result in great numerical instability.

A way to get over this impasse is to construct two fictitious poles in the following manner:

$$\vec{P} = \varepsilon_0 \left(\chi_1 + \chi_2\right) \vec{E}, \tag{3.20}$$

The susceptibilities are defined as:

$$\chi_1 = \begin{bmatrix} \varepsilon_x(\omega) & 0 \\ 0 & \varepsilon_{xY}(\omega) \end{bmatrix} \quad \chi_2 = \begin{bmatrix} \varepsilon_{yX}(\omega) & 0 \\ 0 & \varepsilon_y(\omega) \end{bmatrix}$$

where, and this is the fundamental point, the peak of $\varepsilon_x(\omega)$ ($\varepsilon_y(\omega)$) is in the same position of the peak of $\varepsilon_{xY}(\omega)$ ($\varepsilon_{yX}(\omega)$), but with $\omega_{pxY} \approx 0$ ($\omega_{pyX} \approx 0$). In this manner, the overall physical system is not modified, while the numerical stability is, hopefully, much better. Indeed, in this framework it is possible to consider the two χ as two separate poles, and write the equations:

$$\int_V \frac{1}{\lambda_{Nx}^2} \left(\varepsilon_{\infty x} F_{x1} E_x + \varepsilon_{\infty x} \frac{\omega_{pxY}^2}{\omega_{px}^2} F_{y1} E_y + \frac{(-\omega_{0x}^2 + i\gamma_x \omega + \omega^2)}{\omega_{px}^2} (F_{x1} P_{x1} + F_{y1} P_{y1}) \right) d^3 r = 0 \tag{3.21}$$

$$\int_V \frac{1}{\lambda_{Ny}^2} \left(\varepsilon_{\infty y} \frac{\omega_{pyX}^2}{\omega_{py}^2} F_{x2} E_x + \varepsilon_{\infty y} F_{y2} E_y + \frac{(-\omega_{0y}^2 + i\gamma_y \omega + \omega^2)}{\omega_{py}^2} (F_{x2} P_{x2} + F_{y2} P_{y2}) \right) d^3 r = 0 \tag{3.22}$$

Here, the only components with physical meaning are P_{1x} and P_{2y}, while P_{1y} and P_{2x} are only a mathematical artefact. As shown in figure 3.15, this approach has more promising results, but it does not yet give the correct results [9].

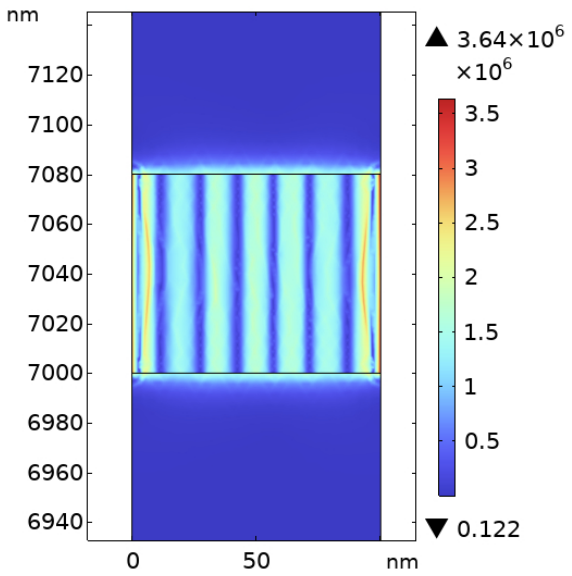

Figure 3.15: Norm of the electric field for a fixed frequency and fixed k_x vector

4 | Chapter four: Experimental Work

In the previous sections, numerical simulations and theoretical predictions have been made. In this chapter, the aim is to study if the folding of the bands is experimentally visible. In order to address this question, a prototype of a cavity is fabricated. In the following, the details of its fabrication and the experimental reflection measurements on it will be discussed. The first section is designated to the fabrication technique, while the second one focuses on the experimental measurements.

4.1. Fabrication of the sample

The preparation of the prototype requires two main steps: creating hBN structures on a substrate, and placing a sinusoidal pattern on top of them. These procedures will be thoroughly described in the following subsections.

4.1.1. Exfoliation of hBN

The fabrication of the cavity begins with the substrate where it will be placed. The substrate must hold two crucial characteristics: firstly it needs to be transparent or semi-transparent in order to improve the optical contrast (vital for the optical measurements); secondly, it needs to be conductive in order for the nanolithography process to work properly. Two substrates holding the aforementioned properties have been selected: ITO glass and CrAu glass.

ITO, which stands for *indium tin oxide*, is a compound famously known for being transparent and conducting at the same time, and for being easily deposited as a thin film. Indeed, ITO glass is a 15 mm by 20 mm piece of Polished soda lime float glass with a fully oxidized layer of ITO on top. This layer has a quoted resistance of 20 Ω, a thickness of 100 nm, and a roughness of 1.8 nm (measured by the manufacturer via AFM). All the

properties are a perfect fit for the needs of the presented study, except for the value of the roughness, which is not exactly ideal: as a consequence, it will be difficult to exfoliate on top of such surface, as hBN favours sticking to more flat substrates.

The second substrate is also a piece of glass, about half the size of the previous one, on top of which it has been deposited, in the DTU 2DPHYS department laboratories, a 2 nm layer of chromium and a 8 nm layer of gold. This structure is not quite as transparent as the ITO substrate, but it is approximately as conductive. Most importantly, its greatest advantage over the ITO glass is that its metallic nature makes it easier for hBN to stick on top.

After the substrate selection it is necessary to place hBN on top of it. For that to work the substrates need to be cleaned first. Initially, the cleaning happens in a fume hood, and it consists of a few steps:

1. acetone bath at 40^{o}C for 30 minutes, to remove possible traces of dust or other particles;
2. water bath at room temperature for 2 minutes, to remove completely any acetone droplets and remaining impurities;
3. IPA (isopropyl alcohol) bath at room temperaturefor 2 minutes, to remove any water droplets and still remaining impurities.

Then, in order to remove IPA as well, the substrate is dried with a nitrogen gun, taken out of the fume hood, and sent to a plasma chamber, where it undergoes an oxygen plasma cleaning procedure for 10 minutes. Only upon completion of this last step, the substrate is ready for use. Indeed in the process of fabrication of nanostructure it is extremely important to work with a clean substrate, because any unwanted external particles can greatly affect the working of the system.

A hBN crystal, as seen in chapter 2, is made up of many layers kept close to each other via Van der Waals interactions. In order to have flakes of hBN on the substrate, it is necessary to take some of the layers from the crystal by employing a method called *exfoliation*. This procedure is carried out in the following way: some tape is stuck to the crystal and slowly removed, so that a portion of the layers is now on the tape. Then, another piece of tape is stuck to the first one, and slowly removed. This sticking and un-sticking of pieces of tape continues until a sufficiently thin deposit of hBN remains on

one piece of tape. After that, this last piece is stuck to the substrate. In order to make it easier for hBN to stick to the substrate, the whole structure with tape on top is placed on a hot plate at 90^{o}C for a few minutes, and then the tape is slowly removed. The final result is a substrate with hBN flakes.

In order to have the sinusoidal pattern, it is necessary to carve it via nanolithography. Because it is not possible to perform it directly on the hBN flake, it is useful to cover the whole sample with a polymeric resist made of a solution of PPA (polyphthalamide, also known as high performance polyamide): indeed the working of the nanolithography process, discussed in the next subsection, is based on the evaporation of this material. A drop of this substance is placed on top of the sample, which is then placed in a spin-coater, where, by exploiting the centrifugal motion, the solution is spread all over the sample. After that the sample is baked on a hot plate for a few minutes, so that the PPA solution on top can more quickly relax in a stable structure.

4.1.2. Nanolithography and characterization

Among the many available technique for nanolithography, the one chosen in this study is the *thermal scanning probe lithography* [31], or tSPL in short, and it is carried out with a machine called *nanofrazor*. The main reason for this choice is the micro- to nanometer scale precision of this instrument: because the optical measurement are carried out using visible light, it is necessary to have pattern which are not too far from the light's wavelength. There exist also other very accurate technique, as electron beam lithography for example, but to work they require stricter conditions.

Its working principle is the use of a high temperature AFM tip to sublimate a nanometer-sized portion of the underlying material, thus creating a pattern.

The tip is voltage controlled, meaning that it will dig deeper into the sample as the voltage is increased: the voltage applied is calculated on the basis of a capacitative measurement between the tip and the sample. As a consequence, the sample must be somehow conductive, otherwise the capacitance computation will fail, and the tip will not be able to know its distance from the sample. Hence, since hBN is not a conductive material, the choice of a conductive substrate is imperative.

The images above show how the work on the nanofrazor looks under an optical microscope. As it can be seen, the second picture shows some smaller patterns: the reason is that the nanofrazor is very sensitive to even the smallest environmental changes, and thus

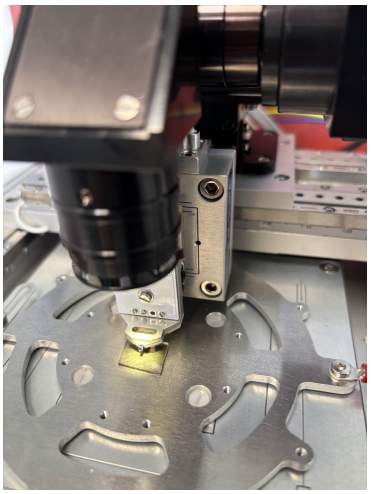

Figure 4.1: Picture of the nanofrazor: notice the tip, which is almost in contact with the sample, and the microscope, which allows the user to see where the pattern is being carved

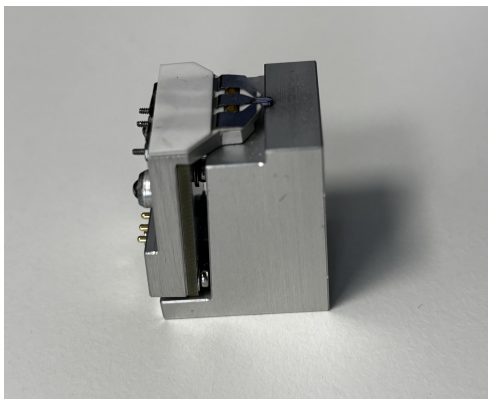

(a) Side view

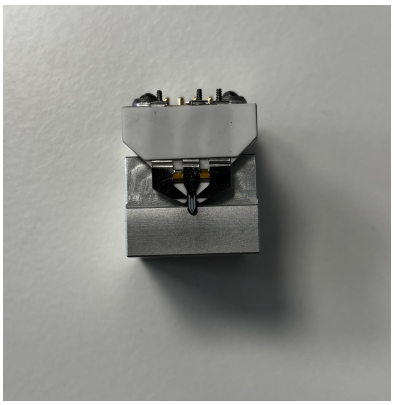

(b) Top view

Figure 4.2: Picture of the AFM tip on a stage

sometimes it seems to now work properly. However, since the pattern is hardly visible, it is convenient to use the nanofrazor in "reading" mode, i.e. as an AFM reader. The results are in figure 4.4:

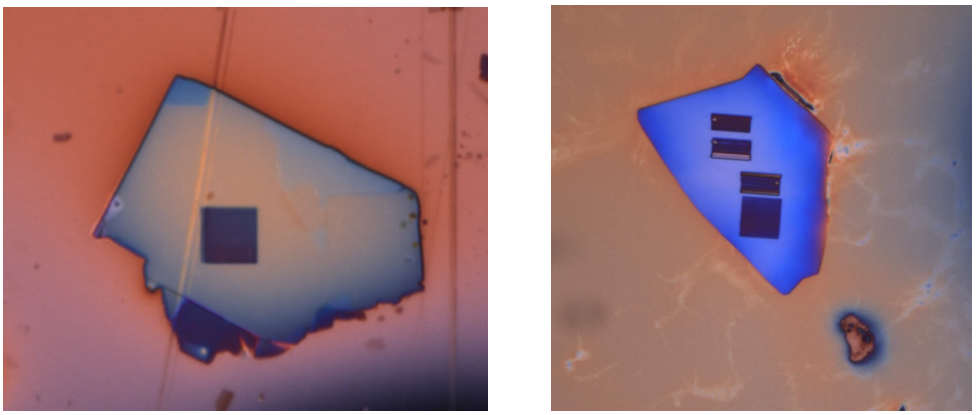

(a) CrAu sample (b) ITO sample

Figure 4.3: Pattern on PPA sitting on hBN flakes on different substrates

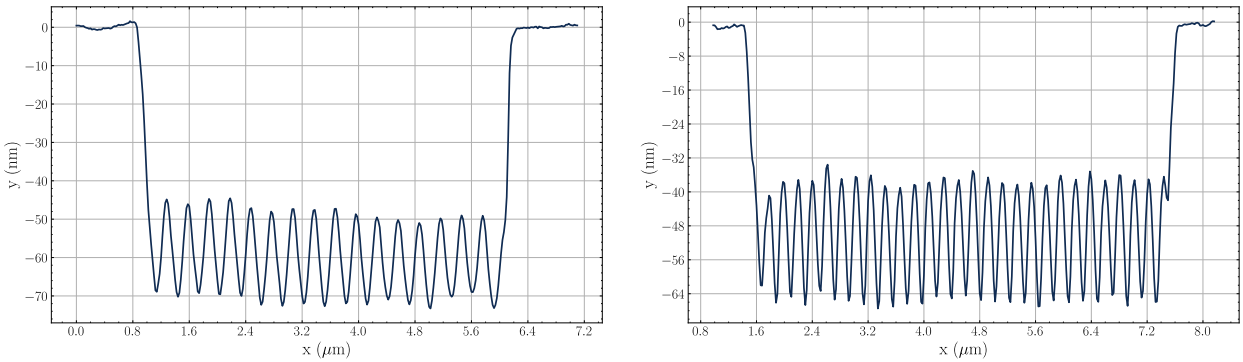

(a) CrAu , period = 300 nm (b) ITO sample, period = 200 nm

Figure 4.4: AFM-like scanning along a line perpendicular to the pattern

Notice the presence of an approximately 60 nm dip, besides the periodic pattern: what happened is that, even though the PPA coating is relatively thin, in order to have a pattern-hBN distance of about 10-20 nm, it was necessary to carve down the resist, and then make the pattern.

It can be clearly seen that the pattern has a distinct periodicity, even tough some noise-like features are present. The discrepancies between the desired shape and the actual result can be attributed to the extremely sensitive nature of the tip: as the pattern is imprinted, most of the resist is sublimated as soon as it is touched by the hot tip, but tiny pieces may stick temporarly to the tip. Hence the tip's shape gets a little modified, and its overall electric resistance as weel. As a consequence it strays from the desired shape. Even if these variations look small, they are still in the tens of nanometer scale.

The sample shown in this section have been picked among many similar ones. The main challenge of working with this type of ITO substrate is its significant surface roughness, which is a double problem: layered materials like hBN tend to avoid sticking to it, while dust particles are easily trapped. Hence not only the cleaning process described in the previous subsection needs to be repeated more than one time, but also the exfoliating process on such surface requires extreme care, many trials, and at the end the available hBN flakes are very limited in number. This issue is not present for the CrAu sample, on which, many more flakes are easily found. On the other hand, if ITO samples can be easily acquired commercially, these CrAu samples need a quite laborious in-house fabrication, which requires significantly more time.

4.2. Optical measurements

Once the sample has been fabricated, it is now possible to verify experimentally what was found out in the simulations. The next subsections describe the experimental set up, how it works, and present the analysis of the data from the samples.

4.2.1. Description of the optical setup

In order to experimentally measure the dispersion relation of the guided modes inside the cavity, it is necessary to analyse light at different wavelength (related to energy, the y axis), and at different angles (related to k, the x axis). The first requirement is satisfied by employing a *spectrometer*, that is a light detector that, thanks to internal mirrors, diffraction gratings and multiple detectors, is able to take a *spectral image*: i.e. to measure how many photons have a certain frequency, for each frequency of a limited spectrum.

The second requirement can be satisfied in many ways, for instance moving the light source or moving the detectors to cover a certain range of angles. The technique used in this set up, however, is different. A fixed source shines white light onto the sample; then, the reflected light is channeled to a lens, and then to the detector, the spectrometer. The fundamental element is the lens: if the light were to go directly to the detector, it would just see the sample, and no information about angles would be transmitted. Instead, in the set up considered, the light goes through a lens that performs a Fourier transformation of the sample's image: this new image lies in k space, and therefore carries information about the angles. At this point, one last step needs to be considered.

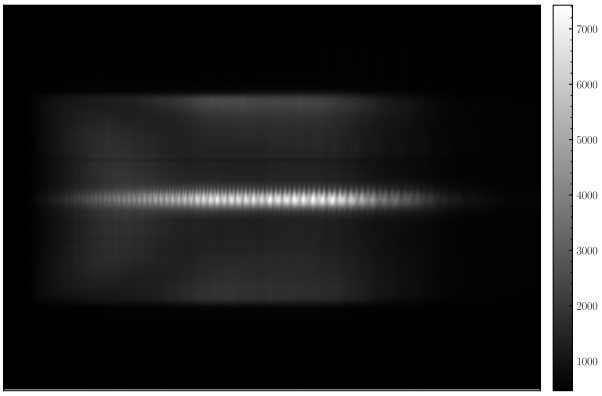

Figure 4.5: Example of an output of the spectrometer: the x axis represents the wavelength while the y axis the position

The output of the spectrometer is a plot where on the x axis lie the wavelength analysed,

on the y axis the position (arbitrary units, explanation comes later), and the colour of each pixel represents the intensity (grayscale). The problem is that the position displayed is a fictitious one: the intensity at each point is the result of the spectrometer taking, at a fixed wavelength, the mean intensity of a horizontal row of pixels in the image. As a consequence the information on angles is lost. To solve this issue, a slit is placed before the spectrometer: hence, the image that arrives at the detector is not the full (k_x, k_y) Fourier-transformed image, rather it is only a thin vertical line. Hence, each point in the spectrometer output is not the mean over multiple points, but only the measured intensity at a single point.

At last, one more element of the setup needs to be presented: a small circular aperture. Indeed, even if the light coming from the lamp goes through a microscope with a high objective before hitting the sample, it illuminates a rather large portion of the sample, including areas where the pattern is not present. These areas will contribute to the overall noise, which will screen the signal coming from the patterned area. To avoid this scenario, the aperture is placed between the sample and the lens, so that the image Fourier-transformed will include only the patterned zone.

4.2.2. Results and comments

Before considering the measurements on the samples analysed in subsection 4.1.2,it is necessary to perform numerical simulations that will provide a guide to examine the experimental results. The COMSOL® implementation is very similar to the previous case, with the only exception that the parameters for all the materials are taken from literature [22] [20] [33] [21]. The results are presented in figure 4.6.

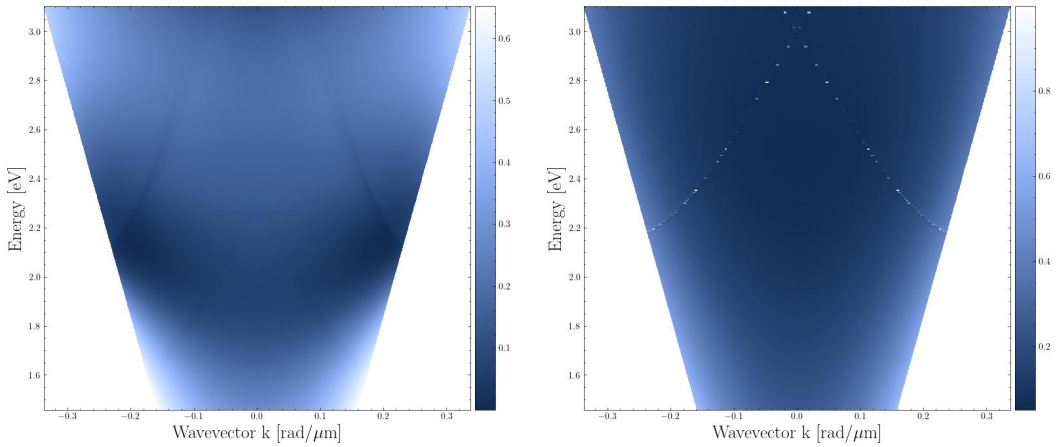

(a) CrAu (b) ITO

Figure 4.6: Simulations of the dispersion relation for the samples, colour bar for intensity

From the picture, it is clear that the expectation is to see a much stronger signal for the ITO sample, but the CrAu sample has the potential of showing double the lines: indeed, with a bit of focus, it is possible to recognize two more lines under the two more visible ones. A remark before presenting the experimental result: from the numerical simulations it appears that the bands' folding is hardly visible when using a PPA coat on top of hBN. However, before drawing the final conclusion, it is necessary to consider the experimental result. In this regard, note that the intensity read by the detector needs to be normalized. Firstly it is necessary to eliminate the dark counts by subtracting the intensity measured when the lamp is switched off. Then, in order to eliminate possible contributions coming from the environment around the sample, it is necessary to perform a normalization by dividing for the intensity measured in a portion of the flake without the pattern. Hence, the final intensity is calculated following the equation:

$$I = \frac{I_{sample} - I_{dark}}{I_{reference} - I_{dark}} \tag{4.1}$$

Consider the Cr-Au sample. The experimental dispersion relation acquired is shown in figure 4.7:

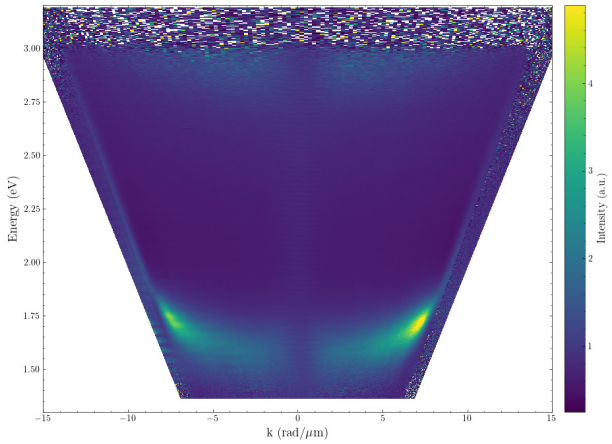

Figure 4.7: Experimental dispersion relation for CrAu sample, intensity normalized at 1^{st} and 99^{th} percentiles

As it can be seen, unfortunately it is not possible to see the dispersion lines of the modes, even after enhancing the data. A similar dispersion results from the measurements on the ITO sample, shown in figure 4.8:

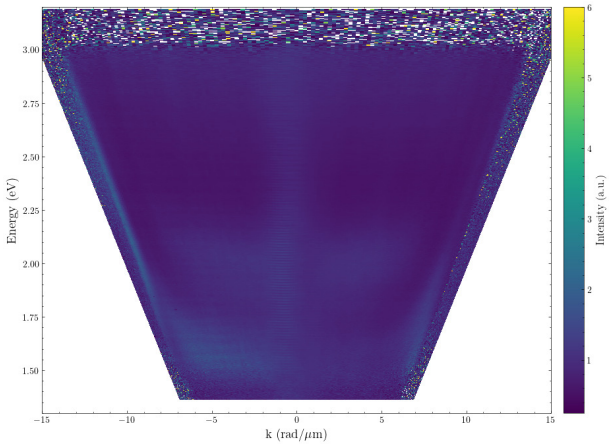

Figure 4.8: Experimental dispersion relation for ITO sample, intensity normalized at 1^{st} and 99^{th} percentiles

Also in this case there is no visible trace of the characteristic lines of the modes.

These unsatisfactory results are caused by many factors. Firstly, as highlighted in subsection 4.1.2, the shape of the pattern presents many irregularities. Then, the reduced size of the overall pattern required the circular slit to be almost completely closed. As a consequence there could be diffraction effects that disrupt the signal. Moreover, the small values of the intensity of the image suggest that the measurements from the sample and from the reference are very similar. That means that the pattern on PPA does not contributes significantly to the signal.

At last, it can be concluded that patterning PPA instead of hBN does not lead to a visible bending: the signal, if present at all, is surely very hard to acquire.

5 | Conclusions and future developments

In this work, the behaviour of the electromagnetic field inside Fourier optical cavities has been discussed. The role of a discrete periodicty has been studied. A few examples have also been presented and analysed: a dielectric waveguide, where an experimental evaluation has been attempted; a plasmonic cavity, where surface plasmon polaritons are exploited to confine the field; and an hyperbolic cavity, where the peculiar phonon response generates a change in sign between diagonal terms of the dielectric tensor, thus furthering confining the modes. In this regard, ab initio calculation has been employed to compute the optical response of both the cavity and the material that would host the excitons. Therefore, the outcome of this study is the calculation of the eigenmodes of the electromagnetic field inside the listed cavities, and the optical response of the materials.

The next step to make towards the goal of simulating exciton-photon coupling, thus combining the two main results of this work, is to quantise the calculated field. The idea would be to extract the electromagnetic field from the numerical simulation, decompose it in its Fourier components and, from there, compute the Hamiltonian and solve the Schroedinger equation with it. In this regard, a specialised code that deals with light-matter interaction at the second quantisation level is needed [37]. With regards to the hyperbolic cavity, there are multiple possibilities ahead. Regarding the MAN approach, a more thorough analysis of the causes of numerical instabilities needs to be performed. Alternatively, a new mathematical framework could be considered: for instance, even if the computations are more costly, the Helmhltz equation can be solved iterativaly in a self-consisten way. From an experimental point of view, the next step would be to plasma etch the pattern in the PPA, so that it gets transferred to the hBN itself. This would certainly enhance the optical response. Other nanolitographic technique can be tested as well, from electron beam litography to chemical etching. In a broader view, it would also be necessary to experimentally measure the response from other kinds of cavities, for example the plasmonic one, or the hyperbolic one.

Bibliography

[1] COMSOL Multiphysics® v. 6.3. COMSOL AB, Stockholm, Sweden.

[2] G. M. Andolina, M. Ceccanti, B. Turini, R. Riolo, M. Polini, M. Schiró, and F. H. L. Koppens. Quantum Electrodynamics of graphene Landau levels in a deep-subwavelength hyperbolic phonon polariton cavity, Mar. 2025. URL `http://arxiv.org/abs/2501.04133`. arXiv:2501.04133 [cond-mat].

[3] S. R. Bahn and K. W. Jacobsen. An object-oriented scripting interface to a legacy electronic structure code. *Comput. Sci. Eng.*, 4(3):56–66, MAY-JUN 2002. ISSN 1521-9615. doi: 10.1109/5992.998641.

[4] D. N. Basov, A. Asenjo-Garcia, P. J. Schuck, X. Zhu, and A. Rubio. Polariton panorama. *Nanophotonics*, 10(1):549–577, Nov. 2020. ISSN 2192-8614, 2192-8606. doi: 10.1515/nanoph-2020-0449. URL `https://www.degruyter.com/document/doi/10.1515/nanoph-2020-0449/html`. Publisher: Walter de Gruyter GmbH.

[5] S. Brem, C. Linderälv, P. Erhart, and E. Malic. Tunable phases of moiré excitons in van der waals heterostructures. *Nano Letters*, 20(12):8534–8540, 2020. doi: 10.1021/acs.nanolett.0c03019. URL `https://doi.org/10.1021/acs.nanolett.0c03019`. PMID: 32970445.

[6] G. Cassabois, P. Valvin, and B. Gil. Hexagonal boron nitride is an indirect bandgap semiconductor. *Nature Photonics*, 10(4):262–266, Apr. 2016. ISSN 1749-4885, 1749-4893. doi: 10.1038/nphoton.2015.277. URL `https://www.nature.com/articles/nphoton.2015.277`.

[7] A. Chernikov, T. C. Berkelbach, H. M. Hill, A. Rigosi, Y. Li, B. Aslan, D. R. Reichman, M. S. Hybertsen, and T. F. Heinz. Exciton binding energy and nonhydrogenic rydberg series in monolayer ws 2. *Physical review letters*, 113(7):076802, 2014.

[8] S. Dai, Z. Fei, Q. Ma, A. S. Rodin, M. Wagner, A. S. McLeod, M. K. Liu, W. Gannett, W. Regan, K. Watanabe, T. Taniguchi, M. Thiemens, G. Dominguez, A. H. C. Neto, A. Zettl, F. Keilmann, P. Jarillo-Herrero, M. M. Fogler, and D. N. Basov.

Tunable Phonon Polaritons in Atomically Thin van der Waals Crystals of Boron Nitride. *Science*, 343(6175):1125–1129, Mar. 2014. ISSN 0036-8075, 1095-9203. doi: 10.1126/science.1246833. URL https://www.science.org/doi/10.1126/science.1246833.

[9] S. Dai, J. Quan, G. Hu, C.-W. Qiu, T. H. Tao, X. Li, and A. Alù. Hyperbolic Phonon Polaritons in Suspended Hexagonal Boron Nitride. *Nano Letters*, 19(2):1009–1014, Feb. 2019. ISSN 1530-6984, 1530-6992. doi: 10.1021/acs.nanolett.8b04242. URL https://pubs.acs.org/doi/10.1021/acs.nanolett.8b04242.

[10] P. e. a. Giannozzi. QUANTUM ESPRESSO: a modular and open-source software project for quantum simulations of materials. *J. Phys.: Condens. Matter*, 21(39):395502, Sept. 2009. ISSN 0953-8984, 1361-648X. doi: 10.1088/0953-8984/21/39/395502. URL https://iopscience.iop.org/article/10.1088/0953-8984/21/39/395502.

[11] P. e. a. Giannozzi. Advanced capabilities for materials modelling with Quantum ESPRESSO. *J. Phys.: Condens. Matter*, 29(46):465901, Nov. 2017. ISSN 0953-8984, 1361-648X. doi: 10.1088/1361-648X/aa8f79. URL https://iopscience.iop.org/article/10.1088/1361-648X/aa8f79.

[12] P. e. a. Giannozzi. Quantum espresso toward the exascale. *The Journal of Chemical Physics*, 152(15):154105, Apr. 2020. ISSN 0021-9606, 1089-7690. doi: 10.1063/5.0005082. URL https://pubs.aip.org/jcp/article/152/15/154105/1058748/Quantum-ESPRESSO-toward-the-exascale.

[13] A. J. Giles, S. Dai, I. Vurgaftman, T. Hoffman, S. Liu, L. Lindsay, C. T. Ellis, N. Assefa, I. Chatzakis, T. L. Reinecke, J. G. Tischler, M. M. Fogler, J. H. Edgar, D. N. Basov, and J. D. Caldwell. Ultralow-loss polaritons in isotopically pure boron nitride. *Nature Mater*, 17(2):134–139, Feb. 2018. ISSN 1476-1122, 1476-4660. doi: 10.1038/nmat5047. URL https://www.nature.com/articles/nmat5047.

[14] G. Giuliani and G. Vignale. *Quantum Theory of the Electron Liquid*. Cambridge University Press, 2005.

[15] G. Grosso and G. Pastori Parravicini. *Solid state physics*. Academic Press, an imprint of Elsevier, Amsterdam, 2nd edition edition, 2014. ISBN 9780123850300.

[16] Z. Guo, H. Jiang, and H. Chen. Hyperbolic metamaterials: From dispersion manipulation to applications. *Journal of Applied Physics*, 127(7):071101, Feb. 2020. ISSN 0021-8979, 1089-7550. doi: 10.1063/1.5128679. URL https://pubs.aip.org/jap/article/127/7/071101/565888/Hyperbolic-metamaterials-From-dispersion.

[17] H. Herzig Sheinfux, L. Orsini, M. Jung, I. Torre, M. Ceccanti, S. Marconi, R. Maniyara, D. Barcons Ruiz, A. Hötger, R. Bertini, S. Castilla, N. C. H. Hesp, E. Janzen, A. Holleitner, V. Pruneri, J. H. Edgar, G. Shvets, and F. H. L. Koppens. High-quality nanocavities through multimodal confinement of hyperbolic polaritons in hexagonal boron nitride. *Nature Materials*, 23(4):499–505, Apr. 2024. ISSN 1476-1122, 1476-4660. doi: 10.1038/s41563-023-01785-w. URL `https://www.nature.com/articles/s41563-023-01785-w`.

[18] H. Hübener, E. V. Boström, M. Claassen, S. Latini, and A. Rubio. Quantum materials engineering by structured cavity vacuum fluctuations. *Materials for Quantum Technology*, 4(2):023002, jun 2024. doi: 10.1088/2633-4356/ad4e8b. URL `https://dx.doi.org/10.1088/2633-4356/ad4e8b`.

[19] John D. Joannopoulos, Steven G. Johnson, Joshua N. Winn, and Robert D. Meade. *Photonic Crystals: Molding the Flow of Light*. Princeton University Press, second edition edition, 2011. ISBN 1-4008-2824-4 978-1-4008-2824-1. URL `http://ab-initio.mit.edu/book/photonic-crystals-book.pdf`.

[20] P. B. Johnson and R. W. Christy. Optical constants of the noble metals. *Phys. Rev. B*, 6:4370–4379, Dec 1972. doi: 10.1103/PhysRevB.6.4370. URL `https://link.aps.org/doi/10.1103/PhysRevB.6.4370`.

[21] P. B. Johnson and R. W. Christy. Optical constants of transition metals: Ti, v, cr, mn, fe, co, ni, and pd. *Phys. Rev. B*, 9:5056–5070, Jun 1974. doi: 10.1103/PhysRevB.9.5056. URL `https://link.aps.org/doi/10.1103/PhysRevB.9.5056`.

[22] T. A. F. König, P. A. Ledin, J. Kerszulis, M. A. Mahmoud, M. A. El-Sayed, J. R. Reynolds, and V. V. Tsukruk. Electrically tunable plasmonic behavior of nanocube–polymer nanomaterials induced by a redox-active electrochromic polymer. *ACS Nano*, 8(6):6182–6192, 2014. doi: 10.1021/nn501601e. URL `https://doi.org/10.1021/nn501601e`. PMID: 24870253.

[23] P. Lalanne, W. Yan, A. Gras, C. Sauvan, J.-P. Hugonin, M. Besbes, G. Demésy, M. D. Truong, B. Gralak, F. Zolla, A. Nicolet, F. Binkowski, L. Zschiedrich, S. Burger, J. Zimmerling, R. Remis, P. Urbach, H. T. Liu, and T. Weiss. Quasinormal mode solvers for resonators with dispersive materials. *J. Opt. Soc. Am. A*, 36(4):686, Apr. 2019. ISSN 1084-7529, 1520-8532. doi: 10.1364/JOSAA.36.000686. URL `https://opg.optica.org/abstract.cfm?URI=josaa-36-4-686`.

[24] A. H. Larsen, M. Vanin, J. J. Mortensen, K. S. Thygesen, and K. W. Jacobsen.

Localized atomic basis set in the projector augmented wave method. *Physical Review B—Condensed Matter and Materials Physics*, 80(19):195112, 2009.

[25] A. H. Larsen, J. J. Mortensen, J. Blomqvist, I. E. Castelli, R. Christensen, M. Dułak, J. Friis, M. N. Groves, B. Hammer, C. Hargus, E. D. Hermes, P. C. Jennings, P. B. Jensen, J. Kermode, J. R. Kitchin, E. L. Kolsbjerg, J. Kubal, K. Kaasbjerg, S. Lysgaard, J. B. Maronsson, T. Maxson, T. Olsen, L. Pastewka, A. Peterson, C. Rostgaard, J. Schiøtz, O. Schütt, M. Strange, K. S. Thygesen, T. Vegge, L. Vilhelmsen, M. Walter, Z. Zeng, and K. W. Jacobsen. The atomic simulation environment—a python library for working with atoms. *Journal of Physics: Condensed Matter*, 29(27):273002, 2017. URL `http://stacks.iop.org/0953-8984/29/i=27/a=273002`.

[26] N. Lassaline, R. Brechbühler, S. J. W. Vonk, K. Ridderbeek, M. Spieser, S. Bisig, B. le Feber, F. T. Rabouw, and D. J. Norris. Optical fourier surfaces. *Nature*, 582 (7813):506–510, 2020. doi: 10.1038/s41586-020-2390-x. URL `https://doi.org/10.1038/s41586-020-2390-x`.

[27] N. Lassaline, D. Thureja, T. Chervy, D. Petter, P. A. Murthy, A. W. Knoll, and D. J. Norris. Freeform electronic and photonic landscapes in hexagonal boron nitride. *Nano Letters*, 21(19):8175–8181, 2021. doi: 10.1021/acs.nanolett.1c02625. URL `https://doi.org/10.1021/acs.nanolett.1c02625`. PMID: 34591490.

[28] S. Latini, E. Ronca, U. De Giovannini, H. Hübener, and A. Rubio. Cavity control of excitons in two-dimensional materials. *Nano Letters*, 19(6):3473–3479, 2019. doi: 10.1021/acs.nanolett.9b00183. URL `https://doi.org/10.1021/acs.nanolett.9b00183`. PMID: 31046291.

[29] K. H. Michel and B. Verberck. Phonon dispersions and piezoelectricity in bulk and multilayers of hexagonal boron nitride. *Physical Review B*, 83(11):115328, Mar. 2011. ISSN 1098-0121, 1550-235X. doi: 10.1103/PhysRevB.83.115328. URL `https://link.aps.org/doi/10.1103/PhysRevB.83.115328`.

[30] J. J. Mortensen, A. H. Larsen, M. Kuisma, A. V. Ivanov, A. Taghizadeh, A. Peterson, A. Haldar, A. O. Dohn, C. Schäfer, E. Ö. Jónsson, et al. Gpaw: An open python package for electronic structure calculations. *The Journal of Chemical Physics*, 160 (9), 2024.

[31] P. E. S. Pellegrini, L. De-Moraes, F. J. Poma, S. Vaz, F. H. Cioldin, H. E. Hernández-Figueroa, and S. Moshkalev. Nanofabrication of all-dielectric metasurfaces through

pulsed thermal scanning probe lithography. *Scientific Reports*, 15, 07 2025. doi: 10.1038/s41598-025-07428-1.

[32] A. C. Polycarpou. *Introduction to the Finite Element Method in Electromagnetics*. Synthesis Lectures on Computational Electromagnetics. Springer International Publishing, Cham, 2006. ISBN 9783031005619 9783031016899. doi: 10.1007/978-3-031-01689-9. URL https://link.springer.com/10.1007/978-3-031-01689-9.

[33] M. Rubin. Optical properties of soda lime silica glasses. *Solar Energy Materials*, 12(4):275–288, 1985. ISSN 0165-1633. doi: https://doi.org/10.1016/0165-1633(85)90052-8. URL https://www.sciencedirect.com/science/article/pii/0165163385900528.

[34] P. Shekhar, J. Atkinson, and Z. Jacob. Hyperbolic metamaterials: fundamentals and applications. *Nano Convergence*, 1(1):14, Dec. 2014. ISSN 2196-5404. doi: 10.1186/s40580-014-0014-6. URL https://nanoconvergencejournal.springeropen.com/articles/10.1186/s40580-014-0014-6.

[35] L. Sponza, H. Amara, C. Attaccalite, S. Latil, T. Galvani, F. Paleari, L. Wirtz, and F. Ducastelle. Direct and indirect excitons in boron nitride polymorphs: A story of atomic configuration and electronic correlation. *Physical Review B*, 98(12):125206, Sept. 2018. ISSN 2469-9950, 2469-9969. doi: 10.1103/PhysRevB.98.125206. URL https://link.aps.org/doi/10.1103/PhysRevB.98.125206.

[36] G. Stefanucci and R. v. Leeuwen. *Nonequilibrium many-body theory of quantum systems: a modern introduction*. Cambridge university press, Cambridge, 2013. ISBN 9780521766173.

[37] F. Troisi, H. Hübener, A. Rubio, and S. Latini. Cavity-QED-controlled two-dimensional Moiré Excitons without twisting, Aug. 2025. URL http://arxiv.org/abs/2508.02388. arXiv:2508.02388.

[38] A. Woessner, M. B. Lundeberg, Y. Gao, A. Principi, P. Alonso-González, M. Carrega, K. Watanabe, T. Taniguchi, G. Vignale, M. Polini, J. Hone, R. Hillenbrand, and F. H. L. Koppens. Highly confined low-loss plasmons in graphene–boron nitride heterostructures. *Nature Materials*, 14(4):421–425, Apr. 2015. ISSN 1476-1122, 1476-4660. doi: 10.1038/nmat4169. URL https://www.nature.com/articles/nmat4169.

[39] T. Wu, D. Arrivault, W. Yan, and P. Lalanne. Modal analysis of electromagnetic resonators: User guide for the man program. *Computer Physics Communications*, 284:

108627, 2023. ISSN 0010-4655. doi: https://doi.org/10.1016/j.cpc.2022.108627. URL https://www.sciencedirect.com/science/article/pii/S0010465522003460.

[40] J. Yan, J. J. Mortensen, K. W. Jacobsen, and K. S. Thygesen. Linear density response function in the projector augmented wave method: Applications to solids, surfaces, and interfaces. *Physical Review B—Condensed Matter and Materials Physics*, 83 (24):245122, 2011.

[41] W. Yan, R. Faggiani, and P. Lalanne. Rigorous modal analysis of plasmonic nanoresonators. *Phys. Rev. B*, 97:205422, May 2018. doi: 10.1103/PhysRevB.97.205422. URL https://link.aps.org/doi/10.1103/PhysRevB.97.205422.

[42] W. Yao, D. Xiao, and Q. Niu. Valley-dependent optoelectronics from inversion symmetry breaking. *Physical Review B*, 77(23):235406, June 2008. ISSN 1098-0121, 1550-235X. doi: 10.1103/PhysRevB.77.235406. URL https://link.aps.org/doi/10.1103/PhysRevB.77.235406.

[43] A. V. Zayats, I. I. Smolyaninov, and A. A. Maradudin. Nano-optics of surface plasmon polaritons. *Physics Reports*, 408(3):131–314, 2005. ISSN 0370-1573. doi: https://doi.org/10.1016/j.physrep.2004.11.001. URL https://www.sciencedirect.com/science/article/pii/S0370157304004600.

A | Appendix A

A.1. Dielectric waveguide modes

Assuming a TE polarization, Fresnel reflection law can be written as

$$r_{TE} = \frac{cos\theta_i - n \cdot cos\theta_t}{cos\theta_i + n \cdot cos\theta_t}$$

where $n = n_2/n_1$, θ_i is the incidence angle, and θ_t is the transmission angle, as shown in the picture below.

Furthermore, Snell law implies $n_1 sin\theta_i = n_2 sin\theta_t$, i.e. $sin\theta_i = n \cdot sin\theta_t$.

Since $n \cdot cos\theta_t = n\sqrt{1 - sin^2\theta_t}$, it follows $n \cdot cos\theta_t = \sqrt{n^2 - sin^2\theta_i}$. As a consequence:

$$r_{TE} = \frac{cos\theta_i - \sqrt{n^2 - sin^2\theta_i}}{cos\theta_i + \sqrt{n^2 - sin^2\theta_i}}$$

Because we are assuming total internal reflection, it holds true $sin^2\theta_i > n^2$, hence:

$$r_{TE} = \frac{cos\theta_i - i\sqrt{sin^2\theta_i - n^2}}{cos\theta_i + i\sqrt{sin^2\theta_i - n^2}} = \frac{a - ib}{a + ib}$$

By defining $a + ib = ce^{i\varphi}$, it follows $c = \sqrt{a^2 + b^2}$ and $\varphi = arctan(a/b)$. Thus:

$$r_{TE} = \frac{ce^{-i\varphi}}{ce^{+i\varphi}} = e^{-2i\varphi}$$

and therefore:

$$\varphi = arctan\left(\frac{\sqrt{sin^2\theta_i - n^2}}{cos\theta_i}\right)$$

$$\varphi_r = 2\varphi = 2arctan\left(\frac{\sqrt{sin^2\theta_i - n^2}}{cos\theta_i}\right)$$

and

$$tan\left(\frac{\varphi_r}{2}\right) = \frac{\sqrt{sin^2\theta_i - n^2}}{cos\theta_i}$$

From the last picture, it is clear that:

$$\begin{cases} sin\theta_i &= cos\theta \\ cos\theta_i &= sin\theta \end{cases}$$

As a consequence:

$$tan\left(\frac{\varphi_r}{2}\right) = \frac{\sqrt{cos^2\theta - n^2}}{sin\theta} = \sqrt{\frac{1 - sin^2\theta - sin^2\theta_{1CR}}{sin^2\theta}} = \sqrt{\frac{1 - sin^2\theta_{1CR}}{sin^2\theta} - 1} = \\ = \sqrt{\frac{cos^2\theta_{1CR}}{sin^2\theta} - 1}$$

Having two expressions involving φ_r, it is now possible to equate them and find:

$$tan\left(\frac{\pi}{\lambda} n_1 d \cdot sin\theta - q\frac{\pi}{2}\right) = \sqrt{\frac{cos^2\theta_{1CR}}{sin^2\theta} - 1}$$

Solutions of this equations are $sin\theta$ where θ corresponds to a propagating mode of the waveguide. However this equation can only be solved numerically, and not analytically. Nonetheless, with the help of a few algebraic manipulation, it is possible to get some insight. First consider $sin\theta = y$ and plot the following:

$$\begin{cases} f(y) = tan\left(\frac{\pi}{\lambda} n_1 d \cdot sin\theta - q\frac{\pi}{2}\right) \\ g(y) = \sqrt{\frac{cos^2\theta_{1CR}}{sin^2\theta} - 1} \end{cases}$$

The solutions are the points where $f(y)$ meets $g(y)$. Note that $g(y)$ exist only up to $y = sin\theta_{CR}$. Therefore the number of guided mode is set to a value M given by:

$$M = \left\lceil 2n_1 d \cdot \frac{sin\theta_{CR}}{\lambda} \right\rceil$$

Writing $sin\theta_{CR}$ as a function of n_1 and n_2:

$$\frac{2n_1 d}{\lambda} sin\theta_{CR} = \frac{2n_1 d}{\lambda}\sqrt{1 - cos^2\theta_{CR}} = \frac{2n_1 d}{\lambda}\sqrt{1 - sin^2\theta_{1CR}} = \frac{2n_1 d}{\lambda}\sqrt{1 - \frac{n_2^2}{n_1^2}} = \\ = \frac{2d}{\lambda}\sqrt{n_1^2 - n_2^2}$$

Hence, it is possible to have a more physically meaningful expression for M:

$$M = \left\lceil \frac{2d}{\lambda}\sqrt{n_1^2 - n_2^2} \right\rceil$$

where the term $\sqrt{n_1^2 - n_2^2}$ is known as *numerical aperture*.

A.2. Dielectric waveguide e.m. field

Having understood the conditions required for modes to propagate, it is now time to analyse their behaviour more closely. In the following, assume a mode travels with an angle θ_m and has a TE polarization. Thus, in a similar fashion to the Fabry-Perot case, it is possible to write:

$$\vec{k}^+ = \frac{2\pi}{\lambda} n_1 sin\theta_m \vec{u}_z + \frac{2\pi}{\lambda} n_1 cos\theta_m \vec{u}_x = k_{zm}\vec{u}_z + k_{xm}\vec{u}_x$$
$$\vec{k}^- = -\frac{2\pi}{\lambda} n_1 sin\theta_m \vec{u}_z + \frac{2\pi}{\lambda} n_1 cos\theta_m \vec{u}_x = -k_{zm}\vec{u}_z + k_{xm}\vec{u}_x$$

Hence:

$$E(x, z, t) = u_m e^{i(\omega t - k_{xm} x}$$

where:

$$u_m = \begin{cases} A_m cos\left(\frac{2\pi n_1 sin\theta_m}{\lambda} y\right) & n \text{ even} \\ A_m sin\left(\frac{2\pi n_1 sin\theta_m}{\lambda} y\right) & n \text{ odd} \end{cases}$$

In the previous example, it was possible to impose the condition of null field at the mirror position and beyond, because it was assumed that their surface was perfectly reflecting. However, it is not possible to apply the same strategy here, as the modes will have a tail in the cladding region. It is therefore necessary to calculate their behaviour in the cladding. Consider the Helmoltz equation:

$$\nabla^2 \vec{\tilde{E}} + \frac{\omega^2 n^2}{c^2} \vec{\tilde{E}} = \vec{0}$$

Because of the TE polarization assumption $\tilde{E} = \tilde{E}_y(x, z)$, thus $\partial^2 \tilde{E}_y / \partial y^2 = 0$, and the equation becomes:

$$\frac{\partial^2 \tilde{E}_y}{\partial z^2} + \frac{\partial^2 \tilde{E}_y}{\partial x^2} + \frac{\omega^2 n_2^2}{c^2} \tilde{E}_y = 0$$

By considering $\tilde{E}_y$ as a superposition of modes, it is immediate to deduce:

$$\frac{\partial \tilde{E}_y}{\partial z} = c_m \frac{du_m}{dz} e^{ik_{xm}x} \rightarrow \frac{\partial^2 \tilde{E}_y}{\partial z^2} = c_m \frac{d^2 u_m}{dz^2} e^{ik_{xm}x}$$
$$\frac{\partial \tilde{E}_y}{\partial x} = c_m u_m(z)(-ik_{xm}) e^{ik_{xm}x} \rightarrow \frac{\partial^2 \tilde{E}_y}{\partial x^2} = -c_m u_m(z) k_{xm}^2 e^{ik_{xm}x}$$

Inserting these expressions into the equation, it follows:

$$\frac{d^2u_m}{dz^2} - \gamma_m^2 u_m = 0 \quad \text{where} \quad \gamma_m^2 = k_{xm}^2 - \frac{\omega^2}{c^2} n_2^2$$

Making the ansatz $u_m(z) = e^{gz}$, it follows:

$$g^2 e^{gz} - \gamma_m^2 e^{gz} = 0$$

Assuming $g = \pm\gamma_m$, the solution is $u_m(z) = e^{\pm\gamma_m z}$. Therefore:

$$u_m(z) = c_m e^{-\gamma_m z} \quad \text{for } z > d/2$$
$$u_m(z) = c_m e^{+\gamma_m z} \quad \text{for } z < d/2$$

B | Appendix B

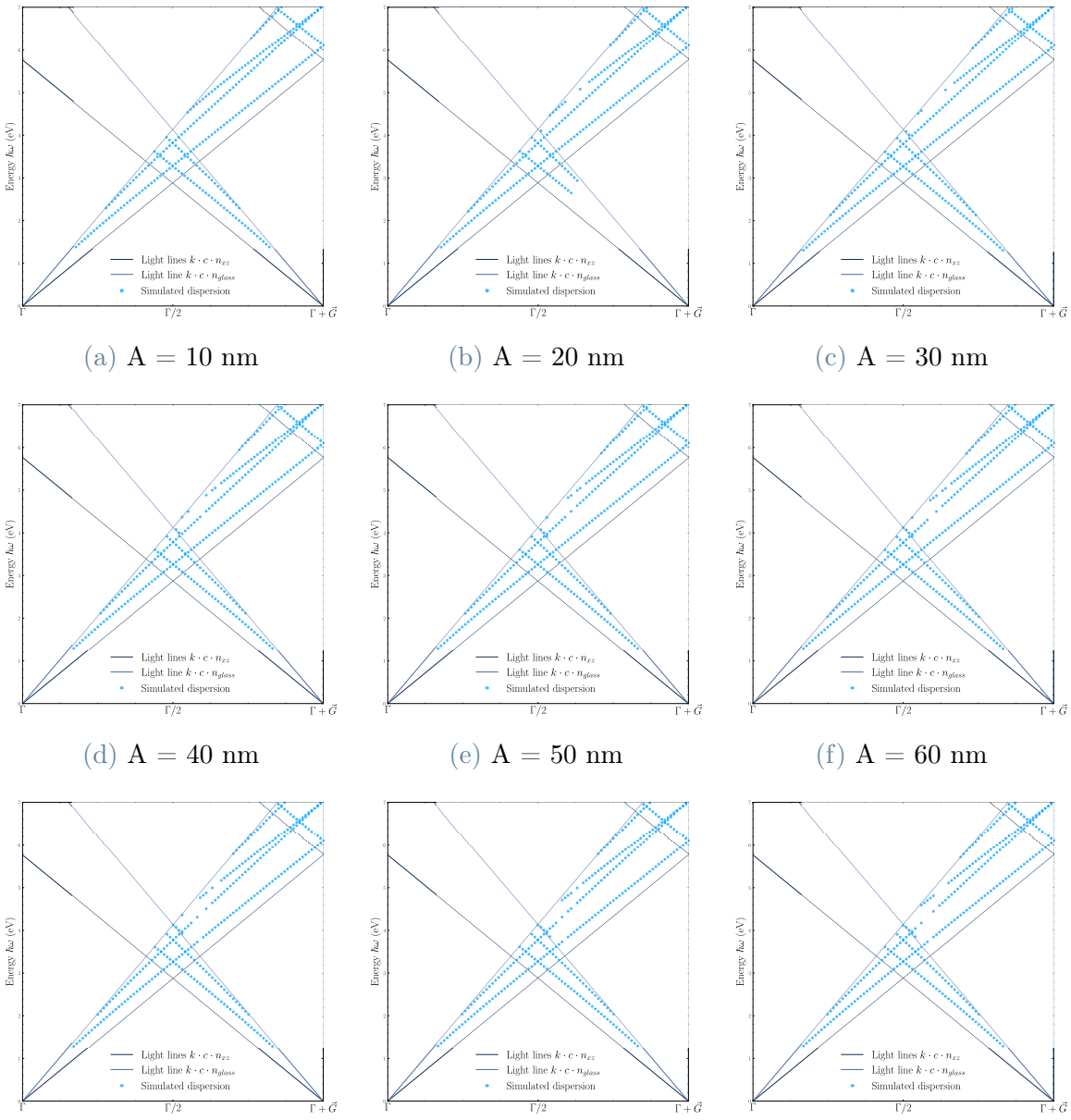

(a) A = 10 nm (b) A = 20 nm (c) A = 30 nm

(d) A = 40 nm (e) A = 50 nm (f) A = 60 nm

(g) A = 70 nm (h) A = 80 nm (i) A = 90 nm

Figure B.1: Simulations with a period of 100 nm, A = amplitude of the sinusoidal pattern

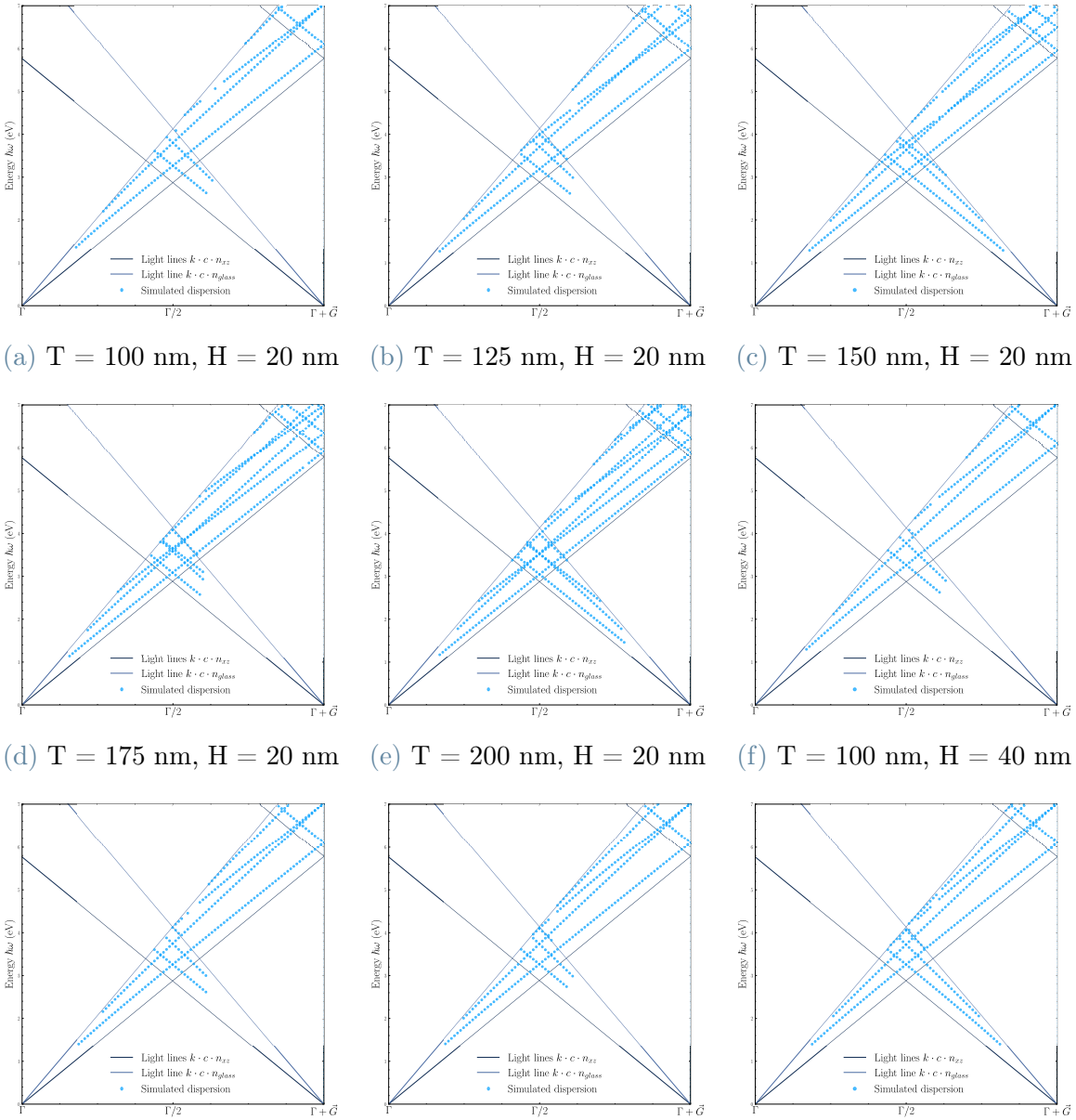

(a) T = 100 nm, H = 20 nm (b) T = 125 nm, H = 20 nm (c) T = 150 nm, H = 20 nm

(d) T = 175 nm, H = 20 nm (e) T = 200 nm, H = 20 nm (f) T = 100 nm, H = 40 nm

(g) T = 100 nm, H = 80 nm (h) T = 100 nm, H = 120 nm (i) T = 100 nm, H = 160 nm

Figure B.2: Simulations with a period of 100 nm, T = core layer thickness, H = resist thickness, i.e. minimum core-resist distance

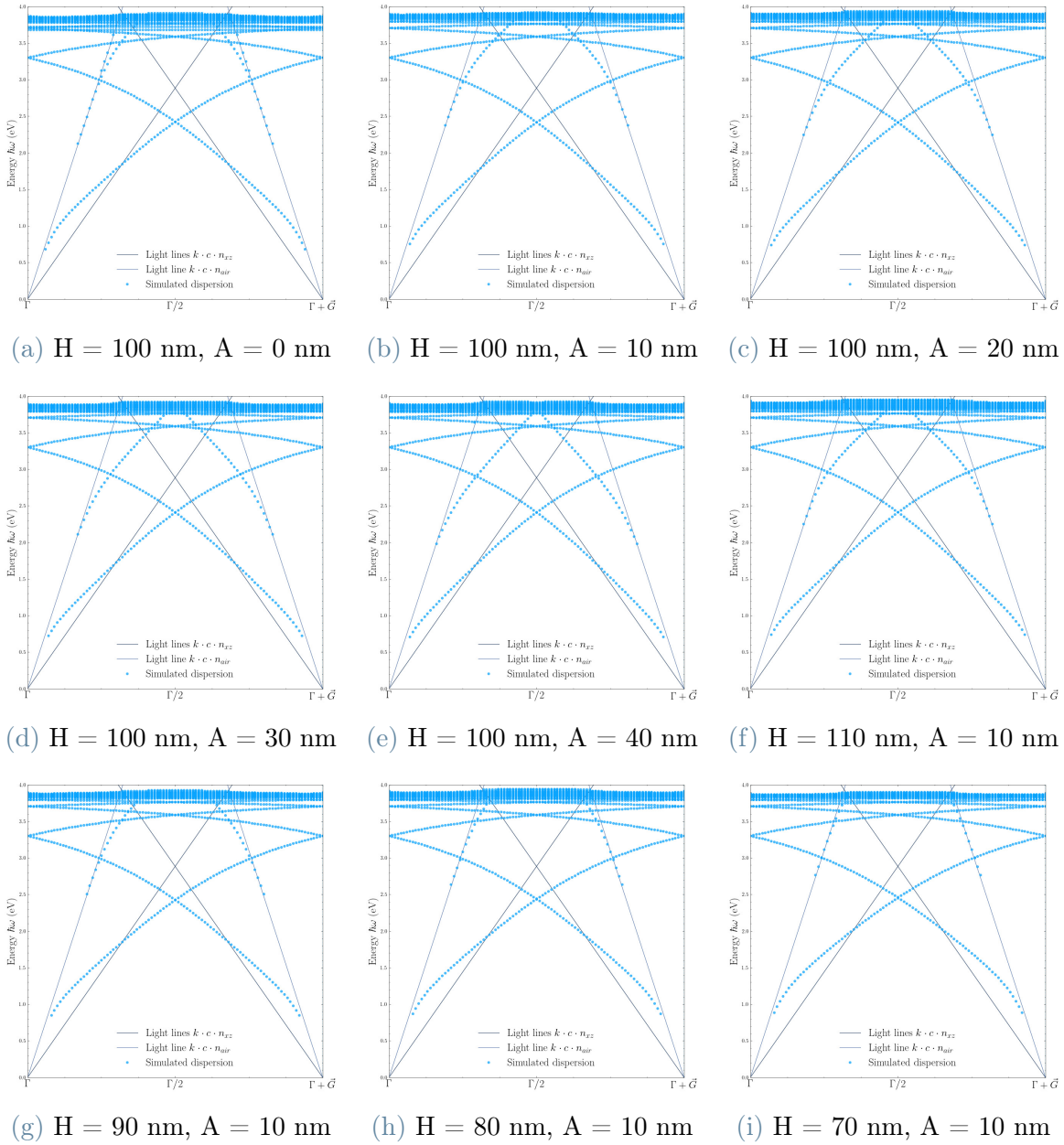

(a) H = 100 nm, A = 0 nm (b) H = 100 nm, A = 10 nm (c) H = 100 nm, A = 20 nm

(d) H = 100 nm, A = 30 nm (e) H = 100 nm, A = 40 nm (f) H = 110 nm, A = 10 nm

(g) H = 90 nm, A = 10 nm (h) H = 80 nm, A = 10 nm (i) H = 70 nm, A = 10 nm

Figure B.3: Simulations with a period of 100 nm, H = core layer height, A = amplitude of the pattern

List of Figures

Acknowledgements

I wish to thank my supervisors at DTU prof. Simone Latini, prof. Søren Raza, prof. Bjarken Sørensen Jessen, my supervisor at Politecnico di Milano prof. Giulio Nicola Felice Cerullo, and the 2DPHYS section of the Physics Departement at DTU, with a special mention for PostDoc Cheng Xiang, PostDoc Xavier Zambrana Puyalto, and Master Student Magnus Vejby Nielsen. I also wish to express my gratitude towards PostDoc Burak Gurlek at Max Planck Institute for the Structure and Dynamics of Matter.